Measurement of the Λ_b^0 lifetime in the exclusive decay $\Lambda_b^0 \to J/\psi\Lambda^0$ with the DØ detector

Ivan Heredia de la Cruz

Centro de Investigación y de Estudios Avanzados del IPN

Department of Physics

A thesis submitted for the degree of

Doctor of Science
Speciality in Physics

Supervisor: Heriberto Castilla Valdez

Mexico City June 2012

Resumen

En este trabajo reportamos la medición del tiempo de vida del barión Λ_b^0 utilizando el decaimiento exclusivo $\Lambda_b^0 \to J/\psi\,\Lambda^0$. El tiempo de vida del mesón B^0 se mide a su vez en el canal topológicamente similar $B^0 \to J/\psi\,K_S^0$, el cual verifica nuestro procedimiento de medición, y permite una determinación directa del cociente del tiempo de vida del Λ_b^0 y el B^0. Los datos utilizados en este análisis fueron grabados por el detector DØ durante la segunda corrida del colisionador Tevatron en el Fermilab, del 2002 al 2011, y corresponde a una luminosidad integrada de 10.4 fb^{-1} de colisiones protón-antiprotón a una energía de centro de masa de $\sqrt{s} = 1.96$ TeV. De aquí obtenemos $\tau(\Lambda_b^0) = 1.303 \pm 0.075$ (stat.) ± 0.035 (syst.) ps, $\tau(B^0) = 1.508 \pm 0.025$ (stat.) $\pm$ 0.043 (syst.) ps y $\tau(\Lambda_b^0)/\tau(B^0) = 0.864 \pm 0.052$ (stat.) $\pm$ 0.033 (syst.). Estas mediciones mejoran y reemplazan los resultados previos de la Colaboración DØ que emplean los mismos canales de decaimiento. Nuestra medición del cociente de tiempos de vida concuerda de forma excelente con las predicciones teóricas y es compatible con el promedio mundial actual, aunque difiere de la medición más reciente de la Colaboración CDF en más de 2 desviaciones estándares.

Abstract

In this work we report a measurement of the Λ_b^0 baryon lifetime using the exclusive decay $\Lambda_b^0 \to J/\psi\,\Lambda^0$. The B^0 meson lifetime is also measured in the topologically similar channel $B^0 \to J/\psi\,K_S^0$, which provides a cross-check of the measurement procedure, and allows a direct determination of the ratio of the Λ_b^0 and the B^0 lifetimes. The data used in this analysis were collected with the DØ detector during the complete Run II of the Fermilab Tevatron Collider, from 2002 to 2011, and correspond to an integrated luminosity of 10.4 fb^{-1} of proton-antiproton collisions at a center of mass energy $\sqrt{s} = 1.96$ TeV. We obtain $\tau(\Lambda_b^0) = 1.303 \pm 0.075$ (stat.) $\pm\, 0.035$ (syst.) ps, $\tau(B^0) = 1.508 \pm 0.025$ (stat.) $\pm\, 0.043$ (syst.) ps and $\tau(\Lambda_b^0)/\tau(B^0) = 0.864 \pm 0.052$ (stat.)± 0.033 (syst.). These measurements supersede previous results of the DØ Collaboration using the same decay channels. Our measurement of the lifetime ratio is in excellent agreement with theoretical predictions and compatible with the current world-average, but differs with the latest measurement of the CDF Collaboration in more than 2 standard deviations.

A mis padres y mis hermanos.

Y con mucho amor ...
a Lily.

Acknowledgements

It happened one day, as any other, that Dr. Heriberto Castilla Valdez invited me to do my PhD with him. I accepted. It was hard, but I do not regret. There were many valuable experiences and challenges that, for better or worse, I owe to Heriberto.

Four years and a half ago, my wife and I packed four bags, threw away all other stuff, and traveled to Chicago. We were received by Dr. Jesus Orduña, who shortly after became a good friend of us. We will always be grateful to him for all his help.

I sincerely thank the DØ experiment spokespersons, Dmitri Denisov, Darien Wood, Stefan Söldner-Rembold and Gregorio Bernardi, for their support during my long visit to the DØ experiment, and for trusting and accepting me as member of the DØ Collaboration. I am grateful to the DØ run coordinators, detector and algorithm experts, who taught me about the experiment and were always there backing me up: George Ginther, William Lee, Marc Buehler, Stefan Grünendahl, Jadzia Warchol, Rick Jesik, Rolando Flores and Herb Greenlee. I am specially grateful to Stefan G. for his patience and willingness to train me as a L1 CTT expert.

To the DØ physics coordinators, Aurelio Juste, Marco Verzocchi and Christian Schwanenberger, and the b physics group conveners, Penny Kasper, Mark Williams and Marjorie Corcoran, for their helpful comments and guidance. To the members of the Editorial Boards that evaluated my work, Brendan Casey, Avdhesh Chandra, Hal Evans, Dmitry Tsybychev, Gene Fisk and Arthur Maciel; as well as my senior colleagues, Eduard de la Cruz Burelo and Alberto Sánchez Hernández, that kindly shared their experience and knowledge with me.

To the evaluation committee integrated by Dr. Pedro Luis Manuel Podesta Lerma, from Universidad Autónoma de Sinaloa, and Drs. Miguel Ángel Pérez Angón, Agustin Conde Gallardo and Alberto Sánchez Hernández, from Cinvestav, who contributed to improve the quality of this thesis. Also to the academic coordinators of the Cinvestav physics department, Drs. Abdel Pérez Lorenzana and Luis Fernando Rojas Ochoa, who always backed me up on my period as a graduate student.

I want to express my most sincere gratitude and appreciation to the women who made my life easier and pleasant at Fermilab, Sonya Wright, Julie Saviano, Jackie Cyko and Cheryl Bentham, as well as the efficient and nice team of academic support at Cinvestav formed by Flora Ibáñez, Patricia Villar, Elizabeth Mote and Rosemary Ovando.

To my closest friends: Estela Garcés, Jorge Martínez, Enrique Camacho, Roger Hernández, Jesus Orduña, Minerba Betancourt, Liliana Toscano, Alonso Contreras, Michelle Prewitt, and Alejandro García. It's been a pleasure to share so many good moments with you. Ricardo, it was good while it lasted. And to my little friend Bolt, who stood with me in those busy days.

Also to the friends who gave us the opportunity to stay at their place during hard times: Marta and Paola Orduña, and Mireya and Luis Lenin.

To CONACyT, that once again funded my education.

To the Fermi Research Alliance, LLC, and the Universities Research Association, Inc., that made possible my visit to Fermilab.

Last but never least. To my family: mom, dad, brothers, I love you and have missed you so much while I've been away. You are the source of my strength and determination. And from the depths of my heart, I love you Lily, thank you for always being there for me, you give all meaning to my life.

Contents

List of Figures

List of Tables

Acronyms

Aϕ counter Scintillation counter on the A-layer PDTs

A-layer Muon detectors located inside the central toroid

AA Alternative Algorithm

B-layer Muon detectors located outside the central toroid

C-layer Muon detectors located outside the B layer

CERN Conseil Européen pour la Recherche Nucléaire (European Organization for Nuclear Research)

CFT Central fiber tracker

CKM Cabibbo-Kobayashi-Maskawa

CTT Central track trigger

DCA Distance of closest approach

DS Double-sided silicon sensor

DSDM Double-sided double-metal silicon sensor

EW Electroweak

F-disk Smaller of two sizes of SMT disks

Fermilab Fermi National Accelerator Laboratory

FODO Focusing-defocusing magnets

H-disk Larger of two sizes of SMT disks, located at high η

HQE Heavy quark expansion

HQET Heavy quark effective theory

HQS Heavy quark symmetry

IP Impact parameter

L0 SMT Layer-0 (innermost SMT layer)

L1 Level 1 trigger

L2 Level 2 trigger

L3 Level 3 trigger

LHC Large Hadron Collider

LQCD Lattice QCD

MC Monte-Carlo (simulation)

MDT Mini drift tube

OPE Operator product expansion

PDF Probability density function

PDL Proper decay length

PDT Proportional drift tube

PQCD Perturbative QCD

PV Primary interaction vertex

QCD Quantum chromodynamics

QCDSR QCD sum rules

RF Radio-frequency

SM Standard Model

SMT Silicon microstrip tracker

SS Single-sided silicon sensor

Chapter 1

Introduction

Until recently, the only particle collider capable of producing weakly-decaying b baryons was the Fermilab Tevatron Collider. The fractions of the different hadron species are believed to be the same in unbiased samples of high momentum b jets originating from Z decays and $p\overline{p}$ collisions at the Tevatron (although early Tevatron results discouraged this assumption). The world average production fraction of b baryons is $f(b \to \text{baryon}) = 0.083 \pm 0.020$ [1] and is a mixture of Λ_b^0, Ξ_b^-, Ξ_b^0, Ω_b^-, etc.

Even for the lightest and most copiously produced b baryon, the $\Lambda_b(udb)$, only a few decay channels and properties have been studied. With the full datasets of the DØ and CDF experiments at Fermilab and the excellent performance of the Large Hadron Collider (LHC) and the experiments at CERN, it is now possible to study more precisely important effects on b baryons, such as lifetimes, polarization, CP and T violation. In particular, the uncertainties on Λ_b^0 branching fractions are on the order of $\sim$(30–60)% [1]. We recently measured the production fraction $f(b \to \Lambda_b^0)$ multiplied by the branching fraction of the decay $\Lambda_b^0 \to J/\psi\,\Lambda^0$ [2, 3]. This measurement is useful to study $b \to s$ decays such as $\Lambda_b^0 \to \mu^+\mu^-\Lambda^0$ which are forbidden at tree level in the Standard Model [4].

The Λ_b^0 ought to have spin 1/2 and positive intrinsic parity, $J^P = 1/2^+$, however neither of these quantum numbers have actually been measured. The mass of the Λ_b^0 baryon is measured to be $m(\Lambda_b^0) = (5620.2 \pm 1.6)$ MeV/c^2 and the current world average lifetime is $\tau(\Lambda_b^0) = (1.425 \pm 0.032)$ ps [1].

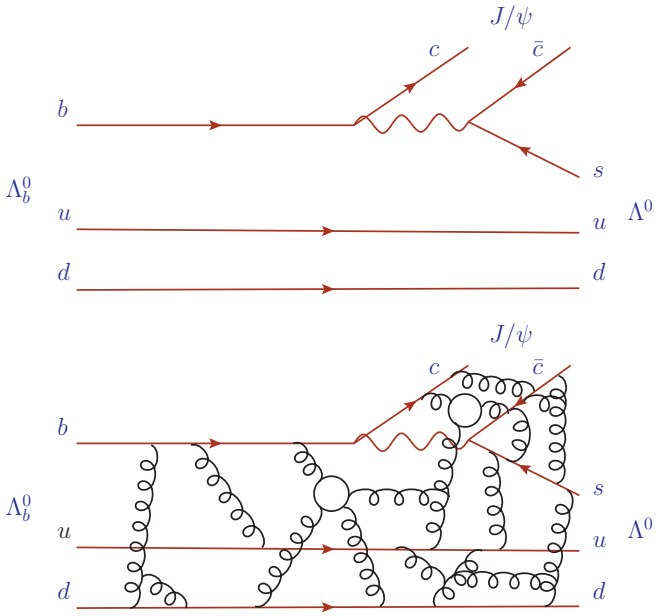

Figure 1.1: Top: Feynman diagram of the weak decay $\Lambda_b^0 \to J/\psi\,\Lambda^0$. Bottom: more realistic representation of the decay $\Lambda_b^0 \to J/\psi\,\Lambda^0$.

Lifetime measurements of particles containing b quarks provide important tests of the significance of strong interactions between the constituent partons in the weak decay of b hadrons. We take as example the decay $\Lambda_b^0 \to J/\psi\,\Lambda^0$, shown in Fig. 1.1, where the simple description of the weak decay is complicated by the action of the strong interactions. These interactions produce measurable differences between b hadron lifetimes that the heavy quark expansion (HQE) [5] predicts with good accuracy through the calculation of lifetime ratios. While the agreement of the ratios between experimental measurements and HQE is excellent for B mesons [6], there are remaining discrepancies between experimental results and theoretical predictions for b baryons.

Recently, the CDF Collaboration [7] used the exclusive decay $\Lambda_b^0 \to J/\psi\,\Lambda^0$ to report the single most precise determination of the Λ_b^0 lifetime which is more than 2 standard deviations higher than the world average [1] and slightly above the B^0 lifetime. The CDF measurement of the lifetime ratio, $\tau(\Lambda_b^0)/\tau(B^0)$, is higher than the HQE calculation including $\mathcal{O}(1/m_b^4)$ effects, 0.88 ± 0.05 [8, 9]. On the other hand, theoretical predictions are in agreement with measurements by the DØ Collaboration in

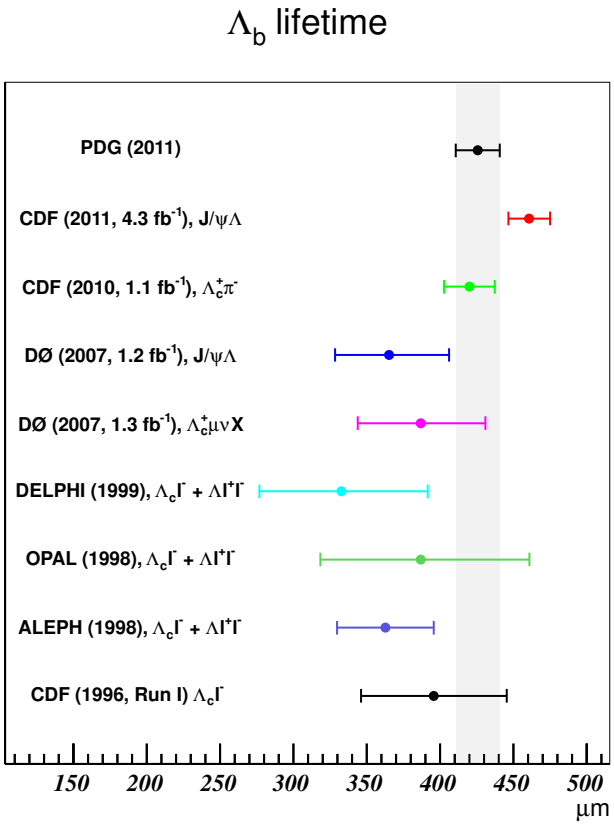

Figure 1.2: Measurements of the Λ_b^0 lifetime.

the $J/\psi\Lambda^0$ [10] and semileptonic [11] channels, by the CDF Collaboration in the $\Lambda_c^+\pi^-$ final state [12], by the DELPHI, OPAL and ALEPH Collaborations in semileptonic decays [13, 14, 15], and previous measurements also in semileptonic channels by the CDF Collaboration [16]. The experimental status is summarized in Fig. 1.2. More measurements of the Λ_b^0 lifetime and of the ratio $\tau(\Lambda_b^0)/\tau(B^0)$ are required to resolve this discrepancy.

This work is our contribution to the pool of existing measurements. At the time of writing this thesis, only two physics analyses use the complete DØ dataset, and this is one of them. Also, for over 10 years only two experiments have been able to measure the Λ_b^0 lifetime and we are proud to belong to one of them.[1]

[1]The LHCb experiment reported a preliminary result of the Λ_b^0 lifetime in a public conference note

1. INTRODUCTION

[LHCb-CONF-2011-001, March 24, 2011], $\tau(\Lambda_b^0) = 405.6 \pm 32.37$ (stat.) $\pm$ 10.5 (syst.) μm. To date, LHCb result has not been submitted to a refereed journal nor updated.

Chapter 2

Theoretical and experimental techniques

In the following sections we develop the theoretical framework to predict b hadron lifetimes. We start with a short introduction of the Standard Model of elementary particles. We define a general strategy to calculate exclusive decay rates and study some of the approximate symmetries of the heavy quarks in the context of the heavy quark effective theory. Then, these tools are used to exemplify the heavy quark expansion of the Λ_b^0 decay width and to show the best predictions of the lifetime ratio $\tau(\Lambda_b^0)/\tau(B^0)$. Finally, we provide a general overview of the methods used to measure the Λ_b^0 lifetime.

2.1 Standard Model and the CKM matrix

The Standard Model (SM) of elementary particles is the unification of the electroweak (EW) interactions, described by the symmetry group $SU(2)\times U(1)$, and Quantum Chromodynamics (QCD) described by the gauge symmetry $SU(3)$. The gauge structure of these SM interactions has been verified comprehensively by many different experiments during the last three decades. The building blocks and interactions of the SM are summarized in Fig. 2.1. Leptons and quarks, which are spin 1/2 fermions arranged in three generations of similar physical properties, form all the known visible

matter.[1] On the other hand, gluons, $W^{\pm}$, Z^0, photon and Higgs are (gauge) bosons that mediate the strong, weak and electromagnetic interactions.

Quarks carry color charge, and the gluons mediate the strong interactions between color charged particles. A consequence of the QCD theory is that quarks are strongly bound or "confined" in color-neutral composite particles (hadrons) containing quark-antiquark pairs (mesons) or three quarks (baryons).

In the SM the mass of the quarks, flavor violation and CP violation arise from Yukawa interactions with the Higgs field. The Yukawa couplings are simply chosen to contrive the observed masses. On the other hand, the strength of flavor-changing weak decays are parametrized by the entries of the Cabibbo-Kobayashi-Maskawa (CKM) matrix (V_{CKM}) in the charged-current J^{μ}_{CC} to W boson field:

$$L_{CC} = -\frac{g}{\sqrt{2}} J^{\mu}_{CC} W^{\dagger}_{\mu} + \text{h.c.}, \tag{2.1}$$

where

$$J^{\mu}_{CC} = \left(\bar{\nu}_e, \bar{\nu}_\mu, \bar{\nu}_\tau\right) \gamma^{\mu} \begin{pmatrix} e_L \\ \mu_L \\ \tau_L \end{pmatrix} + \left(\bar{u}_L, \bar{c}_L, \bar{t}_L\right) \gamma^{\mu} V_{CKM} \begin{pmatrix} d_L \\ s_L \\ b_L \end{pmatrix}. \tag{2.2}$$

Only left-handed fermion fields participate in the weak interaction. At low energies, this interaction can be seen as local four-fermion couplings of the form

$$\mathcal{L}_{\text{eff}} = -2\sqrt{2} G_F J^{\mu}_{CC} J^{\dagger}_{CC,\mu}, \tag{2.3}$$

where $G_F = 1.16637(1) \times 10^{-5}$ GeV^{-2} is the Fermi constant.

By construction, the CKM matrix is unitary and leads to CP violation if like-charged quarks all have distinct masses. The same construction also leads to the Glashow-Iliopoulus-Maiani effect: there are no flavor-changing neutral currents at the tree level in the SM. These properties are presented in a schematic form in Fig. 2.2, where interactions between members of the same generation are strong, and the interactions between generations are weaker and possible only (at tree level) through charged currents ($W^{\pm}$ decays, between up and down type quarks). The CKM matrix for the known three

[1] We use the term "visible" matter to distinguish between ordinary matter (known quarks and leptons) and other exotic forms such as dark matter or dark energy.

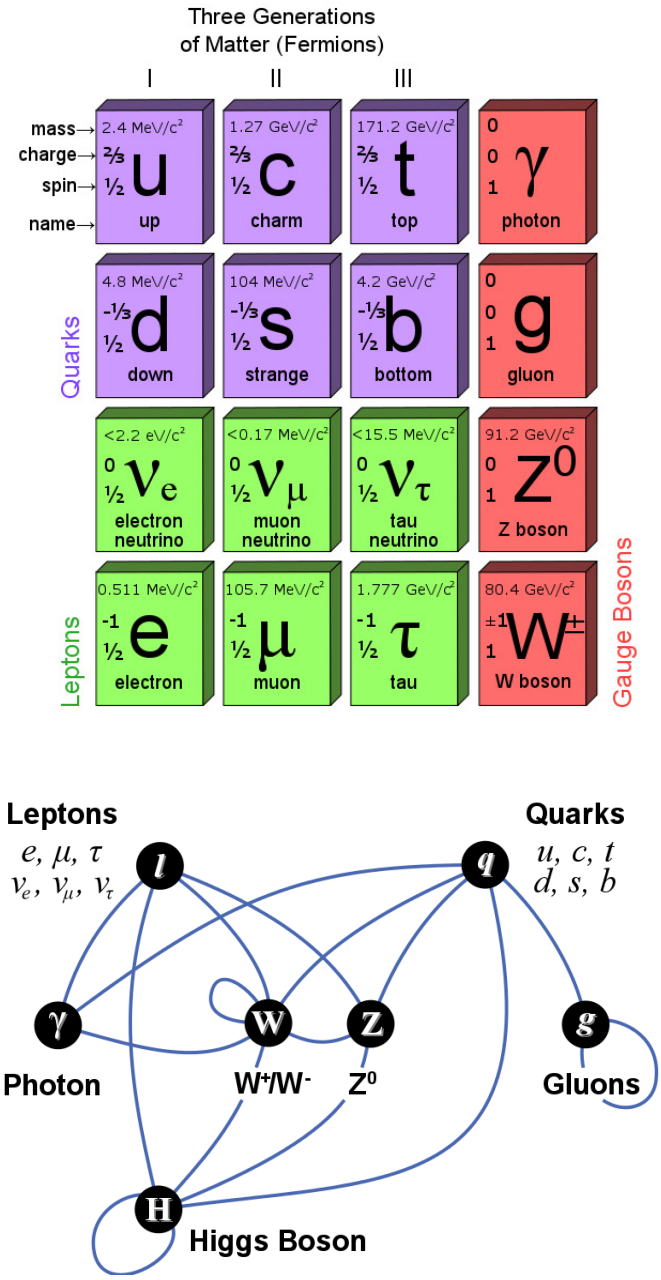

Figure 2.1: The Standard Model of elementary particles and interactions [17].

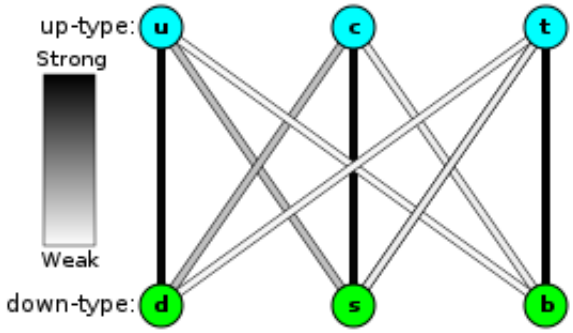

Figure 2.2: Pictorial representation of the strength of flavor-changing weak decays [18].

generations, usually written

$$V_{CKM} = \begin{pmatrix} V_{ud} & V_{us} & V_{ub} \\ V_{cd} & V_{cs} & V_{cb} \\ V_{td} & V_{ts} & V_{tb} \end{pmatrix}, \tag{2.4}$$

has only three real (CP conserving) and one imaginary (CP violating) parameters. The unitarity of the CKM matrix relates the elements of the matrix. The orthogonality of columns leads to interesting constraints, for instance,

$$V_{us}V_{ub}^{*} + V_{cs}V_{cb}^{*} + V_{ts}V_{tb}^{*} = 0, \tag{2.5}$$

defining a triangle in the complex plane, where the lengths of the sides are $|V_{us}V_{ub}^{*}|$, $|V_{cs}V_{cb}^{*}|$, and $|V_{ts}V_{tb}^{*}|$, and their respective opposing angles are $\beta_s = \arg\left[-\frac{V_{cs}V_{cb}^{*}}{V_{ts}V_{tb}^{*}}\right]$, $\alpha_s = \arg\left[-\frac{V_{ts}V_{tb}^{*}}{V_{us}V_{ub}^{*}}\right]$ and $\gamma_s = \arg\left[-\frac{V_{us}V_{ub}^{*}}{V_{cs}V_{cb}^{*}}\right]$. A measurement of β_s is important since is expected to be on the order of one degree, and any large deviation from zero would be a clear sign of new physics. Recently, the Cinvestav group on the DØ experiment has worked on a measurement of this angle through the study of the temporal-angular distribution of $B_s^0 \to J/\psi\phi$ decays [19]. The bottom line is that separate and even redundant measurements of lengths (through decay and mixing rates) and angles (through CP asymmetries) are needed to test the validity of the CKM mechanism. The feasibility of these studies is, however, hindered by quark confinement in hadrons and, hence, hadronic matrix elements must be evaluated to compare model parameters (v.g. CKM matrix) to experimental measurements.

To deal with hadronic matrix elements (strong interactions), depending on the case, theoreticians have developed several approaches and tools such as perfect symmetries (C or CP conservation), approximate symmetries (isospin, flavor SU(3), chiral or heavy quark symmetries), lattice QCD (LQCD), perturbative QCD (PQCD) for exclusive processes, QCD sum rules (QCDSR), and many other models of QCD (quark models, factorization, etc.).

2.2 Decay rates and effective Hamiltonians

The decay rate or *decay width*[1] of a b hadron H_b with momentum $\mathbf{P}$ into some final state f of n particles is calculated using the Fermi's Golden Rule:

$$\Gamma(H_b \to f) = S_f \frac{(2\pi)^4}{2E(\mathbf{P})} \int \delta^4 \left(P - \sum\nolimits_i k_i \right) |\mathscr{M}_f(P; k_i)|^2 \prod_{j=1}^{n} \frac{\mathrm{d}^3 k_j}{(2\pi)^3 2E_j(\mathbf{k}_j)}, \qquad (2.6)$$

where $E_i(\mathbf{k}_i)^2 = k_i^2 + m_i^2$, m_i is the mass of particle i, $\mathscr{M}_f(P; k_i)$ is the invariant amplitude of the decay, and S_f is a combinatorial factor to account for identical configurations in the final state f.

The confinement of quarks and gluons occur on a length scale $R_{had} \sim 1/\Lambda_{QCD} \sim 1$ fm, which determines the size of hadrons. The parameter Λ_{QCD} ($\approx 200 - 400$ MeV) is a fundamental quantity in QCD that sets the scale for the running coupling constant. For energies lower than Λ_{QCD}, the strong coupling constant is large and a perturbative development of the physical quantities is impossible. On the other hand, when two quarks are very close ($\ll 1/\Lambda_{QCD}$), the coupling constant is small (asymptotic freedom), and a perturbative approach is feasible. The asymptotic freedom allows us to write the decay amplitude as an *operator product expansion* (OPE),

$$\mathscr{M}_f = -\frac{4G_F}{\sqrt{2}} \sum_j V_{CKM}^j C_j(\mu) \langle f | O_j(\mu) | B \rangle \left[1 + \mathcal{O}\left(\frac{m_b^2}{M_W^2} \right) \right], \qquad (2.7)$$

where μ is a renormalization scale, m_b the mass of the b quark, m_W the mass of the W boson, and V_{CKM}^j are products of the corresponding CKM elements (for example, $V_{cb}V_{cs}^*$ in $\Lambda_b^0 \to J/\psi\, \Lambda^0$ decays). Physics from distances shorter than μ^{-1} is encompassed in

[1] The decay rate or width is the probability per unit time that the particle will decay.

the Wilson coefficients C_j (dependence on the top mass, M_W, etc.), that are universal since do not depend on the final state f. On the other hand, the hadronic matrix elements $\langle f|O_j(\mu)|B\rangle$ account for phenomena occurring at distances longer than μ^{-1} (e.g. dependence on Λ_{QCD}), and are usually evaluated using non-perturbative methods such as LQCD or QCDSR. Therefore, at a scale of order m_b and up to corrections of order m_b^2/M_W^2, we can write an effective Hamiltonian, where C_j's can be viewed as effective coupling constants and O_j's as the corresponding vertices:

$$H_{eff} = \frac{4G_F}{\sqrt{2}} \sum_j V_{CKM}^j C_j O_j + \text{h.c.} \tag{2.8}$$

C_j constants can be calculated perturbatively to include hard QCD effects. A list of O_j operators in the SM and extensions of the SM as well as numerical values of C_j, including their renormalization group evolution, can be found in Refs. [20, 21, 22] (and references therein).

2.3 Heavy quark symmetry

Once the short-distance physics has been separated from the long-distance physics, the latter can be simplified taking advantage of approximate symmetries, which imply non-trivial relations between observables. A *heavy quark* is by definition a quark with a mass much larger than Λ_{QCD} ($m_Q \gg \Lambda_{QCD}$): in the SM u, d, s are light quarks, whereas c, b and t are heavy quarks. For heavy quarks, the theory allows a perturbative description of the strong interactions and their description is almost trivial. On the other hand, systems with a heavy quark and other light quarks are more complicated. Fortunately, the typical momenta exchanged between heavy and light quarks is of the order Λ_{QCD}, that is not enough to resolve the quantum numbers of the heavy quark, such as flavor (mass) and spin orientation of the heavy quark [23]. Therefore, light quarks only experience the heavy quark color field, and in the rest frame of the heavy quark, the spin interaction decouples (vanish in the limit $m_Q \to \infty$). Also, as $m_Q \to \infty$, the heavy quark and the hadron have the same velocity (0 in the rest frame), and in this limit the solution of the field equations of QCD and the configuration of the light constituents are independent of m_Q.

To sum up, in the limit $m_Q \to \infty$, hadrons which differ only in the flavor or spin of the heavy quark have the same configuration of the light degrees of freedom. This provides relations between the properties of hadrons containing heavy quarks, for example, Λ_b^0 and Λ_c^+ baryons, plus corrections due to finite heavy quark masses. These relations are encoded in a $SU(2N_h)$ spin-flavor symmetry group (N_h the number of heavy-quarks flavors), called heavy quark symmetry (HQS) under which the *effective* strong interactions are invariant.[1]

2.4 Heavy quark effective theory

It is useful to write a theory where the effects of the heavy quarks become irrelevant at low energies (similarly to the Fermi theory, where the effects of the W and Z are disregarded), where the HQS breaking corrections are developed in a systematic and consistent way in powers of $1/m_Q$. Short distance effects (hard gluons) can be incorporated in this effective theory using renormalization group techniques in the form of Wilson coefficients (see section 2.2). Such simplified description is provided by the heavy quark effective theory (HQET), where a heavy quark interacts with light quarks by the exchange of soft gluons (virtual momenta are small, of the order of Λ_{QCD}). In this framework, heavy particle fields are "integrated out", leaving a non-local effective action that can be expanded in an OPE in powers of $1/m_Q$.

The are many good reviews of HQET. Here we follow Ref. [23]. Firstly, we observe that the propagator of a heavy quark can be expanded as follows:

$$\frac{i}{\not p - m_Q} = \frac{i}{v \cdot k} \frac{1 + \not v}{2} + \dots , \tag{2.9}$$

where $p_Q^\mu = m_Q v^\mu + k^\mu$, v is the quark velocity (very close to the hadron's velocity) and $k \sim \Lambda_{QCD} \ll m_Q$ is the residual momentum. As $m_Q \to \infty$, heavy quark flavor symmetry emerges. Also, the quark-gluon vertex appears between two propagators of the form

$$P_\pm = \frac{1 \pm \not v}{2}. \tag{2.10}$$

[1] An analogy of the flavor symmetry is the fact that different isotopes have similar chemistry, since the wave function of the electrons are almost independent of the heavy nucleus. Similarly, the spin symmetry resembles the degeneration of the hyperfine levels in atoms.

Spin symmetry emerges from the fact that $P_+\gamma^\mu P_+ = v^\mu P_+$ and $P_+^2 = P_+$ (just one γ matrix in the end). Therefore, it is convenient to write the heavy quark field $Q(x)$ in terms of velocity dependent fields and factorize m_Q:

$$Q = e^{-im_Q v\cdot x}\left[h_v(x) + H_v(x)\right], \tag{2.11}$$

where

$$\begin{pmatrix} h_v(x) \\ H_v(x) \end{pmatrix} = e^{im_Q v\cdot x} P_\pm Q(x). \tag{2.12}$$

After some algebra, the QCD Lagrangian for a heavy quark becomes

$$\mathcal{L}_Q = \bar{Q}(i\not{D} - m_Q)Q = \bar{h}_v iv\cdot D h_v - \bar{H}_v(iv\cdot D + 2m_Q)H_v + \text{interaction terms}, \tag{2.13}$$

where $D^\mu = \partial^\mu - ig_s T_a A_a^\mu$, g_s is the strong coupling constant and T_a are generators of the $SU(3)$ group. From this equation h_v describes apparently a massless field, whereas H_v "eats" twice the heavy quark mass. The HQET Lagrangian is constructed from h_v, eliminating H_v by using the equation of motion of Q, $(i\not{D} - m_Q)Q = 0$, and then looking for an effective Lagrangian that recovers the equation of motion for h_v:

$$\mathcal{L}_{\text{eff}} = \bar{h}_v iv\cdot D h_v + \bar{h}_v i\not{D}_\perp \frac{1}{2m_Q + iv\cdot D} i\not{D}_\perp h_v, \tag{2.14}$$

where $D_\perp^\mu = D^\mu - v^\mu v\cdot D$. Each derivative in the second term of Eq. 2.14 produces powers of k ($\ll m_Q$). Therefore, we can expand this term in powers of iD/m_Q and use the properties of the P_+ operator to show that:

$$\mathcal{L}_{\text{eff}} = \bar{h}_v iv\cdot D h_v + \frac{1}{2m_Q}\bar{h}_v(i\not{D}_\perp)^2 h_v + C_{\text{mag}}(\mu)\frac{g_s}{4m_Q}\bar{h_v}\sigma_{\mu\nu}G^{\mu\nu}h_v + \mathcal{O}(1/m_Q^2), \tag{2.15}$$

where $[iD^\mu, iD^\nu] = ig_s G^{\mu\nu}$ is the gluon field strength tensor and $\sigma_{\mu\nu} = i\left[\gamma_\mu, \gamma_\nu\right]/2$. Eq. 2.15 is the HQET effective Lagrangian. As expected, we recover HQS in the limit $m_Q \to \infty$, where only the first term remains. The second term describes the kinetic energy resulting from the residual motion of the heavy quark, whereas the third term represents the chromomagnetic coupling of the heavy quark spin to the gluon field. They violate flavor and spin symmetry, respectively. The coefficient of the chromomagnetic operator, $C_{\text{mag}}(\mu) = 1 + \mathcal{O}(\alpha_s)$, receives short distance corrections which are treated perturbatively in powers of the strong coupling constant, while the kinetic term is protected from quantum corrections by the Lorentz symmetry.

Finally, in the operators of the EW Lagrangian, the QCD field Q can be replaced in terms of h_v (using the equations of motion for h_v and H_v, and Eq. 2.11) to develop a series of higher-dimension operators that describe $1/m_Q$ effects.

2.5 Heavy quark expansion and b hadron lifetimes

If the heavy hadron H_b has multiple decay modes (or branches) with different final states, the total or *inclusive* decay rate of the particle is obtained summing the decay rates for all branches,

$$\Gamma(H_b) = \sum_f \Gamma(H_b \to f). \tag{2.16}$$

The *branching ratio* for each mode is given by

$$\mathcal{B}(H_b \to f) = \frac{\Gamma(H_b \to f)}{\Gamma(H_b)}, \tag{2.17}$$

and the inverse of $\Gamma(H_b)$ measures the mean lifetime of the H_b particle[1],

$$\tau(H_b) = \frac{1}{\Gamma(H_b)}. \tag{2.18}$$

To calculate the inclusive decay rate we can use the HQET technology developed in previous sections. This calculation relies on a hypothesis known as quark-hadron duality: the sum over all possible exclusive final states, which is necessary to determine the total lifetime, is equal to the sum over all possible final state quarks [24]. This assumption eliminates bound-state effects related to the individual properties of individual hadrons [23]. We use the optical theorem to relate the inclusive decay rate of a heavy hadron H_b to the imaginary part of the forward matrix element of the transition operator [9]:

$$\Gamma(H_b) = \frac{1}{2m_{H_b}} \langle H_b | \,\mathrm{Im}\; i \int d^4x\, T\{\mathcal{L}_{\text{eff}}(x), \mathcal{L}_{\text{eff}}(0)\}\, |H_b\rangle, \tag{2.19}$$

where $\mathcal{L}_{\text{eff}}$ is the effective $\Delta B = 1$ Lagrangian in the Fermi theory (Eq. 2.3),

$$\mathcal{L}_{\text{eff}} = -2\sqrt{2} G_F V_{cb} \sum_{d'=d,s;u'=u,c} V^*_{u'd'} \left[C_1(\mu) Q_1^{u'd'}(\mu) + C_2(\mu) Q_2^{u'd'}(\mu) \right] + \text{h.c.}, \tag{2.20}$$

[1] The lifetime depends on the Lorentz frame in which it is measured. In this work, we always measure lifetimes in the H_b rest frame.

and Q_1 and Q_2 are four-quark operators given by

$$Q_1^{u'd'}(\mu) = \bar{d}'_L \gamma_\mu u'_L \bar{c}_L \gamma^\mu b_L, \qquad Q_2^{u'd'}(\mu) = \bar{c}_L \gamma_\mu u'_L \bar{d}'_L \gamma^\mu b_L. \tag{2.21}$$

If we construct an OPE for these operators, the decay rate is given by [20]

$$\begin{aligned} \Gamma(H_b) &= \sum_k \frac{C_k(\mu)}{2m_b^k} \langle O_k^{\Delta B=0}(\mu) \rangle \\ &= \frac{G_F^2 m_b^5}{192\pi^3} \left\{ C_0 \langle \bar{b}b \rangle + C_2 \frac{\langle \bar{b} g_s \sigma^{\mu\nu} G_{\mu\nu} b \rangle}{m_b^2} \right. \\ &\quad \left. + 16\pi^2 \frac{\sum_i C_3^i \langle (\bar{q}_i \Gamma_i q_i)(\bar{b} \Gamma'_i b) \rangle}{m_b^3} + ... \right\}, \end{aligned} \tag{2.22}$$

where $\langle O \rangle \equiv \langle H_b | O | H_b \rangle / 2m_{H_b}$, q_i stands for light quarks (u,d,s), and Γ_i, Γ'_i denote spin and color structures of the four-quark operators. In the limit $m_Q \to \infty$, we recover the parton decay ($\langle \bar{b}b \rangle \to 1$, see Eq. 2.23), where the b quark decays weakly without feeling the light (spectator) quarks or gluons inside the hadron. The second term in the last expression of Eq. 2.22 describes the effect of the gluon field on the heavy quark through the chromomagnetic part of the gluon field. Hence, it depends on the spin of the heavy quark but not in the flavor of the light quarks. The third term finally gives an explicit dependence on the light quarks, and so on.

To evaluate the first (leading operator) and second (first correction) terms in Eq. 2.22, the matrix elements are expanded in powers of $1/m_b$ using HQET techniques (b_v fields, etc.). Then:

$$\langle \bar{b}b \rangle = 1 - \frac{\mu_\pi^2(H_b) - \mu_G^2(H_b)}{2m_b^2} + \mathcal{O}(1/m_b^3), \tag{2.23}$$

$$\langle \bar{b} g_s \sigma^{\mu\nu} G_{\mu\nu} b \rangle = 2\mu_G^2(H_b) + \mathcal{O}(1/m_b), \tag{2.24}$$

where

$$\mu_\pi^2(H_b) = \frac{1}{2m_{H_b}} \langle H_v(v) | \bar{b}_v (i\vec{D})^2 b_v | H_b(v) \rangle, \tag{2.25}$$

$$\mu_G^2(H_b) = \frac{1}{2m_{H_b}} \langle H_v(v) | \bar{b}_v \frac{g_s}{2} \sigma^{\mu\nu} G_{\mu\nu} b_v) | H_b(v) \rangle. \tag{2.26}$$

To evaluate these HQET matrix elements, we use the spectroscopic formula for heavy hadrons [23]:

$$m_H = m_Q + \bar{\Lambda} + \frac{\mu_\pi^2(H_Q) - \mu_G^2(H_Q)}{2m_Q} + ..., \tag{2.27}$$

where $\bar{\Lambda}$ is a parameter independent of the heavy quark mass and spin. Then, the splitting between the ground-state pseudoscalar ($J = 0$) and vector ($J = 1$) b mesons is:

$$\mu_G^2(B) = \frac{3}{4}(M_{B^*}^2 - M_B^2) \approx 0.36 \text{ GeV}^2. \tag{2.28}$$

In the Λ_b^0 the light quarks have total spin 0, hence $\mu_G^2(\Lambda_b^0) = 0$. This is the first difference between b mesons and baryons. The value $\mu_\pi^2(B)$ has to be calculated in a non-perturbative framework, still constrained to $\mu_\pi^2(B) > \mu_G^2(B)$ [20]. On the other hand, it can be shown that $\mu_\pi^2(\Lambda_b^0) = (0.01 \pm 0.03)$ using Λ_b^0 and Λ_c^+ in Eq. 2.27. It is useful to observe that the first and second matrix elements are equivalent to the Lorentz factor $\gamma^{-1} \approx 1 - \vec{p}^{\,2}/2m_b^2$, which decreases (increases) the decay width (lifetime) for a moving particle. In total, the first two terms in Eq. 2.22 account for a shift of $\sim 1-2\%$ in the ratio of Λ_b^0 and B^0 lifetimes.

Higher order terms are harder to calculate and lead to further differences between mesons and baryons. The third term in Eq. 2.22 is a special case since it is enhanced by the phase-space factor $16\pi^2$, inducing corrections of order $16\pi^2(\Lambda_{QCD}/m_b)^3 = \mathcal{O}(5 - 10)\%$ [9].

HQE is successful on describing the experimental results: the heavier the mass of the heavy quark, the smaller the variations in the lifetimes among different hadrons. Non-perturbative corrections arise at Λ_{QCD}^3/m_b^3 in mesons, and there are corrections at Λ_{QCD}^2/m_b^2 in baryons. Moreover, from HQE the following hierarchy is expected [23]:

$$\tau(\Lambda_b^0) < \tau(B_s^0) \approx \tau(B^0) < B^+. \tag{2.29}$$

which is also consistent with the experiments.

Evidently, the ratios of lifetimes give more precise estimations, since they allow several uncertainties and unknown parameters to cancel. For Λ_b^0 and B^0, the theoretical expression is of the form [9, 24]:

$$\frac{\tau(\Lambda_b^0)}{\tau(B^0)} \simeq 0.98 + \left(\frac{\Lambda}{m_b}\right)^3 (\Gamma_3^{(0)} + \frac{\alpha_s}{4\pi}\Gamma_3^{(1)} + ...) + \left(\frac{\Lambda}{m_b}\right)^4 (\Gamma_4^{(0)} + ...) + ..., \tag{2.30}$$

where $\Lambda \sim \Lambda_{QCD}$.

Early calculations of $\tau(\Lambda_b^0)/\tau(B^0)$ predicted values greater than 0.9. After much effort, recent calculations that include higher-order effects reduced this ratio to $0.88 \pm$

0.05 [8, 9]. In contrast to B mesons, NLO QCD corrections and reliable (lattice) values of the Λ_b^0 matrix elements are not yet available. Recently, the CDF Collaboration measured $\tau(\Lambda_b^0)/\tau(B^0) = 1.012 \pm 0.031$. Clearly, convergence between theory and experiment has not yet been reached. Even between experiments there is disagreement. More accurate predictions and more precise measurements are needed verify OPE, HQET and HQE assumptions.

2.6 Lifetime measurement overview

For unstable particles, the relationship between the total scattering cross section σ and the energy E usually appears as a resonance described by a Breit-Wigner function:

$$\sigma(E) = \sigma_0 \frac{(\Gamma/2)^2}{\left(E_0^2 - E^2\right) + (\Gamma/2)^2}. \tag{2.31}$$

The energy $E_0 = M_0 c^2$ corresponds to the maximum of the cross section σ_0 and Γ is the decay width (resonance width). Therefore, the lifetime of a hadron can be inferred from the inclusive decay width of its resonance.

Let us assume an unstable particle R that decays to two stable or metastable particles a and b in $p\bar{p}$ collisions. We call M_R the mass and τ_R the lifetime of particle R. We look for events that contain particles a and b, i.e., we search for processes such as $p + \bar{p} \to a + b + X$, where X is one or several particles. In a fraction of these events, the particle R is produced and decays to a and b, i.e., the reaction goes through an intermediate state containing R, $p + \bar{p} \to R + X \to a + b + X$. Then, the mass of the system $a + b$,

$$M_{ab} = \sqrt{(E_a + E_b)^2 - (\vec{p}_a + \vec{p}_b)^2}, \tag{2.32}$$

is expected to have a Breit-Wigner distribution centered at M_R with width $\Gamma_{ab} = 1/\tau_R$. On the other hand, if there is not such intermediate state, M_{ab} can take any value allowed by relativistic conservation laws. A schematic view of the M_{ab} distribution is showed in Fig. 2.3, where the Breit-Wigner peak lies on the smooth non-resonant background.

In general, the peak is overshadowed by non-resonant backgrounds and it is the (hard) task of people working on these analyses to extract the signal peak. In addition

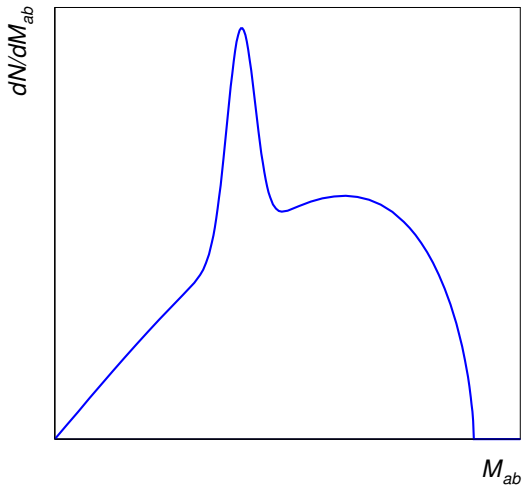

Figure 2.3: Schematic mass distribution of a resonant process.

to these "physics" backgrounds, people have to deal with combinatorial backgrounds arising from multiple primary interactions (pile-up), fake reconstructed particles due to combinatorics produced by the track finding algorithm, and incorrect association of final state particles due to the lack of dedicated particle identification detectors. Unfortunately, the limiting factor to extract a lifetime is not the amount of background. First, it is almost impossible to reconstruct all possible decay channels, which are necessary to extract the real lifetime. Second, the measured width is the convolution of the natural width and the experimental resolution. The method described here simply does not work if the latter is much wider than the former, as is the case for Λ_b^0 baryons reconstructed in the DØ experiment. Instead, we measure the lifetime directly from the distribution of the distance traveled by the Λ_b^0 particles before decaying to some specific final state, taking advantage of the relativistic boost that allows a measurable distance in the laboratory, and use the resonance (the width is basically the detector resolution) to distinguish between signal and background decays.

The DØ experiment can measure the Λ_b^0 lifetime in fully reconstructed (non-leptonic) decays [10] and semi-leptonic decays [11]. The latter approach benefits from the large statistics (muon trigger); however, it makes extensive use of Monte-Carlo simulations to correct the reconstructed momentum (due to the missing neutrino) of the Λ_b^0 baryon

and to estimate possible backgrounds.[1] CDF's $\Lambda_b^0 \to \Lambda_c^+ \pi^-$ measurement takes advantage of an impact parameter and displaced-vertex based two-track trigger, which has no equivalent at DØ.[2] In this work, we measure the Λ_b^0 lifetime in the fully reconstructed decay $\Lambda_b^0 \to J/\psi\,\Lambda^0$. The strength of the $\Lambda_b^0 \to J/\psi\,\Lambda^0$ lifetime analysis is that it almost does not rely on Monte-Carlo simulations and the DØ data is not biased by the online (trigger) selection.

[1] Despite the large statistics in semileptonic decays, one ends with a systematic uncertainty that is twice compared to fully reconstructed decays.

[2] CDF's $\Lambda_b^0 \to \Lambda_c^+ \pi^-$ analysis (1) uses Monte-Carlo simulation to fix the background components (in form of partially and fully reconstructed b decays), and (2) corrects for the efficiency induced by the trigger, which is a very involved and uncertain process based on simulations to account for the impact parameter and vertex displacement of the two tracks, particle identification, Λ_b^0 polarization, etc.

Chapter 3

Experimental apparatus

This chapter contains a general description of the Tevatron Collider and the accelerator chain, followed by a more detailed description of the DØ detector and subsystems that are relevant for the measurement of the Λ_b^0 lifetime.

3.1 The Tevatron Collider

The Tevatron was the world most powerful proton-antiproton collider before it shut down for good on September 29, 2011 [25] and was the highest energy collider until 2009 when the Large Hadron Collider (LHC) initiated operations. The Tevatron complex is located at the Fermi National Accelerator Laboratory (Fermilab) just east of Batavia, Illinois, in the United States. It accelerated beams of protons and antiprotons to 99.999954% of the speed of light around a 6.3 km (3.9 mi) circumference (they circled the tunnel $\sim 47,000$ times per second!). Each beam was accelerated to 980 GeV and they collided at the centers of two 5,000 ton detectors, DØ and CDF. At the moment, the Tevatron continues to send beams into stationary targets to produce neutrino beams and parts of it will be reused for future experiments. A schematic view of the Tevatron is shown in Fig. 3.1.

3.1.1 The Accelerator chain

Before high energy collisions, protons and antiprotons were created and accelerated through various stages [25] as described below.

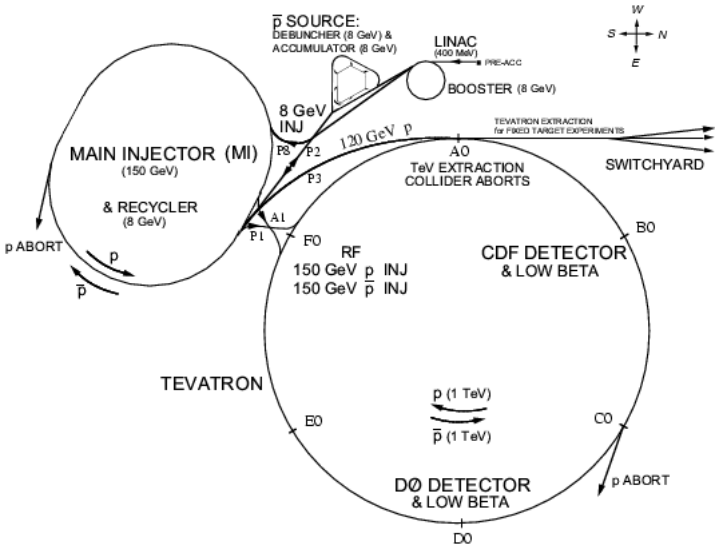

Figure 3.1: Schematic view of the Fermilab Tevatron Collider.

3.1.1.1 Pre-accelerator

To create protons, hydrogen gas was injected into the ion source to produce negative hydrogen ions (H^-). The first stage of acceleration was performed by a Cockcroft-Walton pre-accelerator that increased the H^- ions energy from 25 to 750 keV using a positive voltage.

3.1.1.2 Linac

After the pre-acceleration, the H^- beam was sent to a 150 meter (500 feet) long linear accelerator (linac) that ramped the ions energy up to 400 MeV, about 70% of the speed of light, by using a 116 MeV Alvarez Drift-Tube accelerator and a 400 MeV side-coupled linac equipped with 7 radio-frequency (RF) cavities [26]. A focusing-defocusing quadrupole magnets (FODO) lattice was used to compensate for beam dispersion caused by pulsed acceleration. Before moving to the Booster, the ions passed through a carbon foil that removed the electrons in order to leave just protons.

3.1.1.3 Booster

The Booster was a synchrotron, i.e., a circular accelerator with a lattice of dipole and quadrupole magnets used to bend and focus the beam. The protons were accelerated by RF cavities. After approximately 20,000 revolutions, the proton beam was boosted up to 8 GeV and then transfered into the Main Injector.

3.1.1.4 Main Injector

The Main Injector was a multipurpose synchrotron ring that used RF acceleration. It was capable to accelerate protons up to 150 GeV for injection into the Tevatron (nowadays it is only used to send beams to neutrino experiments). In a different mode, it could create 120 GeV protons for antiproton production, described in section 3.1.1.5. And, finally, it could handle antiprotons coming from the Recycler (section 3.1.1.6) and accelerate the resulting beam to 150 GeV to be transfered into the Tevatron.

In the Main Injector, the beam was grouped in 12 (4) bunches of $\sim 10^{11}$ ($\sim 10^{10}$) protons (antiprotons) and transfered to the Tevatron in a single revolution. The same process was repeated until having 36 proton and antiproton bunches in the Tevatron.

3.1.1.5 Antiproton source

Proton bunches at 120 GeV were steered from the Main Injector to a fixed Ni target. These collisions produced various secondary particles, including antiprotons which were focused by a Li lens and selected by magnetic bending. Resulting 8 GeV antiprotons were transfered to the Debuncher, which was a small synchrotron that stabilized the orbit and removed the bunch structure of the beam. Then, in the same tunnel, the beam was injected into a second synchrotron, called the Accumulator, where antiprotons were collected and "cooled" (reduced emittance and increased brightness). On average, 16 million protons were needed to produce a single antiproton. After collecting enough antiprotons ($\sim 10^{12}$), they were sent to the Recycler.

3.1.1.6 Recycler

The Recycler and the Main Injector shared the same tunnel. The Recycler was used for additional cooling and (gradual) accumulation of antiprotons before they were

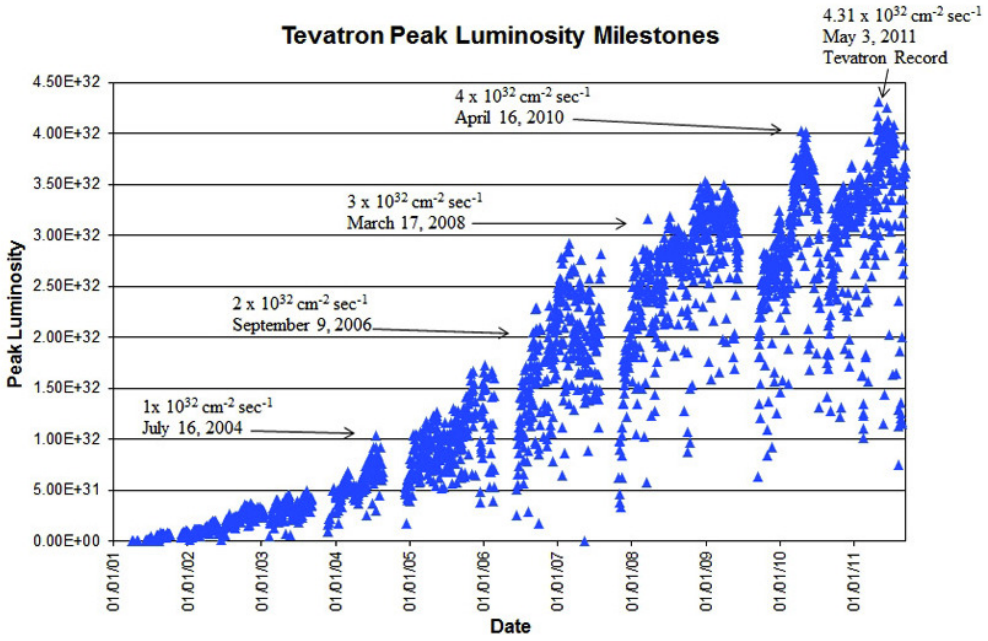

Figure 3.2: Peak luminosity during the Tevatron Run II [27].

injected into the Tevatron. The Recycler did not accelerate beams, but a FODO lattice (dipole magnets in the middle) and RF cavities were used to steer, capture and stabilize the beam, and to produce bunches of antiprotons.

3.1.1.7 Tevatron

The Tevatron accelerated bunches of protons and antiprotons in opposite directions from 150 to 980 GeV. Superconducting NbTi dipole and quadrupole magnets operating at −268 °C (−450 °F) were used to bend and focus the beams inside a vacuum pipe, while the acceleration was provided by RF cavities. The bunches were divided in 3 trains of 12 bunches. Each bunch was separated by 396 ns and each train by 2.617 μs. Proton and antiproton beam paths were controlled by electrostatic separators, which brought them to collision at only two intersection points, just where the CDF and DØ detectors are still located.

The luminosity is a measure of the number of collisions that occurs each second. On May 3, 2011, the Tevatron set an initial luminosity record of 431 $\mu b^{-1}s^{-1}$ [27], as seen

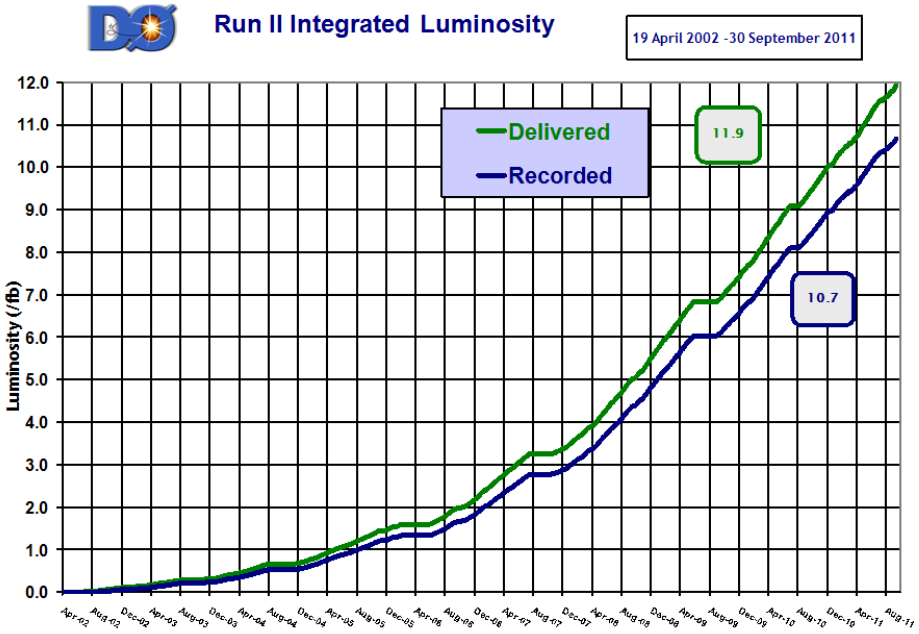

Figure 3.3: DØ Run II integrated luminosity [28].

in Fig. 3.2.[1] The luminosity decayed almost exponentially between the first collisions of quality beams until the beams in the Tevatron were dumped, a period called Store that used to last about 16-20 hours.

From April 19, 2002 to September 30, 2011, a period called Run II, DØ recorded 10.7 fb^{-1} out of 11.9 fb^{-1} of integrated luminosity delivered by the Tevatron, as seen in Fig. 3.3. After data quality studies, it was found that 10.4 fb^{-1} of data were useful for physics analyses. To give an idea of the magnitude of the data recorded, 1 fb^{-1} represents about 50 trillion $p\bar{p}$ collisions [29].

3.2 The DØ detector

In this section we give a general description of the DØ central tracking system, muon detector, magnetic fields (solenoid and toroids), and trigger, which are relevant subsystems to achieve the measurement of the Λ_b^0 lifetime. More briefly we mention

[1] 1 μb $= 10^{-30}$ cm^2.

other subsystems, such as pre-shower detectors, calorimeters and luminosity monitors. A detailed description of the DØ detector can be found in Refs. [30, 31, 32, 33].

3.2.1 DØ detector overview

The DØ detector was built to study $p\overline{p}$ collisions at a center-of-mass energy of $\sqrt{s} = 1.96$ TeV during the Tevatron Run II (it operated at $\sqrt{s} = 1.8$ TeV during Run I, from 1992 to 1996). Just to mention some accomplishments by the DØ Collaboration, it led to the discovery of the top quark and measurement of its mass, discovery of single top quark production, a precise measurement of the W boson mass, first observations of the Ξ_b^- and Ω_b^- baryons, and restrictions on the mass of the Higgs boson [27]. After the definitive Tevatron shutdown, DØ continued to operate for another 6 months for calibration purposes. The DØ assembly area is now utilized to put together new experiments. The DØ detector will not be (completely) disassembled; instead, it is planned for public exhibition. A lot of data have not yet been analyzed. Therefore, for the description of the DØ detector, from now on, I will use the present tense.

The DØ detector is depicted in Fig. 3.4. It includes a central tracking system (section 3.2.2), composed by a silicon microstrip tracker (SMT, section 3.2.2.1) and a scintillating-fiber tracker (section 3.2.2.2) located within a 2 T solenoidal magnet (section 3.2.2.3). The SMT is able to identify displaced vertices, helpful for b-quark tagging. The solenoidal magnetic field allows precision momentum measurement of charged particles. Preshower detectors, for improved electron and photon identification, are located beyond the central tracking system, between the solenoidal magnet and the central calorimeter and in front of the forward calorimeters. Central and forward muon spectrometers (section 3.2.3) surround the calorimeters, and consist of three layers of drift tubes and scintillation trigger counters. A 1.8 T toroidal iron magnet (section 3.2.3.1), located outside the innermost layer of the muon detector, provides a stand-alone muon-system momentum measurement and is used to reject K/π decays. Finally, luminosity monitors, located in front of the end calorimeters, determine the Tevatron luminosity at the DØ interaction region and provides a fast measurement of the position of the interaction vertex along the beams direction.

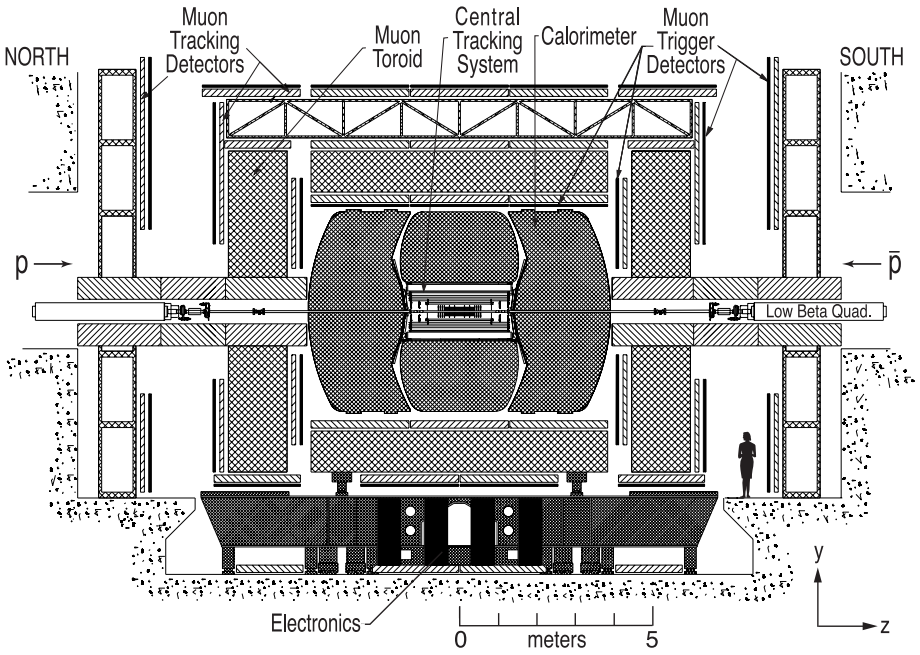

Figure 3.4: Side view of the DØ detector [30].

As usual, we use a right-handed coordinate system in which the z-axis is along the proton direction and the y-axis is upward, as shown in Fig. 3.4. We will frequently use the word "transverse" referring to quantities measured in the plane perpendicular to the z direction. Spherical coordinates (r, ϕ, θ) are also used for analysis and detector description. The r coordinate denotes the perpendicular distance from the z-axis. Instead of the polar angle, it is common to use the pseudorapidity,

$$\eta = -\ln\left[\tan\left(\theta/2\right)\right], \tag{3.1}$$

which is the limit of the true rapidity, $y = 1/2 \ln\left[\left(E + p_z c\right) / \left(E - p_z c\right)\right]$, as $\left(mc^2/E\right) \to 0$. The term "forward" is used to describe the regions at large $|\eta|$ (> 1). Using this convention, we measure particle momenta in terms of transverse momentum (p_T), ϕ and η:

$$\vec{p} = (p_x, p_y, p_z) = (p_T \cos\phi, p_T \sin\phi, p_T \sinh\eta), \tag{3.2}$$

$$|\vec{p}| = p_T \cosh\eta. \tag{3.3}$$

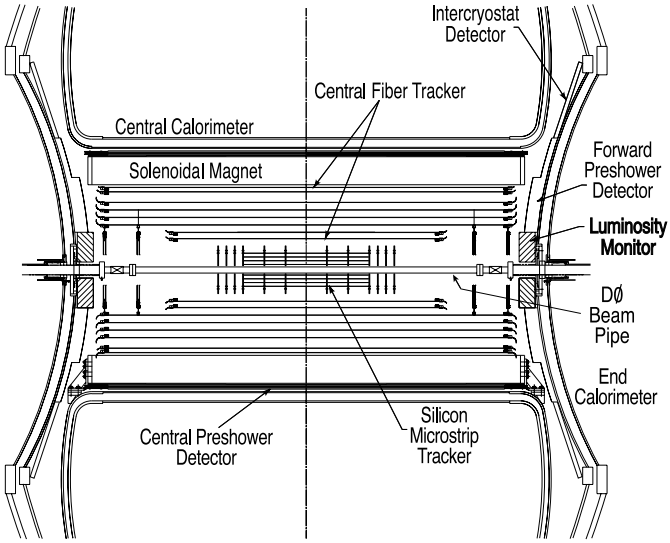

Figure 3.5: Cross sectional view of the DØ tracking system [30].

3.2.2 Central tracking

The central tracking system is shown in Fig. 3.5 and consists of the SMT and the central fiber tracker (CFT) surrounded by a solenoidal magnet. It surrounds the DØ beryllium beam pipe, which has an outer radius of 1.5 cm. It allows a precise determination of the primary interaction vertex (PV), impact parameter (IP) of charged tracks and p_T.

3.2.2.1 Silicon microstrip tracker (SMT)

A diagram of the SMT is shown in Fig. 3.6. It provides both tracking and vertexing over almost the full η coverage of the muon system (section 3.2.3). The SMT consists of barrel modules interspersed with (F-)disks in the central region and large-diameter (H-)disks in the forward regions. The barrels primarily measure the $r-\phi$ coordinate; together with the CFT, they are used to reconstruct vertices at small values of z. The disks give measurements of $r-z$ and $r-\phi$ coordinates, making possible the reconstruction of vertices at high z.

There are 6 barrels with centers at $|z| = 6.2$, 19.0 and 31.8 cm, each one with 4 layers located from $r = 2.7$ to 10.5 cm, that give support to silicon modules called

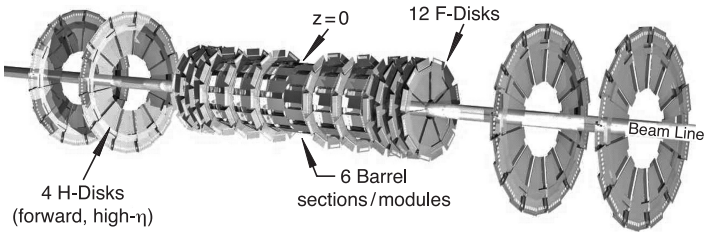

Figure 3.6: Isometric view of the SMT detector [30].

"ladders". Ladders consist of a combination of single-sided (SS), double-sided (DS) and double-sided double-metal (DSDM) silicon wafer technologies, with are characterized by their crystal orientation, thickness, and angle between p and n sides of DS sensors ($> 0^\circ$ are called stereo sensors; otherwise, axial sensors). An F-disk, composed of DS wedge silicon detectors, caps each barrel at $|z| = 12.5$, 25.3, 38.2 cm. In addition, there are three F-disks located forward, in each side, at $|z| = 43.1$, 48.1, 53.1 cm. In the far forward regions, two H-disks at $|z| = 100.4$, 121.0 cm, composed of back-to-back SS wedges, provide tracking at high $|\eta|$. In total, there are 792,576 channels read out by custom-made 128-channel SVXIIe readout chips. These signals are used by the Level 2 and 3 trigger systems (section 3.2.4) to trigger on displaced vertices.

A new inner layer, called Layer 0 (L0), was inserted for the second part of the DØ Run II, named Run IIb, that started in June 2006. Located at $r = 1.6 - 1.8$ cm, the design of L0 was thought to improve the resolution of the Run IIa SMT detector and to provide more robust tracking and pattern recognition at higher luminosities [32].

3.2.2.2 Central fiber tracker (CFT)

The CFT is a set of 835 μm-diameter scintillating fibers placed on top of eight concentric support cylinders, as shown in Fig. 3.7. The cylinders are located from $r = 20$ to 52 cm, the two inner-most are 1.66 m long (bounded by the H-disks), and the outer six are 2.52 m long covering up to $|\eta| \lesssim 1.7$. On each cylinder, a "doublet" layer (the second layer of the doublet offset by 0.5 mm from the first layer) of fibers is oriented along z (axial layer) and a second doublet layer at a stereo ϕ angle of $+3^\circ(u)$ or $-3^\circ(v)$ (stereo layers). From inside to outside, the fiber doublet orientation

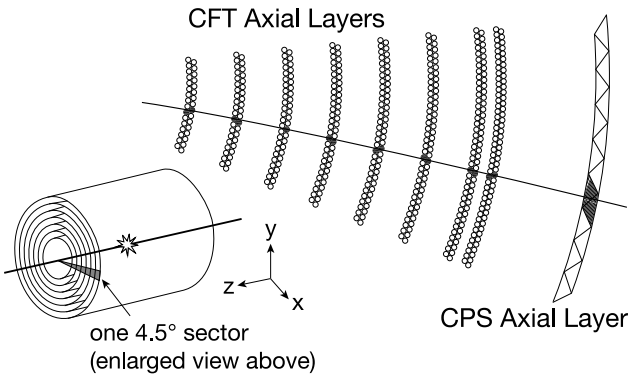

Figure 3.7: Transverse schematic view of the CFT detector [30].

is $zu - zv - zu - zv - zu - zv - zu - zv$. The scintillating fibers are connected to clear fiber waveguides to transfer the scintillation light to visible light photon counters for read out, making in total 76,800 readout channels. These signals are used by the Level 1 hardware trigger (section 3.2.4) to trigger on track p_T in sectors of 4.5°, and this information is sent to the global Level 2 trigger. The Level 3 uses the full CFT readout information.

3.2.2.3 Solenoidal magnet

The superconducting solenoidal magnet curves the trajectories of charged particles to allow a precise measurement of the momentum in the transverse plane. As shown in Fig. 3.8, it provides a central field of 2 T. The polarity of the magnet was reversed regularly in order to reduce detector asymmetry effects.[1] The overall thickness of the solenoid is about one radiation length ($1X_0$) at $\eta = 0$.

3.2.3 Muon detector

For muon detection, DØ has a central muon system that uses proportional drift tubes (PDTs), trigger scintillation counters and toroidal magnets, and a forward muon system with mini drift tubes (MDTs) rather than PDTs, scintillation counters, forward

[1] The periodic reversal of the solenoid and toroid polarities proved to be really useful in the beautiful DØ measurement of the like-sign dimuon charge asymmetry in semileptonic b-hadron decays [Phys. Rev. Lett. 105, 081801 (2010)].

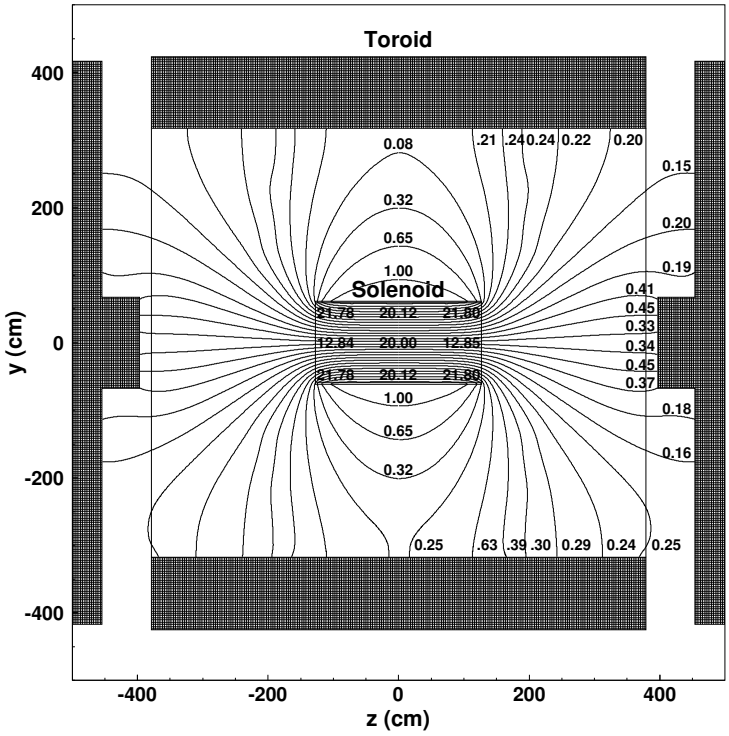

Figure 3.8: A $y-z$ projection of the DØ magnetic field with both solenoidal and toroidal magnets operating at full current [30]. The field is measured in kG.

toroids and beam pipe shielding. The central muon system covers $|\eta| \lesssim 1$ and the forward system extends the coverage up to $|\eta| \approx 2$. The distribution of the muon wire chambers (PDTs and MDTs) and scintillation counters is shown in Fig. 3.9 and will be described in the following subsections.

The scintillation counters are used for triggering; wire chambers are used for precise coordinate measurements and also for triggering. Both technologies help to reject background: the scintillator with timing information, and the wire chambers with track segments. The toroidal magnets allow an independent muon momentum measurement which enables a low-p_T cutoff in the Level 1 muon trigger, permits a cleaner matching with central detector tracks, rejects π/K decays, and improves the momentum resolution for high momentum muons.

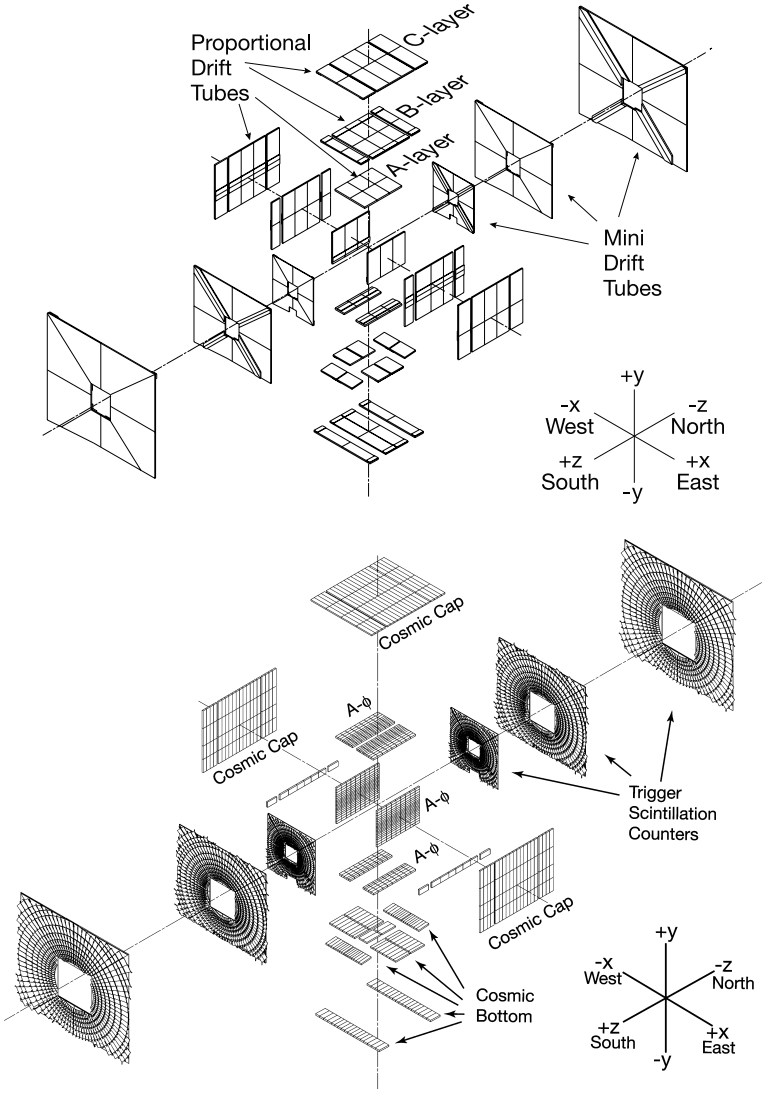

Figure 3.9: Muon detectors [30]. Top: muon wire chambers. Bottom: muon scintillation counters.

3.2.3.1 Toroidal magnets

The central toroid is a 1.1 m thick square annulus, located at about $r = 3.2$ m from the Tevatron beamline. It is divided in three parts to allow access to the inner parts of the detector: center-bottom, and two C-shaped sections. On the other hand, there are two end (forward) toroids, located at $4.5 \leq z \leq 6.1$ m and $r = 4.3$ m from the beamline. The internal fields in the central toroid are approximately 1.8 T and those in the end toroids are approximately 1.9 T. As with the solenoidal magnet, the toroids polarity was regularly reversed during the DØ Run II.

3.2.3.2 Central muon system

The central muon system is composed of the central toroid (section 3.2.3.1), PDT chambers, the cosmic cap and bottom scintillation counters, and the $A\phi$ scintillation counters.

There are three layers of PDT chambers. The inner-most, called A-layer, is located inside the central toroid. The other two layers, B- and C-layers, are located outside. A PDT is a rectangular extruded aluminum tube, called drift-cell, filled with a mixture of 84% argon, 8% methane, and 8% CF_4. Each drift-cell has an anode wire at the center. Vernier cathode pads above and below the wire determine the hit position along the wire.[1]

A set of scintillation counters, called the cosmic cap and cosmic bottom, is installed on the top, sides and bottom of the C-layer. Scintillation counters are fast enough to allow the association of a muon in a PDT with the correct bunch crossing and to discriminate against the cosmic ray background.

The $A\phi$ scintillation counters cover the A-layer. They provide fast triggering, muon identification and out-of-time backscatter rejection from the forward direction. Together with the CFT, it is possible to trigger at Level 1 (section 3.2.4) for high-p_T single muon and low-p_T dimuon triggers.

[1] Vernier pads were only fully instrumented on the A-layer, and about 10% on B/C-layers for aging studies, since they were expensive and did not improve the resolution for tracks passing all three layers.

3.2.3.3 Forward muon system

The forward muon system is composed of the end toroids (section 3.2.3.1), MDT chambers, scintillation counters and shielding around the beam pipe.

The function of the MDT chambers is essentially the same as the PDT chambers in the central region. MDTs are chosen because they provide better resolution and radiation hardness than the PDTs. There are three layers of MDTs (A, B and C), with the A-layer inside the end toroids. MDTs have 8 drift cells, covered with a stainless steel foil and inserted into PVC sleeves, and filled with a mixture of 90% CF_4 and 10% methane.

The muon trigger scintillation counters are installed over the three MDT layers. They provide good time resolution, background rejection and high muon detection.

Finally, the shielding to reduce non-muon background in the muon system consists of layers of iron (hadronic and electromagnetic absorber), polyethylene (neutron absorber) and lead (gamma rays absorber) in a steel structure around the beam pipe and low-beta quadrupoles.

3.2.4 Trigger

More than 2.5 million proton-antiproton bunch crossings occurred at DØ every second during a normal Store. Given the total SM cross section of the Tevatron collider, $\sigma_{tot} \approx 10^8$ nb [34], we expected on the order of 1 to 10 collision in each bunch crossing (pile-up). Since in general not every high energy collision leads to interesting physics[1] and it is also impossible to save all that information due to limited disk space (something similar happens at the LHC), the DØ experiment implements three trigger levels (Level 1 to Level 3, or L1, L2 and L3). Each succeeding level examines fewer events but in greater detail and complexity. Events rejected by any of the trigger levels are permanently lost. Accepted events are buffered at each level to prevent further lost of data. During Tevatron collisions, the available trigger bandwidth had to be divided into different kind of physics and interests, without excluding the possibility of totally new

[1] For calibrations purposes, 1 out of 800,000 beam crossings were randomly recorded (zero-bias trigger). Similarly, 1 out of 700,000 collisions, identified as signal coincidences in the luminosity monitors at the expected time, were saved to disk (minimum-bias trigger).

and unexpected physics. For some physics analyses, such as b physics studies, things got more complicated and inefficient (e.g. pattern recognition) at higher luminosities due to the busy environment.

The L1 consists of hardware elements that process signals from the luminosity monitors, calorimeter, muon system and fiber tracker. The requirements at L1 are very basic, such as energy depositions or hit patterns associated with tracks above a preset momentum threshold (see also footnote 1 in page 32). The set of decisions (also called triggers) taken at L1 reduces the event rate from 2.5 MHz to about 2 kHz.

The L2 is composed by serial or parallelized CPU-based cards or programmable logic based cards for each detector subsystem, and a global processor for integration of the data. The L2 is able to identify physics objects such as jets, electrons, photons, missing energy in the calorimeter, muons and charged tracks (with certain p_T, ϕ, isolation or impact parameter). The global processor analyze all objects received from the detector subsystems and their correlations, to reduce the event rate to about 1 kHz.

Finally, these data are received by the L3 to be analyzed in much more detail. This process is performed in parallel by nearly 500 computers, programmed with complex algorithms. Decisions at L3 are based on complete physics objects and on the relationships between them (vertices, angular separations, etc.).

During Tevatron collisions, to further reduce the rate to an acceptable level, about 100 Hz, L3 triggers had to be "pre-scaled"; for example, 9 out of 10 events with two good muons and $p_T > 2$ GeV/c were randomly rejected between 260 and 310 $\mu\text{b}^{-1}\text{s}^{-1}$.

Chapter 4

Event reconstruction

The goal of this chapter is to show how we reconstruct Λ_b^0 candidates decaying to a J/ψ meson and a Λ^0 baryon. With more detail we shall see that a J/ψ candidate is reconstructed with two good quality oppositely charged muons candidates forming a good vertex. Analogously, a Λ^0 candidate is reconstructed with two oppositely charged tracks, associated with a proton and a pion, converging to a common point. Then, the four-momenta of the J/ψ and Λ^0 candidates are combined to form a Λ_b^0 candidate. The topology of the Λ_b^0 decay chain is shown Fig. 4.1a. Due to the similar topology, we also reconstruct $B^0 \to J/\psi\, K_S^0$ decays, where the K_S^0 meson decays to two charged pions, as shown in Fig. 4.1b.

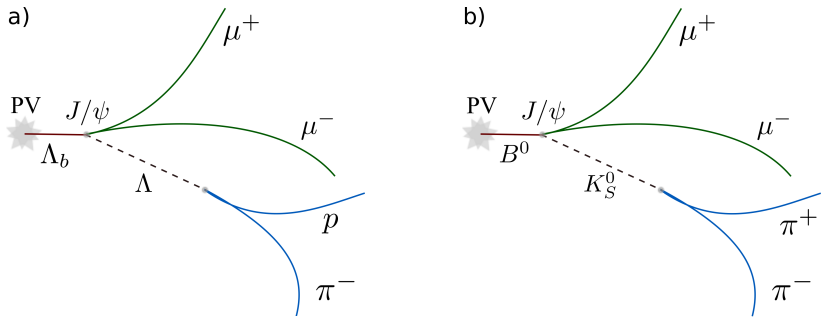

Figure 4.1: Topology of the decays a) $\Lambda_b^0 \to J/\psi\,\Lambda^0$ and b) $B^0 \to J/\psi\, K_S^0$, with $J/\psi \to \mu^+\mu^-$, $\Lambda^0 \to p\pi^-$ and $K_S^0 \to \pi^+\pi^-$.

4.1 Reconstruction software overview

DØ developed a program called DØReco to reconstruct objects used in physics analyses [30]. Since it is a very time consuming process, it must be run on thousands of computers. Every event is divided in "chunks" containing the raw detector signal. DØReco processes these chunks, taking into account calibrations, and then returns more chunks associated with each type of reconstructed object, such as muons, electrons or vertices. The most CPU intensive DØReco process is the reconstruction of global tracks from signals in the SMT and CFT by using several tracking algorithms. Since we are looking for a very specific decay, we use directly a program called AATrack (AA stands for Alternative Algorithm) [35] to reconstruct our secondary vertices. AATrack is a DØReco subroutine used to reconstruct primary vertices (PV) and one of the several algorithms used to reconstruct tracks. We use AATrack extensively because it can identify low p_T tracks which are useful for our analysis (tracks reconstructed by all algorithms are merged and filtered). Moreover, AATrack is the most efficient algorithm for high impact parameter[1] (IP) track candidates, such as those coming from Λ^0 and K_S^0 decays.

4.2 Track reconstruction

The basic elements to reconstruct track candidates are the signals obtained from the strips and fibers of the SMT and CFT detectors. Charged particles produce signals in several neighboring strips, from which AATrack forms clusters called "hits". The algorithm starts by taking an axial hit on the innermost layer and then tests hits at larger radii layers, as shown in Fig. 4.2. A second hit on a higher layer is chosen if the azimuthal angle between hits does not exceed ϕ_{max}. A third hit is accepted if the radius of the circle drawn through the three hits is larger than R_{min} and the IP, measured from the beam-spot[2], is smaller than b_{max}. More hits can be added to the three-hits seed track if they fulfill a χ^2 requirement. Also, every axial hit has multiple associated

[1] The impact parameter of a track is defined as the transverse distance of closest approach (DCA) of the track to the primary vertex point.

[2] The beam-spot is the transverse beam position averaged over multiple beam crossings.

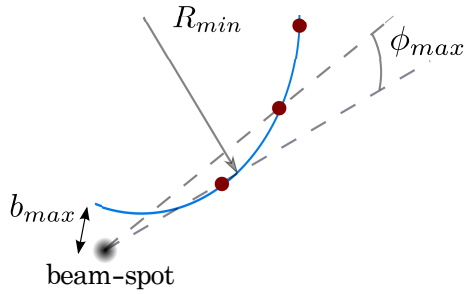

Figure 4.2: Track reconstruction and parameters used to accept or reject a tree-hits seed track.

stereo hits, and all combinations have to be tested. R_{min} is related to the p_T threshold of tracks by the relation

$$p_T^{min}[\text{GeV}] = 0.3 \cdot B[\text{T}] \cdot R_{min}[\text{m}], \tag{4.1}$$

where B is the magnetic field (~ 2 T). As we shall see in section 4.2.1, various values of R_{min}, ϕ_{max} and b_{max} were studied for track reconstruction.

Charged particles decaying far away from the PV (e.g. those coming from Λ^0) are expected to have several missing hits on inside layers, or "backward misses". Missing hits occurring in between hits on the track, or "inside misses", are typical of fake tracks. Missing hits on layers outside the last associated hit on the track are called "forward misses". The track finding algorithm stops for the current track hypotheses if there are no more outward layers to test or if there are more than 3 forward misses. The track hypothesis is rejected if it fails any of the following requirements:

- the total number of hits (N_{tot}) are at least five times the total misses (N_{miss});
- less than six forward and backward misses;
- in average, less than four inside misses, and less than three in the SMT;
- at least four stereo hits.

This procedure is repeated for every allowed initial combination of three hits. A similar algorithm is implemented starting from the outermost CFT layer to smaller radii layers.

To reduce the fake rate, low quality tracks with too many shared hits with higher quality tracks are rejected. Tracks are ordered first by N_{tot}, then by N_{miss}, and finally by χ^2. Starting with the highest quality track, a track is accepted if the total number of shared hits (N_{sh}) between tracks of higher quality is less or equal to $\frac{2}{3}N_{tot}$. This requirement is tightened to $N_{sh} \leq \frac{1}{5}N_{tot}$ if $N_{tot} - N_{sh} \leq 3$. The process is repeated a second time, but this time N_{tot} is replaced by $2N_{tot}$ if the track has a small IP with respect to the PV reconstructed with the current pool of tracks (see section 4.3).

4.2.1 Extended reconstruction

The observation of the Ξ_b baryon at DØ [37] had been impossible without a set of modifications to the AATrack algorithm that allow tracks with IP greater than 2.5 cm to be reconstructed in DØReco. This "extended" reconstruction increases the acceptance of Λ^0 and K^0_S candidates, which generally decay to tracks with low p_T and high impact parameter.

Major changes in the DØ detector occurred during 2005-2006. The DØ Run II was divided in Run IIa (before 2005) and Run IIb (after June 2006). To deal with the high track multiplicity of the Run IIb environment, the Collaboration decided to raise the p_T^{min} of tracks from $\approx$ 180 to $\approx$ 450 MeV/c, in fact killing most of the Λ^0 signal (see section 4.6.1). To perform this analysis, all events with dimuon candidates in Run IIa and Run IIb, with invariant mass between 2.0 to 4.2 GeV/c^2, were reprocessed with the extended algorithm [38]. The parameters used for track reconstruction were modified to allow tracks with p_T above $\approx$ 120 MeV/c. Table 4.1 summarizes these changes.

Table 4.1: Summary of parameters used in the standard and extended reconstruction algorithms.

Parameter	Standard Run IIa	Standard Run IIb	Extended Run II (a-b)
ϕ_{max}	0.08	0.08	0.20
R_{min}	30 cm	75 cm	20 cm
b_{max}	2.5 cm	2.5 cm	10 cm

The data reprocessing last about 4 months in thousands of CPUs.[1] Many technical issues, such as memory and disk consumption and program crashes, had to resolved during that period. We found additional unexpected problems for the Monte-Carlo reprocessing that took us more time to overcome. These problems were decisive in our optimization strategy, which maximize the Λ_b^0 peak significance in data instead of using Monte-Carlo estimates.

4.3 Primary vertex reconstruction

The primary vertex (PV) reconstruction algorithm is described in detail in Ref. [36]. Tracks within a distance of closest approach (DCA) of 2 mm to the beam-spot are used to fit a common vertex using the beam-spot as a constraint. The accuracy of this PV is improved in a second iteration, by using the DCA to the first pass PV instead of the beam-spot. We require at least one PV formed from at least 5 tracks to accept the event.

The inclusion of tracks from the decay of a b hadron can bias the PV towards the b hadron decay vertex. After the reconstruction of the Λ_b^0 and B^0 candidates (see next sections), daughter tracks are excluded in a third and final recalculation of the PV.[2] The distance measured in the transverse plane between the third and second iteration PV is ~ 3 μm overall.

We generate a Monte-Carlo sample of $\Lambda_b^0 \to J/\psi\,\Lambda^0$ decays, that includes the simulation of the detector response, and is reconstructed with the same algorithms as in data (see Appendix A). In Fig. 4.3 we observe that the mean of the residuals between the reconstructed PV and the true (generated) PV is consistent with zero in each of the three spatial components, x, y and z, and hence, the final reconstructed PV is unbiased. As expected, due to the design of the DØ central tracking, the resolution is better in the $x-y$ (transverse) plane than in z direction.

[1] The extended algorithm was modified several times in an effort to fix errors in the code, adjust reconstruction parameters, and improve several subroutines. For these reasons, all data available were reprocessed each year, from 2007 to 2011. As we have already mentioned, the last reprocessing took about 4 months and an equivalent time in order to certify these data.

[2] In practice, only muons are excluded. Tracks with small IP, coming from a Λ^0 or a K_S^0 candidates, are discarded by our selection requirements, mainly to reduce backgrounds.

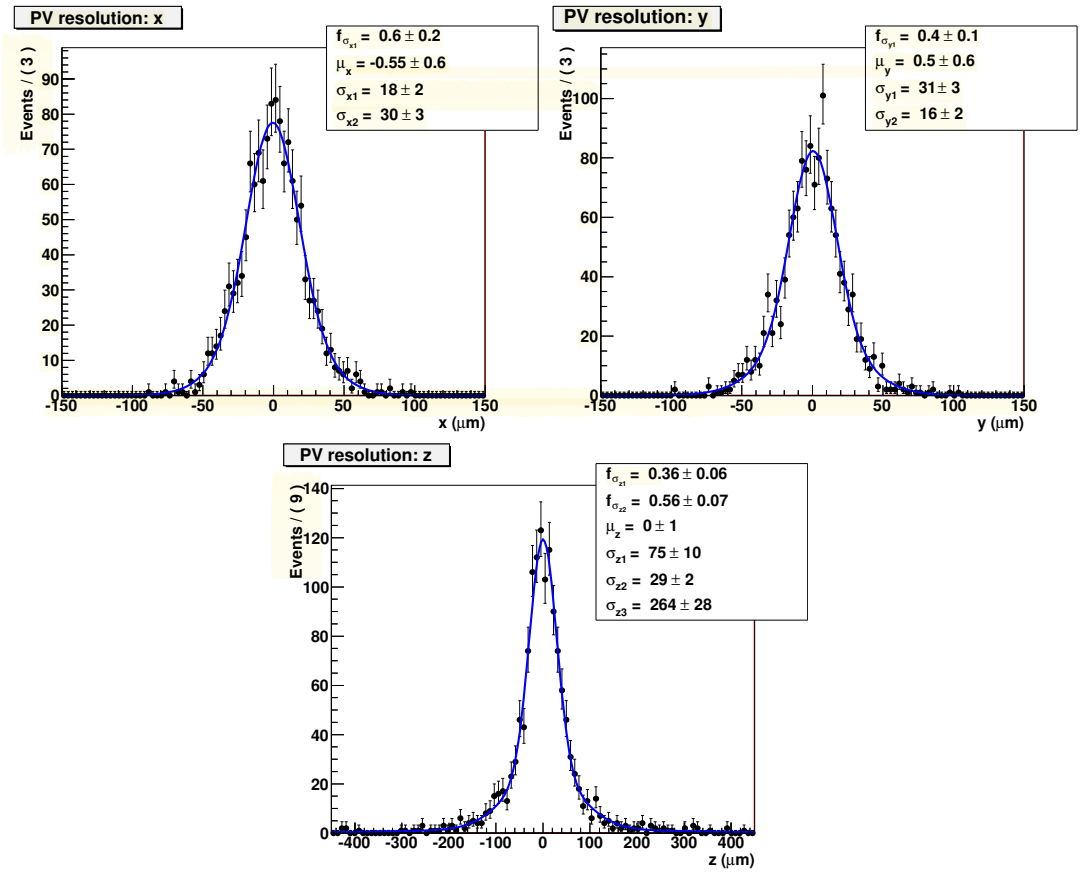

Figure 4.3: Distance from the reconstructed PV to the true PV in the x, y and z coordinates obtained from $\Lambda_b^0 \to J/\psi\,\Lambda^0$ Monte-Carlo simulation (see Appendix A). Shown are the results of the fit to a superposition of Gaussian functions for each coordinate. The Gaussian functions are centered at μ_i $(i = x, y, z)$, and have standard deviations σ_{ij} $(j = 1, 2, ...)$ weighted by $f_{\sigma_{ij}}$.

4.4 Secondary vertex reconstruction

In this thesis we are interested on forming vertices with two oppositely charged tracks [36]. The trajectories of the tracks are approximately helices, or circles in the transverse plane. For two tracks, there are two circles crossing at two points.[1] The algorithm takes the crossing point that leads to the smallest distance between tracks in the z direction. Finally, the final vertex position is calculated from on a simultaneous (two-track) χ^2 minimization of the DCA with respect to the final vertex position.

To ensure that we have good quality vertices, the χ^2 probability of every two-track vertex must be greater than 1%. Figure 4.4 shows that the J/ψ vertex is unbiased and determined with better precision in the transverse plane.[2]

4.4.1 Mass constraint

To improve the resolution of the J/ψ vertex, we vary the p_T of the muons until the invariant mass of the dimuon candidate correspond to the world-average mass of the J/ψ meson, $3,096.9$ MeV/c^2 [1]. Larger p_T errors imply larger allowed variations.

4.4.2 Λ_b^0/B^0 decay vertex reconstruction

The J/ψ has a mean lifetime of 7.1×10^{-21} s [1]. This lifetime is about a thousand times longer than typical strong decay. We know that this effect is due to the OZI Rule and energy conservation [39] (and then the electromagnetic decays become competitive). Even so, we cannot detect such a small lifetime. Therefore, we assume that the production and decay of the J/ψ occur all at the same point.

The Λ_b^0 (B^0) candidates are reconstructed by performing a kinematic vertex fit that constrains the dimuon invariant mass to the world-average J/ψ mass, and the Λ^0 (K_S^0) and two muon tracks to a common vertex. The Λ^0 (K_S^0) has been extrapolated from its decay vertex according to the reconstructed Λ^0 (K_S^0) momentum vector.

[1] Tracks decaying from one common parent may appear separated due to the finite detector resolution. In that case, circles do not cross each other. If the distance between circumferences exceeds 3 mm, the possible vertex is abandoned.

[2] Monte-Carlo studies show that the Λ^0 and K_S^0 vertices are also unbiased. A more precise measurement of these vertices have little impact on the Λ_b^0 or B^0 lifetime measurements.

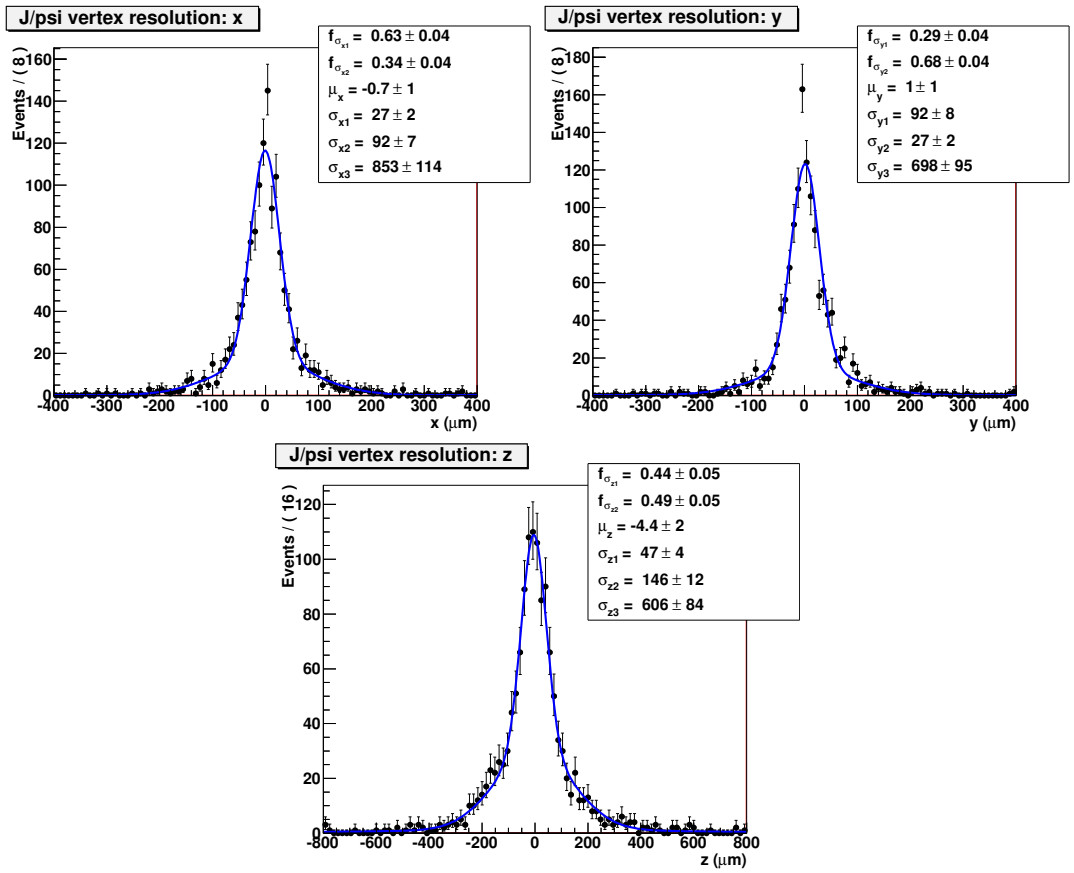

Figure 4.4: Distance from the reconstructed J/ψ vertex to the true J/ψ decay vertex in the x, y and z coordinates obtained from $\Lambda_b^0 \to J/\psi\,\Lambda^0$ Monte-Carlo simulation (see Appendix A). Shown are the results of the fit to a superposition of Gaussian functions for each coordinate. The Gaussian functions are centered at μ_i $(i = x, y, z)$, and have standard deviations σ_{ij} $(j = 1, 2, ...)$ weighted by $f_{\sigma_{ij}}$.

Figure 4.5 shows that the Λ_b^0 decay vertex is unbiased. Moreover, the three-track Λ_b^0 decay vertex resolution is about 20% better than the two-track J/ψ vertex. The corrected muon momenta also improves the Λ_b^0 (B^0) mass resolution about 50% compared to the unconstrained calculation.

4.5 Proper decay length measurement

There are two alternative ways to define the direction of flight of a particle, either by the direction of the vector from its production to its decay vertex ($\vec{d}$) or by its momentum ($\vec{p}$). On the transverse plane, it can be shown that the second definition leads to a resolution improvement of $\approx 75\%$ with respect to the first definition [40]. We can also define the decay length (L) of a particle by $|\vec{d}|$ or by $\vec{d}\cdot\vec{p}/|\vec{p}|$. Again, the second definition leads to a more precise and well behaved resolution (around the origin) that is further improved projected onto the transverse plane:

$$L_{xy} \equiv \frac{\vec{d}\cdot\vec{p}_T}{|\vec{p}_T|} \tag{4.2}$$

The proper decay length (PDL) of a b hadron candidate, denoted by λ, is obtained by boosting the decay length of the b-hadron candidate from the lab to the rest frame,

$$\lambda = \frac{L}{\gamma\beta} = L\frac{cM}{p} = L_{xy}\frac{cM}{p_T}. \tag{4.3}$$

where M_B is the PDG mass of the b hadron [1]. In the last expression we have multiplied the numerator and denominator by $\sin\theta$. Once again, properties measured on the transverse plane are more precise. Figure 4.6 shows that the measurement of the PDL is unbiased.

4.6 Data sample selection

In this analysis we use an integrated luminosity of 10.4 fb^{-1}, which is the full Run II DØ data sample. These data are divided in 5 periods. In between these periods the Tevatron was shutdown temporarily, and DØ used that time to fix or recover the efficiency of the various subdetectors:

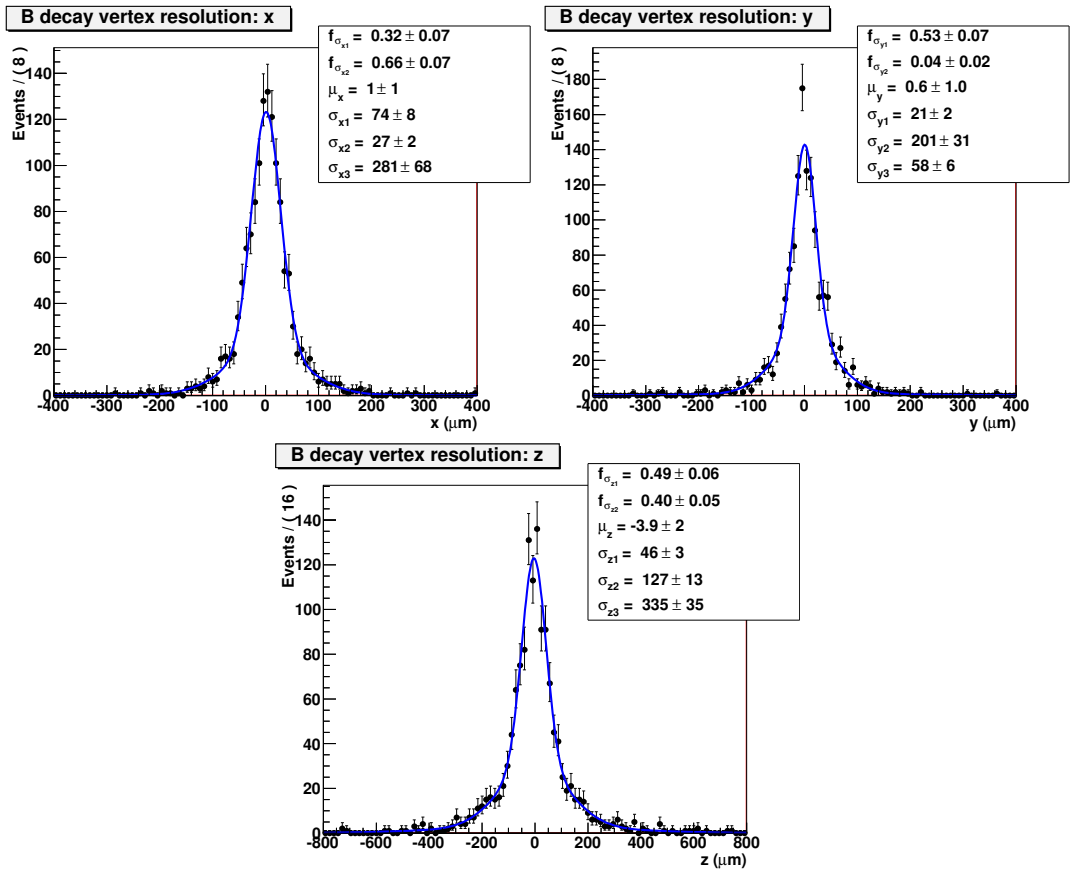

Figure 4.5: Distance from the reconstructed Λ_b^0 decay vertex to the true Λ_b^0 decay vertex in the x, y and z coordinates obtained from $\Lambda_b^0 \to J/\psi\,\Lambda^0$ Monte-Carlo simulation (see Appendix A). Shown are the results of the fit to a superposition of Gaussian functions for each coordinate. The Gaussian functions are centered at μ_i $(i = x, y, z)$, and have standard deviations σ_{ij} $(j = 1, 2, ...)$ weighted by $f_{\sigma_{ij}}$.

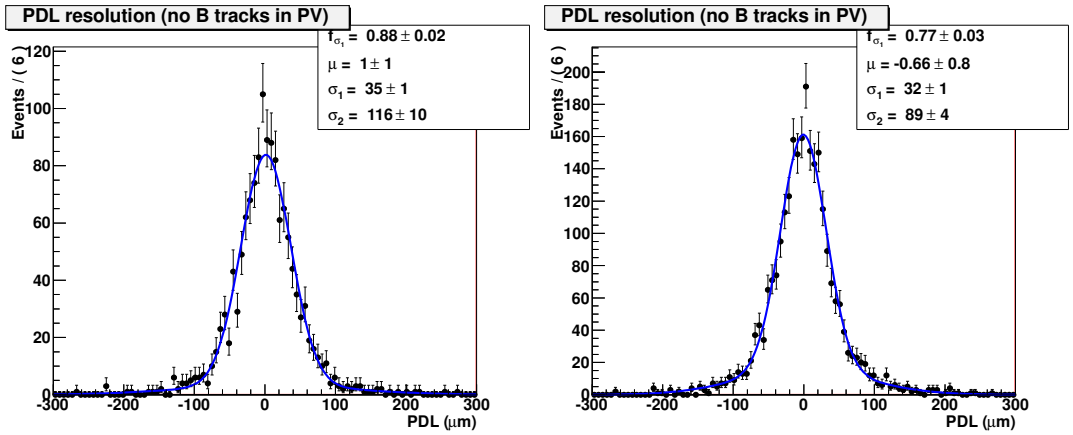

Figure 4.6: Distance from the reconstructed PDL to the true PDL obtained from (left) $\Lambda_b^0 \to J/\psi\,\Lambda^0$ and (right) $B^0 \to J/\psi\,K_S^0$ Monte-Carlo simulations (see Appendix A). Shown are the results of the fit to a superposition of Gaussian function for each decay channel. The Gaussian functions are centered at μ and have standard deviations σ_j $(j = 1, 2, ...)$ weighted by f_{σ_j}.

1. Run IIa: April 20, 2002 - February 22, 2006, recorded up to 1.3 fb^{-1}.
2. Run IIb1: June 9, 2006 - August 4, 2007, recorded up to 2.8 fb^{-1}.
3. Run IIb2: October 28, 2007 - June 13, 2009, recorded up to 6.1 fb^{-1}.
4. Run IIb3: September 14, 2009 - July 17, 2010, recorded up to 8.1 fb^{-1}.
5. Run IIb4: August 21, 2010 - September 30, 2011, recorded up to 10.4 fb^{-1}.

Data from Run IIb1 to Run IIb4 is called Run IIb. The main difference between the Run IIa and the Run IIb periods was the addition of a silicon layer (L0) just above the beam pipe.

From these data, we choose events that satisfy muon or dimuon triggers. Events fired exclusively by triggers with a minimum IP requirement for tracks are discarded from the analysis, since they can bias the lifetime measurement. We only accept events that were labeled as good or reasonable for analysis by the SMT, CFT and muon detector experts. We filter events with at least one reconstructed PV. Then, we look for events with two oppositely charged muon candidates forming a good vertex and

dimuon invariant mass consistent with the J/ψ mass. In these events we search for pairs of oppositely charged tracks forming a good vertex and invariant mass consistent with the Λ^0 or K^0_S mass. Then, we reconstruct Λ^0_b or B^0 candidates as explained in section 4.4.2. If there are multiple PVs in the event, we choose the nearest to the J/ψ vertex along the z direction. We apply further requirements to reduce the background rate without introducing a bias to the lifetime measurement.

4.6.1 J/ψ and Λ^0 selection

In order to clean the J/ψ signal we require:

- The χ^2 of the J/ψ vertex must be less than 16.
- For the muon candidates, the total number of hits between the beam pipe and the J/ψ vertex must be less than 3. After the J/ψ vertex, no more than four total forward misses are accepted.
- Each muon track must have at least two hits in the SMT and two hits in the CFT.
- At least one muon candidate in the event must have hits in the inner layer, and in at least one outer layer of the muon detector. This muon must have a p_T greater than 1 GeV/c.
- A second muon candidate must either be detected in the innermost layer of the muon system or have a calorimeter energy deposit consistent with that of a minimum-ionizing particle along the direction of hits extrapolated from the central tracking system.
- The dimuon invariant mass must be within $2.75 - 3.4$ GeV/c^2.

To clean the Λ^0 signal we require:

- The χ^2 of the Λ^0 decay vertex must be less than 25.

- For the charged tracks, the total number of hits between the beam pipe and the Λ^0 decay vertex must be less than three. After the Λ^0 decay vertex, no more than one forward miss per track is allowed.

- At least three CFT hits for each proton or pion candidate. Most of the Λ^0 decays occur after the SMT layers and, therefore, proton and pion candidates are not required to be detected in the SMT.

- The transverse distance significance (transverse distance divided by its uncertainty) between the Λ^0 decay vertex and the PV must be greater than 2 if the transverse distance uncertainty is less than 0.5 cm.

- The cosine of the angle in the transverse plane between the vector from the PV to the Λ^0 vertex and the Λ^0 momentum vector must be greater than 0.8.

- The $p_T(\Lambda^0)$ must be greater than 0.6 GeV/c.

- The square of the IP significance must exceed 5 for both tracks and 16 for at least one of them.

- The two-track invariant mass must be within $1.100 - 1.1285$ GeV/c^2. We order the tracks by p_T and consider the two possible mass assignments: (1) the leading (higher transverse momentum) track is assigned the mass of the proton, and (2) the leading track is assigned the mass of a pion.

The same Λ^0 selection criteria are applied in the selection of $K^0_S \to \pi^+\pi^-$ candidates, except that the mass window is chosen in the range $0.4455 - 0.5405$ GeV/c^2 and pion mass assignments are used.

The distance in the beam direction between the PV and the Λ^0_b/B^0 decay vertex is required to be less than 5 cm. This requirement rejects outliers with incorrectly assigned PVs. The invariant mass of Λ^0_b and B^0 candidates is selected in the range $5.15 - 6.1$ GeV/c^2 and $4.9 - 5.7$ GeV/c^2, respectively.

4.6.1.1 Standard vs. extended reconstructions

At this point it should be emphasized the advantage of using the extended reconstruction algorithm. A comparative picture is shown in Fig. 4.7. The Λ^0 yield increased about $\times 3$ in Run IIa and about $\times 20$ in Run IIb.

Unfortunately, most of the Λ^0 candidates gained by the extended reconstruction lie at very low momentum, where the Λ_b^0 signal is highly contaminated, as shown in Fig. 4.8. The p_T distribution of Λ^0 candidates coming from $\Lambda_b^0 \to J/\psi\,\Lambda^0$ decays peak at ~ 1.8 GeV/c, in contrast to direct Λ^0's (from the PV) that are expected to lie at low momentum. This property, on the other hand, is advantageous for background and signal separation.

4.6.1.2 Mass assumptions

Except for muons, the DØ detector lacks of dedicated detectors to distinguish between different types of charged particles. Therefore, it is not possible to distinguish between protons and pions.

First, we have to consider two possible mass assumptions: p(leading)π^-(trailing) and π^+(leading)$\overline{p}$(trailing). Fortunately, the transverse momentum of the proton in $\Lambda_b^0 \to J/\psi\,\Lambda^0(\to p\pi^-)$ decays is almost always greater than the transverse momentum of the pion. This kinematic property is shown Fig. 4.9 using Monte-Carlo simulation without including the detector response (see Appendix A), called Monte-Carlo at generation level. After all the requirements imposed so far, only the first assumption prevails in our data.

More problematic is the fact that a proton can be confused with a pion. If we assign the mass of a pion to the proton of a Λ^0 candidate, then the invariant mass of the track pair, $M_\Lambda(\pi^+\pi^-)$, clearly has a peak around the K_S^0 mass (Fig. 4.10 top).[1] This "cross-feed" contamination coming from $B \to J/\psi K_S^0 X$ decays (mainly from the fully reconstructed $B^0 \to J/\psi\,K_S^0$) can bias the Λ_b^0 lifetime. Therefore, we reject candidates with $M_\Lambda(\pi^+\pi^-)$ within $0.470 - 0.525$ GeV/c^2. This veto removes almost 100% of the

[1] This background was observed to be distributed almost uniformly across the Λ_b^0 mass range in previous lifetime analyses [10], and it was not removed. However, it also was the most significant source of systematic uncertainty.

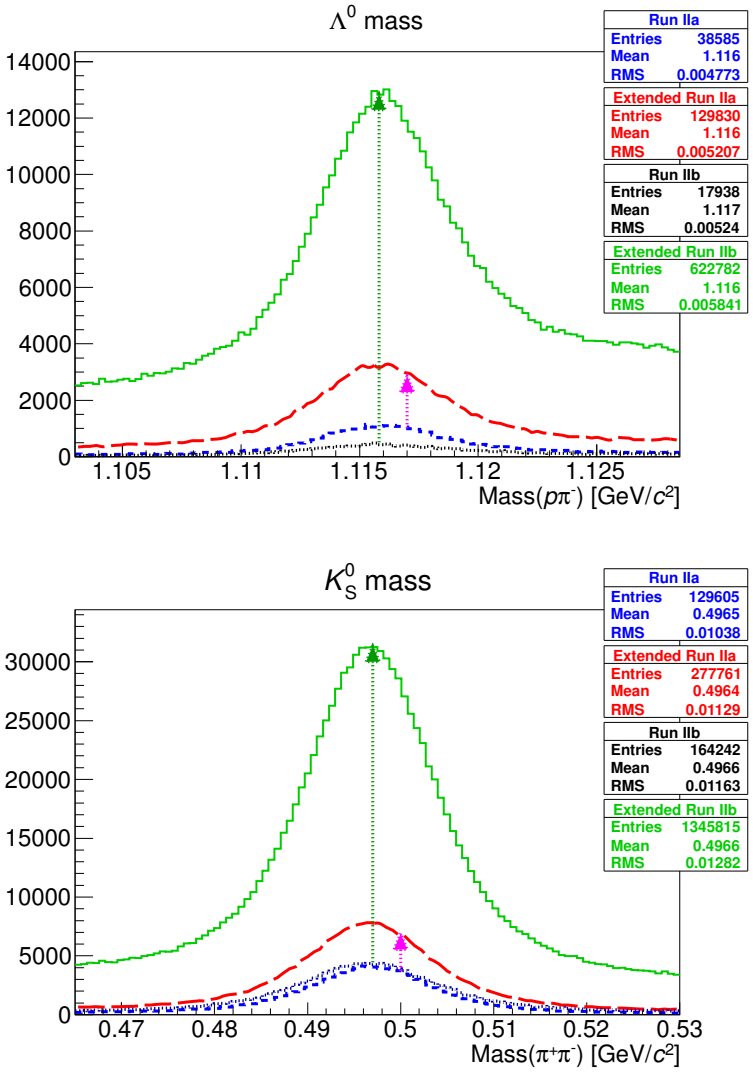

Figure 4.7: (Color online.) Standard vs. extended reconstructions. Shown are the invariant mass distributions of (top) Λ^0 and (bottom) K^0_S candidates before optimizing the Λ^0_b signal. The extended Run IIa reconstruction (red long-dashed histogram) finds ~ 3 (~ 2) times more Λ^0 (K^0_S) candidates than the standard Run IIa reconstruction (blue dashed histogram). Similarly, there are ~ 20 (~ 7) times more Λ^0 (K^0_S) candidates in the extended Run IIb data (green solid histogram) than in the standard counterpart (black dotted histogram).

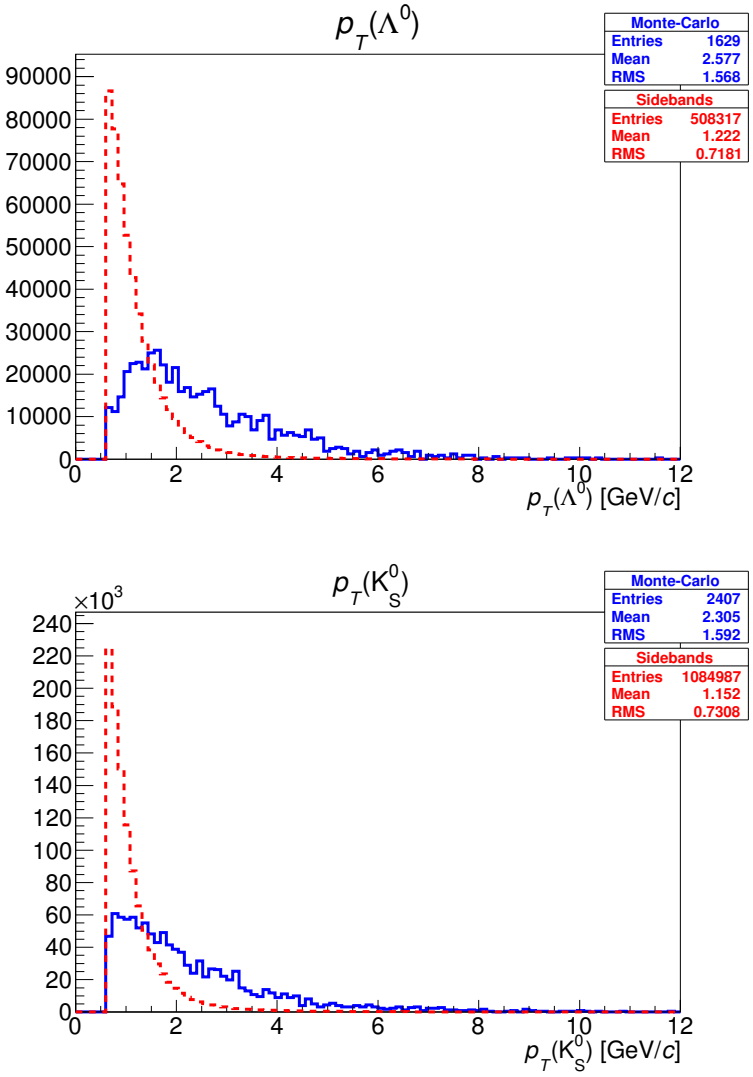

Figure 4.8: Transverse momentum distributions of (top) Λ^0 and (bottom) K^0_S candidates obtained from Monte-Carlo simulation (signal, solid histogram) and mass sidebands (background, dashed histogram).

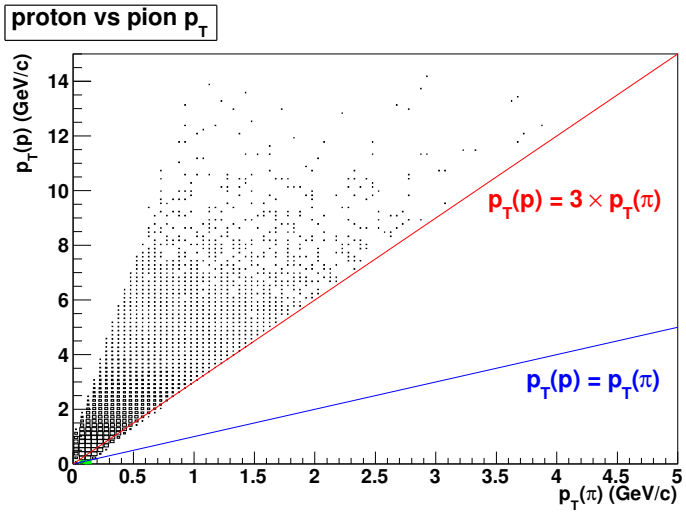

Figure 4.9: Transverse momentum of protons vs. pions in $\Lambda_b^0 \to J/\psi\,\Lambda^0(\to p\pi^-)$ decays obtained from Monte-Carlo simulation at generation level.

cross-feed and about 23% of the Λ_b^0 signal. Similarly, for K_S^0 candidates we assume that one of the tracks is a proton and then we reject all candidates with $M_{K_S^0}(p\pi^-)$ within $1.105 - 1.127$ GeV/c^2 (Fig. 4.10 bottom). This requirement removes almost $\sim 100\%$ of the cross-feed and 6% of the B^0 signal.

4.6.2 Selection optimization

To obtain a clear Λ_b^0 signal, the $\mu^+\mu^-$, $p\pi^-$ and $\pi^+\pi^-$ mass distributions are reduced to cover $\approx 99.7\%$ of the J/ψ and Λ^0 signal candidates: $2.8 < M(\mu^+\mu^-) < 3.35$ GeV/c^2 and $1.105 < M(p\pi^-) < 1.127$ GeV/c^2. The Λ_b^0 selection is optimized by maximizing the figure of merit $S/\sqrt{S+B}$, where S (B) is the number of Λ_b^0 signal (background) candidates in the data sample, estimated by fitting the Λ_b^0 mass spectrum to a superposition of a Gaussian function and an exponential decay.[1] The maximum is found by making all possible combinations of requirements in observables that are

[1]The Λ_b^0 resonance was well established in Ref. [10] using Run IIa data, where the signal optimization was based on Monte-Carlo expectations. In this analysis, we optimize the signal directly from the data. As we mentioned earlier (section 4.2.1), Monte-Carlo reprocessed with the extended algorithm was not available by the time we worked on this optimization. Later, we perform several tests to make sure that the Λ_b^0 lifetime is not biased by the selection.

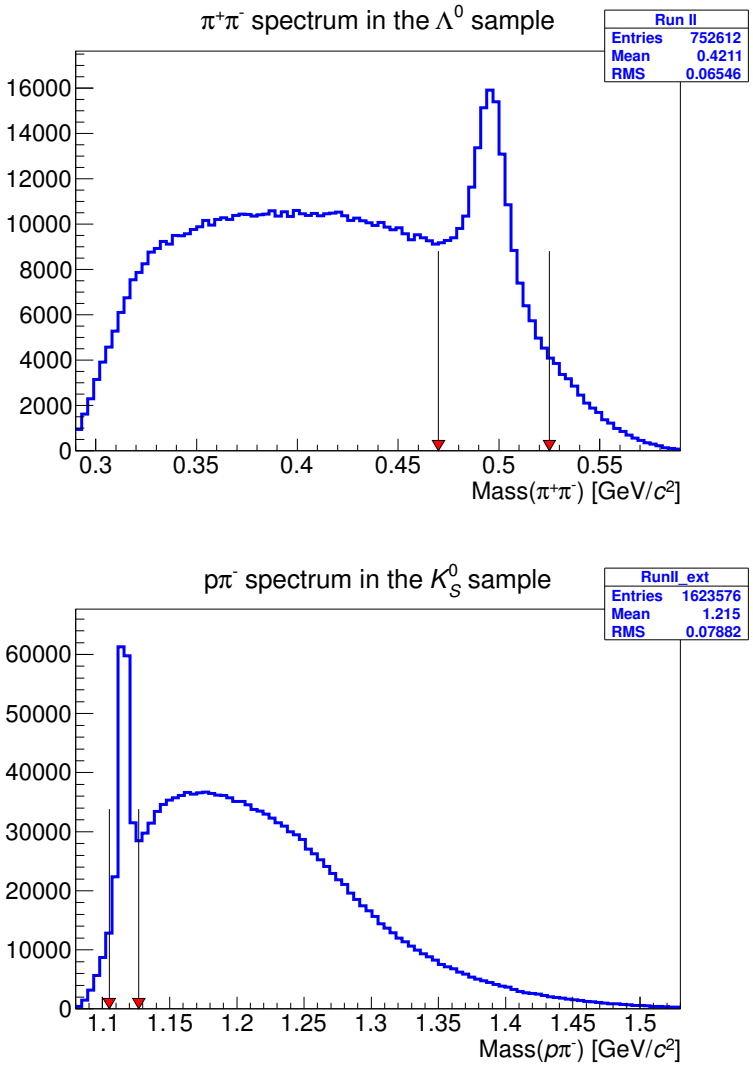

Figure 4.10: Cross-feed contamination of (top) K^0_S candidates in the Λ^0 sample, and (bottom) vice versa: the two tracks forming a Λ^0 candidate are assumed to be pions, and the tracks forming a K^0_S candidate are assigned the mass of a proton and a pion. The area between arrows is excluded.

not related to the Λ_b^0 decay time. After this process, we obtain the following final requirements:

- The $p_T(\Lambda)$ must be greater than 1.8 GeV/c.
- The p_T of protons and pions must be greater than 0.3 GeV/c.
- The Λ^0 collinearity, defined as the cosine of the angle between $\vec{p}_T(\Lambda^0)$ and the vector from the J/ψ vertex to the Λ^0 decay vertex, must be greater than 0.9999. This requirement suppresses contamination from decays of more massive baryons such as $\Sigma^0 \to \Lambda^0\gamma$ or $\Xi^0 \to \Lambda^0\pi^0$.
- The $p_T(J/\psi)$ must be greater than 4.5 GeV/c.
- The distance from the J/ψ to the Λ^0 decay vertex must be greater than 0.3 cm and its significance greater than 3.5.
- The χ^2 of the Λ_b^0 vertex must be less than 25.
- The Λ_b^0 isolation must be greater than 0.35. Isolation is defined as

$$\mathcal{I} \equiv \frac{p(\Lambda_b)}{\left[p(\Lambda_b) + \sum_{<\Delta R} p\right]}, \tag{4.4}$$

  where the sum, excluding the decay products of the Λ_b^0 candidate, is over the momentum of all particles from the PV within the larger $\Delta R(\mu^{\pm}, \Lambda_b)$ cone in pseudorapidity-azimuthal angle space, defined as $\Delta R = \sqrt{\Delta\eta^2 + \Delta\phi^2}$.

After this optimization, if more than one candidate is found in the event, which happens in less than 0.3% of the selected events, the candidate with the best Λ_b^0 decay vertex fit probability is chosen. We have verified that this selection is unbiased by varying the selection values chosen by the optimization as described in more detail later. The same selection criteria are applied to $B^0 \to J/\psi\, K_S^0$ decays (and the corresponding K_S^0 candidates).

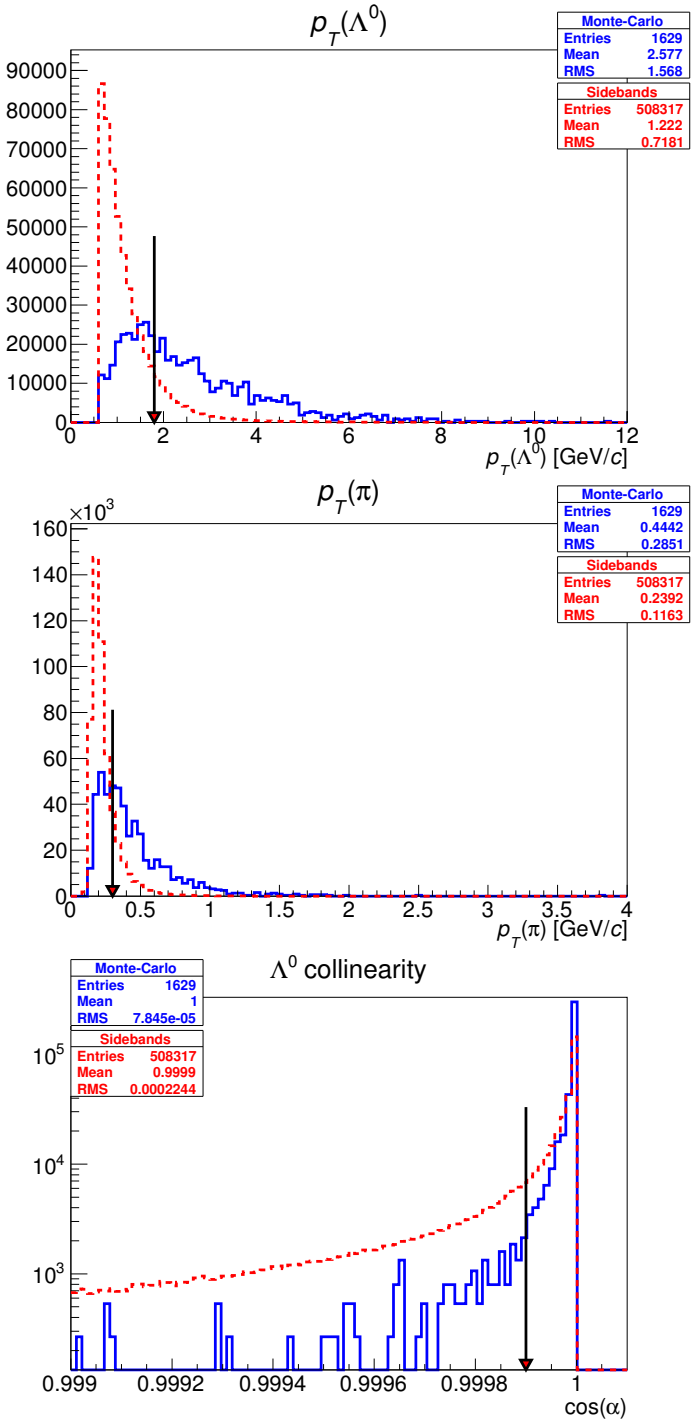

Figure 4.11: Comparison between $\Lambda_b^0 \to J/\psi\,\Lambda^0$ Monte-Carlo (solid histogram) and Λ_b^0 sidebands (dashed histogram) for the most relevant variables used to optimize the Λ_b^0 signal. The arrows indicate the requirement chosen by optimization procedure.

In Fig. 4.11 we compare $\Lambda_b^0 \to J/\psi\,\Lambda^0$ Monte-Carlo (see Appendix A) and Λ_b^0 data obtained from the sidebands regions, for variables with the highest discrimination power: $p_T(\Lambda^0)$, $p_T(\pi^-)$ (trailing track), and the Λ^0 collinearity.[1]

Finally, Fig. 4.12 shows unbinned likelihood fits to the Λ_b^0 and B^0 mass distributions, where the signal is parametrized by a Gaussian function, and the background by an exponential decay. For both decays, a single exponential decay seems to be a poor description of the background. In the following chapter we study with more detail the background composition. For now, the approximate numbers of signal events are 717 ± 70 Λ_b^0 and 5167 ± 137 B^0.

4.7 The yield problem

By direct comparison, it is determined that the extended reconstruction algorithm increases by $\sim 40\%$ the Λ_b^0 yield with respect to the standard version in the full data sample. Even after this gain, we find nearly a 50% deficit of signal events with respect to the previous DØ measurement [10]. After various studies in Monte-Carlo simulations and data subsamples according to trigger epochs, we can attribute the deficit to the following issues:

- The most recent DØ data was collected at higher instantaneous luminosities, which imposed tighter, and less efficient, trigger requirements.

- Higher instantaneous luminosities resulted in a reduction of the reconstruction efficiency caused by the presence of multiple interactions in a single bunch crossing.

- The effects mentioned above have been observed in other decays of b hadrons containing a J/ψ in the final state, such as $B^+ \to J/\psi K^+$, $B^0 \to J/\psi K^{*0}$ and $B_s \to J/\psi\phi$.

[1] The $p_T(J/\psi)$ is also an important variable. However, it depends strongly on the trigger requirements that are not simulated in the Monte-Carlo. Without the trigger simulation, an optimization based on Monte-Carlo estimates gives apparently more discrimination power to this variable than it really has.

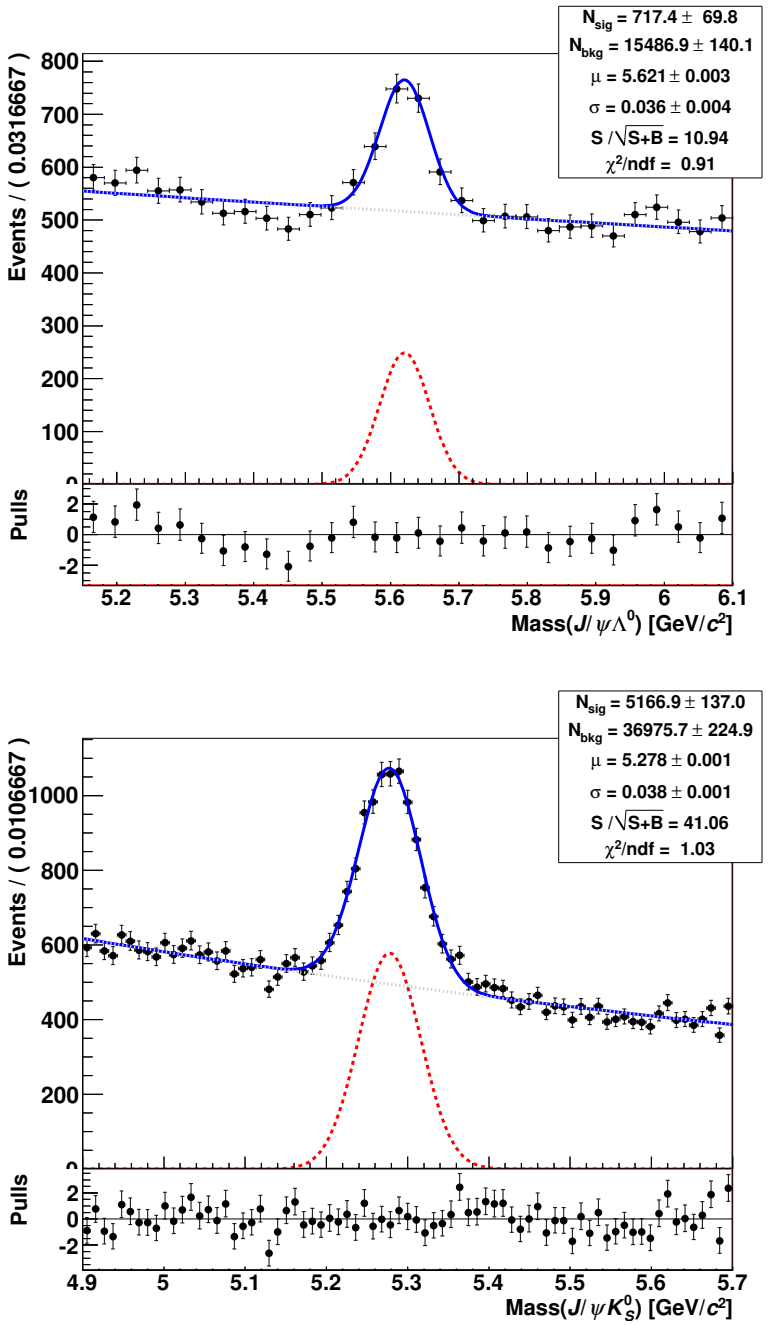

Figure 4.12: Mass distributions of (top) Λ_b^0 and (bottom) B^0 candidates after the Λ_b^0 signal optimization with fit results superimposed. The background component is parametrized by an exponential decay (dotted curve) and the signal component by a Gaussian function (dashed curve). Residuals normalized by the corresponding uncertainty in each bin (pulls) are given in the bottom panel.

- The SMT Layer-0 was added in 2006 and the reconstruction code was updated to take it into account. However, the track requirements mentioned in section 4.2 were not updated, for instance, to allow more backward misses in the SMT that are expected for long lived particles such as Λ^0 and K_S^0. Preliminaries studies showed that after some fine-tunning on these requirements, the reconstruction recovers about $5 - 10\%$ of the missing events. These studies were abandoned after proved success of the extended reconstruction.

- The removal of ambiguous Λ^0 and K_S^0 candidates (cross-feed contamination) causes a lost of approximately 23% of the Λ_b^0 signal events.

Chapter 5

Lifetime measurement

In this chapter we finally measure the Λ_b^0 lifetime. To verify that our method is reliable, we follow the same steps in our sample of reconstructed $B^0 \to J/\psi\, K_S^0$ decays.

5.1 Measurement overview

We already know that signal decays are distributed in mass according to a Gaussian function, where the width of this Gaussian is a measure of the mass resolution of the DØ detector. This is confirmed by Monte-Carlo simulations. Variations of the signal (Gaussian) shape are considered as possible sources of systematic uncertainty. Everything else, that is not described by this shape, must be background and is parameterized empirically. On the other hand, in order to measure the Λ_b^0 lifetime, we need to extract the signal component from the proper decay length (PDL) distribution that includes signal and background decays. We know that signal decays should follow an exponential function. In fact, taking into account the finite resolution of the DØ detector, the exponential is distorted by a resolution function that, according to the simulation, can be adjusted in good approximation to a Gaussian function. The ignorance of the exact shape of the PDL resolution function is a source of systematic uncertainty. Moreover, some components of the background almost mimic the signal shape and, consequently, can bias the lifetime if they are not correctly parametrized. Then, it is convenient to have a better understanding of the different backgrounds in our samples. And finally, we must take advantage of the straightforward separation of the signal and background

components in the mass distribution to assign the correct fraction of signal events in the PDL distribution. To achieve this, we perform a simultaneous unbinned likelihood fit of the mass and PDL distributions.[1]

5.2 Background studies

Previous DØ analyses that measure the lifetime of b hadrons containing a J/ψ in the final state [10, 19, 41], such as $B^0 \to J/\psi K^{*0}$ and $B_s^0 \to J/\psi\phi$, assume that the background in the vicinity of the b hadron mass peak (in the mass sidebands) describes the behavior of the background below the mass peak. Then, to avoid the introduction of biases in the lifetime measurements, the mass sidebands are chosen to have, approximately, the same number of events in the left (low) and right (high) sidebands, and below the signal peak (see Fig. 4.12). This assumption is valid if the PDL distributions of events in the low and the high sidebands are similar, which is clearly contradicted by simple comparison. Figure 5.1 shows that there are not only more long-lived decays in the low sideband than in the high sideband, but also the lifetime is longer in the low sideband. The effect is stronger in B^0 decays than in Λ_b^0 decays.

In fact, the samples of Λ_b^0 and B^0 candidates have two primary background contributions: combinatorial background and partially reconstructed b hadron decays. The combinatorial background can be divided in two categories: prompt background, which accounts for $\approx$ 70% of the total background, primarily due to direct production of J/ψ mesons; and non-prompt background, mainly produced by random combinations of a J/ψ meson from a b hadron and a Λ^0 (K_S^0) candidate in the event. Contamination from partially reconstructed b hadrons comes from b baryons (B mesons) decaying to a J/ψ meson, a Λ^0 baryon (K_S^0 meson), and additional decay products that are not reconstructed.

[1] We shall see that, in fact, we need to fit simultaneously mass, PDL and the uncertainty on the PDL to avoid biasing the lifetime.

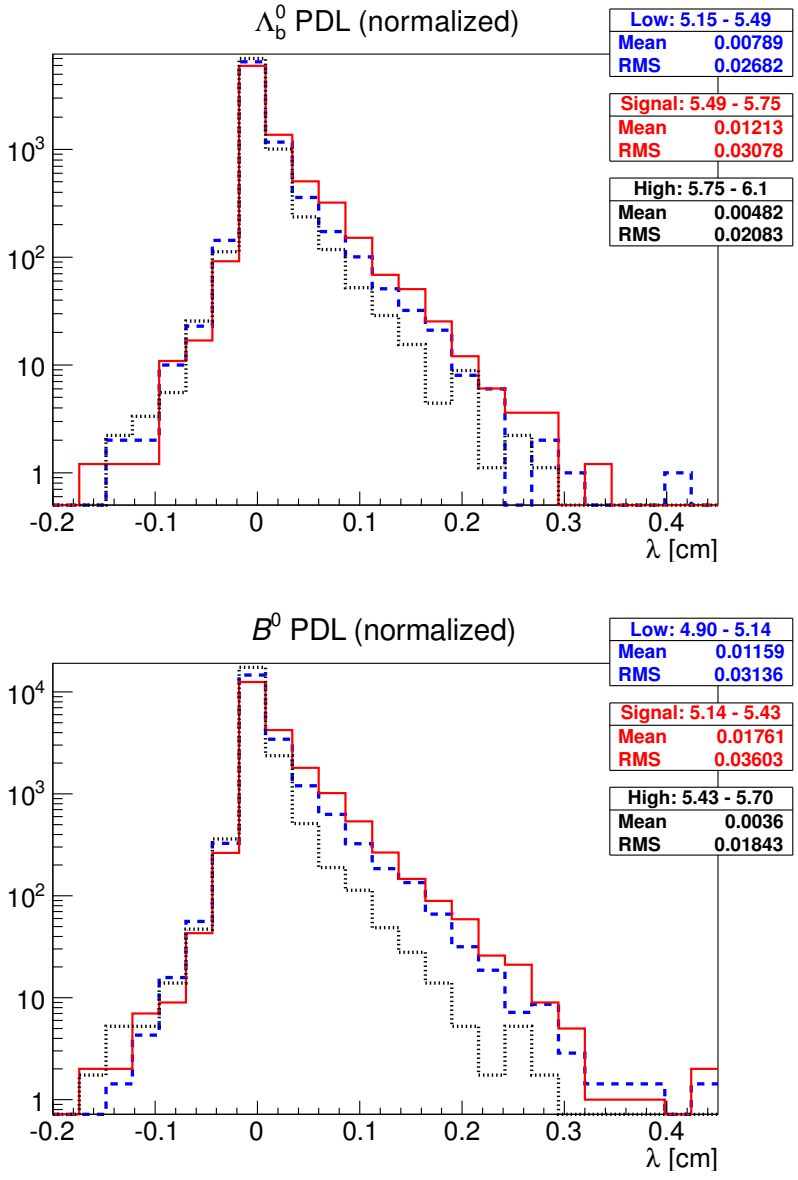

Figure 5.1: Proper decay length distributions of events in the low (dashed line) and high (dotted line) sidebands, and mass peak region (continuous line) for (top) Λ_b^0 and (bottom) B^0 candidates. Mass regions are defined in the statistics boxes.

5.2.1 Partially reconstructed b decays

Partially reconstructed b decays in our samples have a real reconstructed vertex, displaced from the PV as expected from any b hadron decay. They have an effective lifetime larger than we would expect from random $J/\psi\,\Lambda^0$ or $J/\psi\,K^0_S$ combinations, in fact, similar to the lifetime of signal decays, what makes these two components very hard to disentangle by just using the PDL distribution.

We expect lower masses for partially reconstructed b hadrons than for fully reconstructed b hadrons, since we neglect additional decay products in the calculation of the mass. This effect is supported by the data, in Fig. 5.1, where we observe that the PDL distributions of events in the low sideband and the signal region are very similar. In order to confirm this observation we generate an inclusive Monte-Carlo sample of b hadrons with PYTHIA (see Appendix A), forced to decay eventually to a J/ψ, and where at least a Λ^0 or a K^0_S is required to be produced in each event (otherwise the event is rejected). The J/ψ and the Λ^0 (or K^0_S) are not required to form a vertex. On the other hand, in data, we take advantage of the long-lived nature of partially reconstructed b decays to obtain an enriched sample of fully and partially reconstructed b hadrons, by requiring $\lambda > 100$ μm.[1]

We use the generation information of the Monte-Carlo sample and apply exactly the same selection that we used for data, except for isolation and vertex quality requirements.[2] The invariant mass of $J/\psi\,\Lambda^0$ and $J/\psi\,K^0_S$ combinations are shown in Fig. 5.2. We observe more partially reconstructed b hadrons in the B^0 sample than in the Λ^0_b sample. Therefore, we focus on the B^0 Monte-Carlo first.

In the B^0 sample, all partially reconstructed hadrons are distributed at masses below $m(B^0) - m(\pi^0) = 5.140$ GeV/c^2. These decays are of the form

$$B^0 \;\rightarrow\; J/\psi \left\{K^0, K^{*0}(892), K^{*0}_2(1430), ...\right\} X, \tag{5.1}$$

$$B^0 \;\rightarrow\; \{\chi_{c1}(1P), \chi_{c2}(1P), ...\} K^0 X, \text{ and} \tag{5.2}$$

$$B^+ \;\rightarrow\; J/\psi \{K^0, K^{*0}(892), K^{*+}(892), K^{*+}_2(1430), ...\} X, \tag{5.3}$$

[1] Other sources of backgrounds, such as Drell-Yan decays and random muon tracks, are highly suppressed at large decay times. In practice, these backgrounds cannot be distinguished from directly produced J/ψ's and, therefore, all of them contribute to the prompt background component.

[2] Detector resolution effects are not considered in these studies. However, the Monte-Carlo at generation level takes into account the propagation of particles through matter and the detector response.

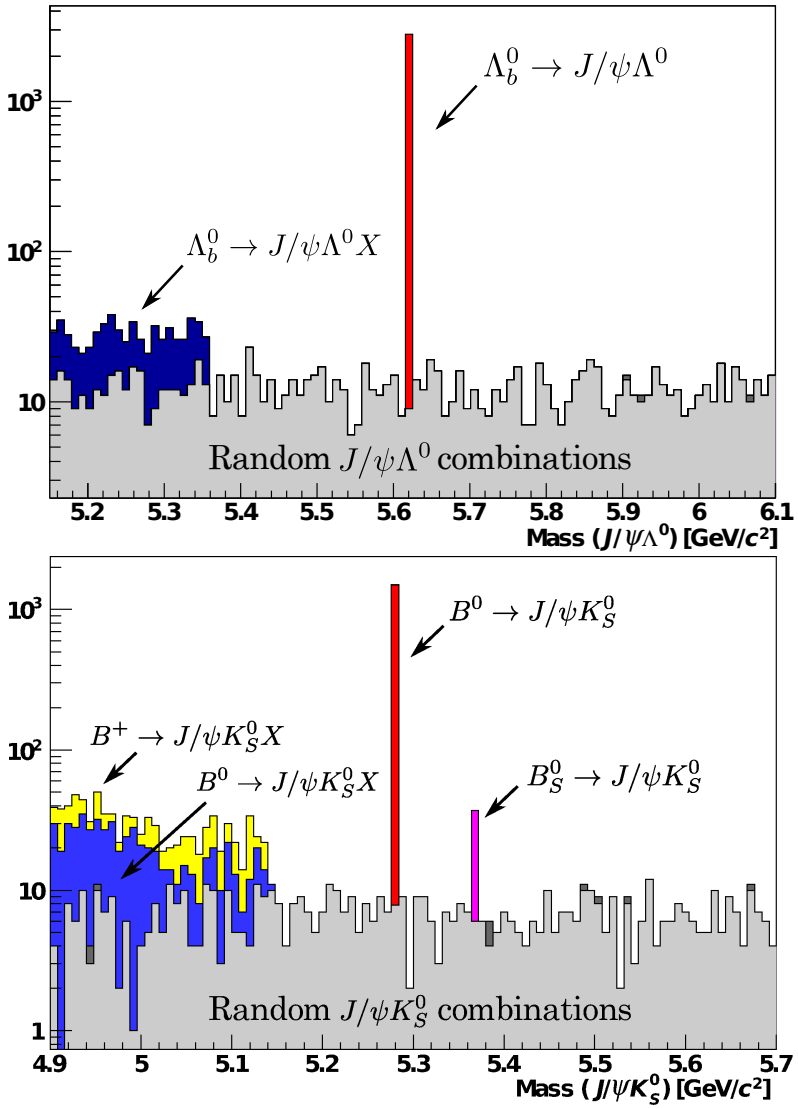

Figure 5.2: Stacked histograms of the invariant mass of (top) $J/\psi\,\Lambda^0$ and (bottom) $J/\psi\,K_S^0$ combinations in inclusive Monte-Carlo samples (see text). The mass is measured at generation level.

where X are mainly pions, $K_2^*(1430) \to \{K^0\pi, K^*(892)\pi, K^*(892)\pi\pi, ...\}$, $K^*(892) \to K^0\pi$ (charge conjugation and conservation are obviated), and $\chi_{c1,2}(1P)$ generally decays radiatively to a J/ψ. Random $J/\psi\, K_S^0$ combinations are distributed almost evenly over the full mass region (the K_S^0 originates from the PV or comes from the decay of a b quark that is different to the quark that gives rise to the J/ψ). Fully reconstructed $B_s^0 \to J/\psi K_S^0$ decays represent the sole component distributed to the right of $B^0 \to J/\psi\, K_S^0$ decays. From Ref. [42], the relative production of B_s^0 to B^0, both decaying to $J/\psi\ K_S^0$, is 0.011 ± 0.002.[1] Then, we expect about 60 $B_s \to J/\psi K_S$ events in the B^0 data sample, which for the lifetime measurement can be disregarded.

In the Λ_b^0 sample we do not expect a large contribution of partially reconstructed b hadrons due to conservation of baryon number and kinematic conservation laws. The DØ EvtGen [43], which decays b and c hadrons in the Monte-Carlo simulation (see Appendix A), only considers contamination from $\Lambda_b \to \chi_{c1}(1P)\Lambda$ decays, where the $\chi_{c1}(1P)$ decays radiatively. After rescaling $f_{\chi_{c1}\Lambda/\psi\Lambda} \equiv \Gamma(\chi_{c1}\Lambda)/\Gamma(J/\psi\Lambda)$ to the average of $\Gamma(\chi_{c1}K^0)/\Gamma(J/\psi K^0)$ and $\Gamma(\chi_{c1}K^+)/\Gamma(J/\psi K^+)$ [1], we expect ≈ 76 events distributed uniformly over 5.15 and ≈ 5.355 GeV/c^2. We also include $\Lambda_b^0 \to \psi(2s)\Lambda^0$ decays to the simulation, where the $\psi(2s)$ decays to a J/ψ and anything else ($\pi\pi, \eta, \pi^0$).[2] Only a small fraction of these decays leaks above 5.15 GeV/c^2.

We must stress that the Monte-Carlo gives only a rough estimate of the mass distribution of partially reconstructed b hadrons; the actual relative composition of the different components is not accurately known (we are probably missing some decays too). In any case, we have confirmed that they must be distributed at masses lower than the fully reconstructed b hadron.

In order to estimate the effect of the finite detector resolution on these decays, we fit the mass distributions of Λ_b^0 and B^0 candidates in data satisfying $\lambda > 100$ μm. Following [42], we parametrize partially reconstructed b hadrons in the B^0 sample with

[1] The branching ratio of many of the decays presented here are overestimated by the DØ EvtGen [43] (see Appendix A) in particular those including a $\chi_{c1,2}(1P)$. The branching ratio of the decay $B_s^0 \to J/\psi K_S^0$ is about 2.5 times greater than the measured value [42].

[2] From a preliminary study to search for $\Lambda_b^0 \to \psi(2s)\Lambda^0$, $\psi(2s) \to \mu^+\mu^-$, we observed a ratio of signal events of about 1/10 with respect to $\Lambda_b^0 \to J/\psi\Lambda^0$, $J/\psi \to \mu^+\mu^-$, which points to a non-negligible $\mathcal{B}(\Lambda_b^0 \to \psi(2s)\Lambda^0)$.

an ARGUS function,

$$f(m) = N \times m \times \sqrt{1 - \frac{m^2}{m_0^2}} \times e^{-Cm^2/m_0^2} \quad (m < m_0), \tag{5.4}$$

where N and C are free parameters in the fit representing the normalization and curvature (or decay constant), respectively. To take into account the detector resolution, the ARGUS function is convoluted with a Gaussian function that shares the same width as the signal Gaussian peak. The cut-off for partially reconstructed b hadrons is fixed to $m_0 = 5.140$ GeV/c^2. The combinatorial background is parametrized by an exponential function. Fit results are shown in Fig. 5.3 (bottom).[1] In the Λ_b^0 data sample, we fix the shape of partially reconstructed b hadrons to the Monte-Carlo and then convolute this shape with the detector resolution (a Gaussian function sharing the same standard deviation as the signal mass peak). Results of this fit are shown Fig. 5.3 (top).

Because of the fact that signal and partially reconstructed b hadron decays have similar PDL distributions that are particularly hard to disentangle in the lifetime fit, we remove partially reconstructed b hadrons by rejecting events with Λ_b^0 (B^0) invariant mass below 5.42 (5.20) GeV/c^2 from the Λ_b^0 (B^0) sample. It can be seen from Fig. 5.3 that partially reconstructed b hadrons contribute minimally to the signal mass region.

5.3 Distribution models and fitting method

The method used to measure the Λ_b^0 lifetime is similar to the previous DØ publication [10]. In this analysis, the information of the uncertainty on the PDL is taken into account by the global lifetime fit to avoid possible biases to the lifetime [44]. The same method is used to obtain the B^0 lifetime.

5.3.1 Three-dimensional likelihood

In order to extract the lifetimes, we perform separate unbinned maximum likelihood fits for Λ_b^0 and B^0 candidates. The superiority of an unbinned likelihood over a binned χ^2 fit is already well established.

[1] In data, apart from random $J/\psi\, K_S^0$ combinations, we need to consider fake K_S^0 candidates which, by definition, are combinatorial and independent of the J/ψ.

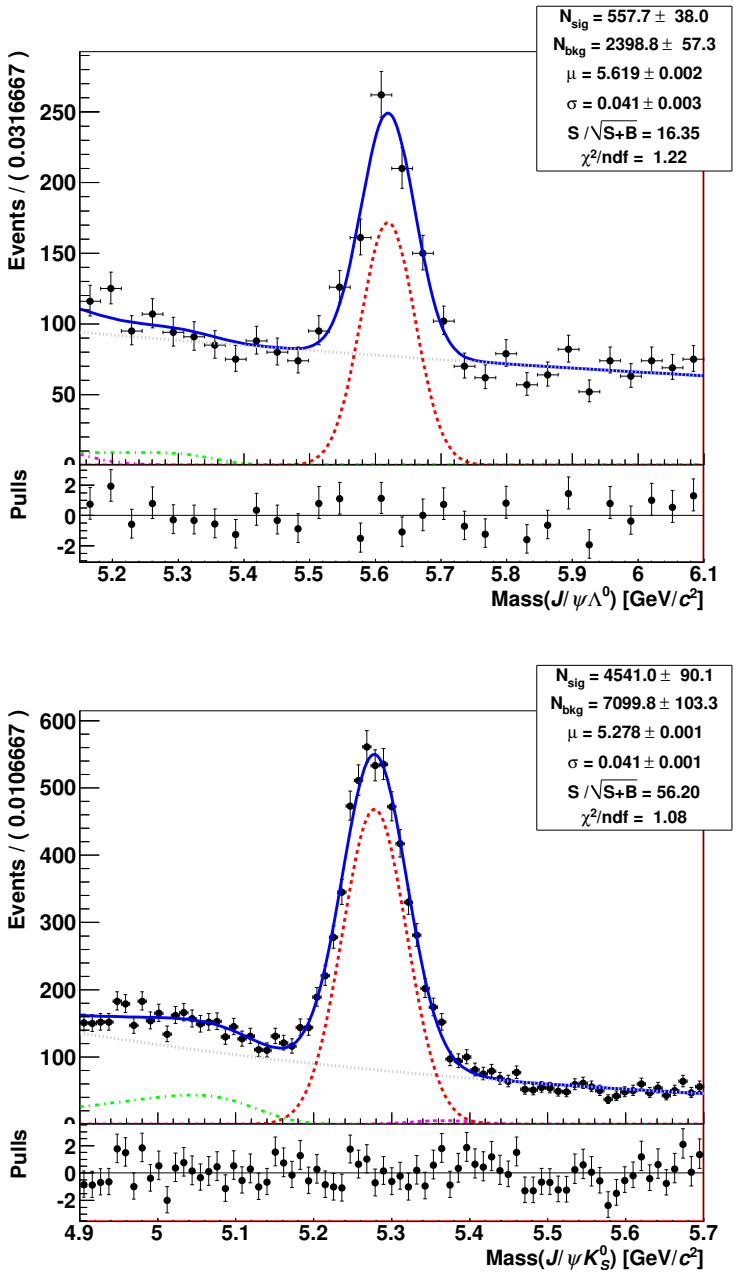

Figure 5.3: Invariant mass distributions for (top) $\Lambda_b^0 \to J/\psi\,\Lambda^0$ and (bottom) $B^0 \to J/\psi\,K_S^0$ candidates satisfying $\lambda > 100\ \mu$m. Fit results are superimposed. Shown are the signal (dashed curve), combinatorial background (dotted curve), and partially reconstructed b decays (dashed-dotted curves in the low sideband). In the B^0 sample, $B_s^0 \to J/\psi K_S^0$ decays are parametrized by a Gaussian function centered at 5.366 GeV/c^2 (dashed curve). Residuals normalized by the corresponding uncertainty in each bin (pulls) are given in the bottom panel.

The likelihood function ($\mathcal{L}$) depends on the probability of reconstructing each candidate event j in the sample with the mass m_j, the proper decay length λ_j and proper decay length uncertainty σ_j^λ:

$$\mathcal{L} = \prod_j^N \Big[f_s \mathcal{F}_s(m_j, \lambda_j, \sigma_j^\lambda) + (1 - f_s)\mathcal{F}_b(m_j, \lambda_j, \sigma_j^\lambda) \Big], \tag{5.5}$$

where f_s is the fraction of signal events and N the total number of events in the sample. $\mathcal{F}_s$ is the probability density function (PDF) describing the signal, defined as the product of the PDF for the mass peak (M_s), PDL (T_s) and PDL uncertainty (E_s),

$$\mathcal{F}_s^j = M_s(M_j) T_s(\lambda_j, \sigma_j^\lambda) E_s(\sigma_j^\lambda). \tag{5.6}$$

The background PDF, $\mathcal{F}_b$, is defined analogously, plus the separation between prompt (p subscript) and non-prompt (np subscript) contributions,

$$\mathcal{F}_b^j = \Big[f_p M_p(M_j) T_p(\lambda_j, \sigma_j^\lambda) + (1 - f_p) M_{np}(M_j) T_{np}(\lambda_j, \sigma_j^\lambda) \Big] E_b(\sigma_j^\lambda). \tag{5.7}$$

The signal PDL uncertainty PDF (E_s) is set apart from the background PDF (E_b) to avoid biasing the lifetime [44]. We know from previous lifetime analyses [10, 19, 41] that the main background contribution is prompt, the fraction (f_p) being $\geq 70\%$ of the total background.

5.3.2 Mass model

The mass distribution is modeled by

$$M(m_j) = f_s M_s(m_j) + (1 - f_s) M_b(m_j), \tag{5.8}$$

where

$$M_s(m_j) = G(m_j, \mu, \sigma) \equiv \frac{1}{\sqrt{2\pi\sigma^2}} e^{-(m_j - \mu)^2/(2\sigma^2)}, \tag{5.9}$$

$$M_b(m_j) = f_p M_p(m_j) + (1 - f_p) M_{np}(m_j). \tag{5.10}$$

The mass distribution of the prompt component of the background (M_p) is parameterized by a constant function, since we observe that the total amount of background is reduced uniformly over the entire mass range when the requirement $\lambda > 100$ μm is

applied. The non-prompt component of the background (M_{np}) is modeled by an exponential function, as observed using the data satisfying this requirement. All signal and background mass parameters are free to float in the three dimensional likelihood fit over the full mass region. Variations of the signal and background shapes are considered as possible sources of systematic uncertainty.

5.3.3 PDL model

The PDL distribution is modeled by

$$T(\lambda_j, \sigma_j^\lambda) = f_s T_s(\lambda_j, \sigma_j^\lambda) + (1 - f_s) T_b(\lambda_j, \sigma_j^\lambda), \tag{5.11}$$

where

$$T_s(\lambda_j, \sigma_j^\lambda) = \frac{1}{c\tau} e^{-\frac{x}{c\tau}} \otimes \overbrace{\sum_i f_g^{(i)} G^{(i)}(x - \lambda_j, 0, s_i \cdot \sigma_j^\lambda)}^{\mathcal{R}} \quad (x \geq 0), \tag{5.12}$$

$$T_b(\lambda_j, \sigma_j^\lambda) = f_p T_p(\lambda_j, \sigma_j) + (1 - f_p) T_{np}(\lambda_j). \tag{5.13}$$

Here τ is the lifetime that we want to extract. The signal exponential decay is convoluted with a superposition of Gaussian functions centered at zero that model the detector resolution ($\mathcal{R}$). The event-per-event uncertainty σ_j^λ is scaled by global factors s_i to take into account a possible underestimation of the uncertainty. For the nominal measurement we consider a single Gaussian function for the resolution, and therefore, we only use a global factor s:

$$\mathcal{R}(\lambda_j, s \cdot \sigma_j^\lambda) = \frac{e^{-\lambda_j^2 / 2(s\sigma_j^\lambda)^2}}{\sqrt{2\pi} s \sigma_j^\lambda}. \tag{5.14}$$

We consider two Gaussian functions (two scale factors) for the resolution as a possible source of systematic uncertainty. The prompt component of the λ distribution is parametrized by the resolution function

$$T_p(\lambda_j, s \cdot \sigma_j^\lambda) = \mathcal{R}(\lambda_j, s \cdot \sigma_j^\lambda), \tag{5.15}$$

and the non-prompt component is modeled empirically, as shown in fig. 5.4, by the superposition of two exponential decays for $\lambda < 0$ and two exponential decays for

$\lambda > 0$, as observed from events in the high-mass sideband:

$$T_{np}(\lambda_j) = \begin{cases} \frac{f_1^-}{\lambda_1^-} e^{\lambda_j/\lambda_1^-} + \frac{f_2^-}{\lambda_2^-} e^{\lambda_j/\lambda_2^-} & (\lambda_j < 0) \\ \frac{f_1^+}{\lambda_1^+} e^{-\lambda_j/\lambda_1^+} + \frac{1-f_1^- - f_2^- - f_1^+}{\lambda_2^+} e^{-\lambda_j/\lambda_2^+} & (\lambda_j > 0) \end{cases} \tag{5.16}$$

All signal and background PDL parameters are free to float in the three dimensional likelihood fit over the full mass region.

5.3.4 PDL uncertainty model

The PDL uncertainty distribution is modeled by

$$E(\sigma_j^\lambda) = f_s E_s(\sigma_j^\lambda) + (1 - f_s) E_b(\sigma_j^\lambda). \tag{5.17}$$

The signal distribution $E_s(\sigma_j^\lambda)$ is obtained from Monte-Carlo simulation and parameterized by a superposition of Gaussian functions.[1] The signal shape is fixed in the global lifetime fit. The background distribution is modeled by two exponential functions convoluted with a Gaussian function as determined from the high-mass sideband region in Fig. 5.5:

$$E_b(\sigma_j^\lambda) = \left(\frac{f_b^E}{\gamma_{1b}} e^{-x/\gamma_{1b}} + \frac{1 - f_b^E}{\gamma_{2b}} e^{-x/\gamma_{2b}} \right) \otimes G(x - \sigma_j^\lambda, \mu_b^E, \sigma_b^E) \quad (x > 0). \tag{5.18}$$

Background uncertainty parameters are free to float in the three dimensional likelihood fit over the full mass region.

5.4 Λ_b^0 and B^0 lifetime measurements

All the events, except for those corresponding to the invariant mass region contaminated by partially reconstructed b hadrons, are used in each likelihood fit to determine a total of 19 parameters: lifetime, mean and width of the signal mass, signal fraction, prompt background fraction, one non-prompt background mass parameter, 7

[1] We use the Roofit class RooKeysPdf [45] that implements a one-dimensional adaptive kernel estimation PDF which model the distribution of an arbitrary input dataset as a superposition of Gaussian kernels, one for each data point, each contributing $1/N$ to the total integral of the PDF. The width of the Gaussian is adaptively calculated from the local density of events.

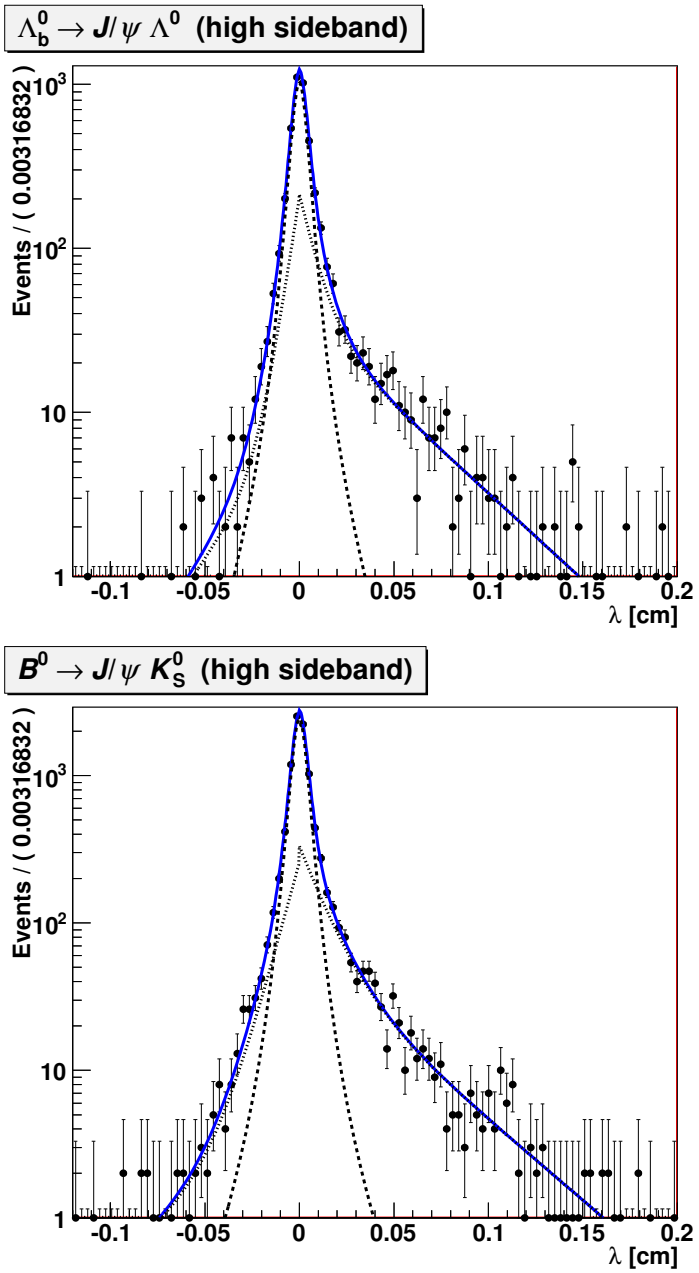

Figure 5.4: PDL distributions for (top) Λ_b^0 and (bottom) B^0 candidates in the high-mass sideband, above 5.80 and 5.45 GeV/c^2, respectively, with fit results superimposed. The dashed (dotted) curve is the projection of the prompt (no-prompt) component.

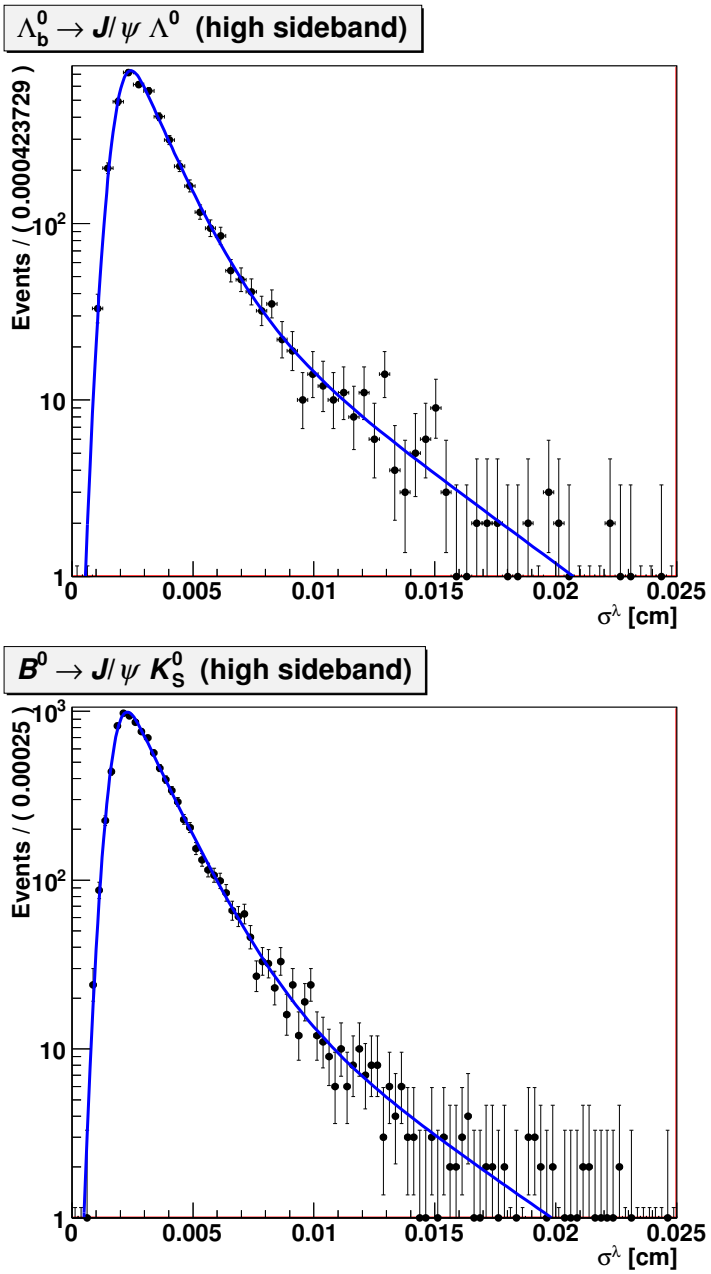

Figure 5.5: PDL uncertainty distributions for (top) Λ_b^0 and (bottom) B^0 candidates in the high-mass sideband, above 5.80 and 5.45 GeV/c^2, respectively, with fit results superimposed.

Table 5.1: Results of the maximum likelihood fit to extract the Λ_b^0 lifetime.

N	Parameter	Value	Error (−)	Error(+)
1	γ_{1b} (μm)	47.8	-3.2	3.6
2	γ_{1b} (μm)	14.1	-0.4	0.4
3	f_b^E	0.132	-0.018	0.021
4	μ_b^E (μm)	18.6	-0.1	0.2
5	σ_b^E (μm)	3.9	-0.1	0.1
6	f_2^-	0.27	-0.02	0.02
7	λ_2^- (μm)	72.2	-6.6	6.8
8	f_1^-	0.03	-0.01	0.01
9	λ_1^- (μm)	363.2	-63.7	86.3
10	f_1^+	0.39	-0.03	0.03
11	λ_1^+ (μm)	435.1	-22.4	23.8
12	λ_2^+ (μm)	79.6	-9.4	10.7
13	s	1.30	-0.02	0.02
14	f_p	0.70	-0.02	0.02
15	$c\tau$ (μm)	390.7	-22.1	22.9
16	c_{np}	-0.4	-0.1	0.1
17	μ (GeV/c^2)	5.619	-0.003	0.003
18	σ (GeV/c^2)	0.041	-0.003	0.003
19	f_s	0.070	-0.005	0.005

non-prompt background λ parameters, 5 background σ^λ parameters, and one resolution scale factor.

The maximum likelihood fits to the data yield $c\tau(\Lambda_b^0) = 390.7 \pm 22.4$ μm and $c\tau(B^0) = 452.2 \pm 7.6$ μm. The numbers of signal events, derived from f_s, are 755 ± 49 (Λ_b^0) and 5671 ± 126 (B^0). Figures 5.6 and 5.7 shows the projections on mass, PDL and PDL uncertainty obtained from the maximum likelihood fit for Λ_b^0 and B^0 candidates, respectively. Tables 5.1 and 5.2 report the values of all floating parameters.

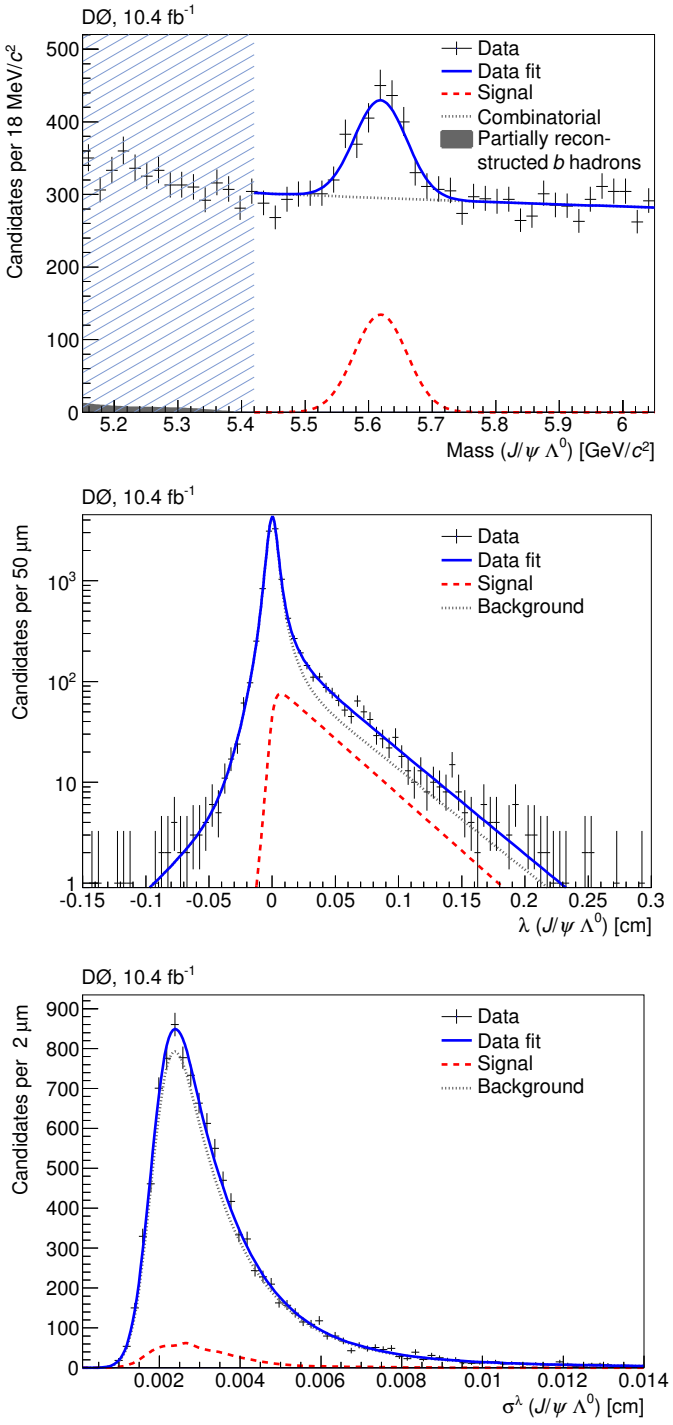

Figure 5.6: Results of the Λ_b^0 lifetime fit. Shown are the invariant mass (top), λ (middle) and σ^λ (bottom) distributions for Λ_b^0 candidates. Events in mass regions contaminated with partially reconstructed b hadrons (hatched region) are excluded from the fit.

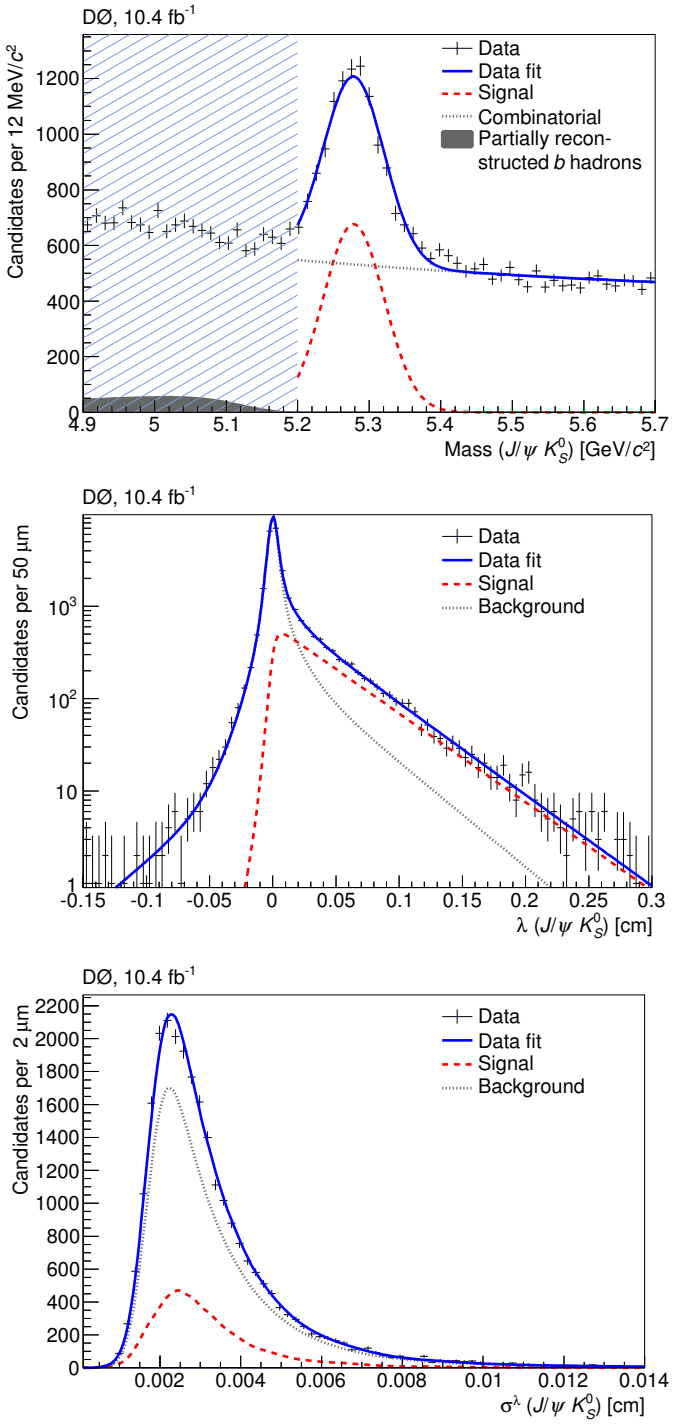

Figure 5.7: Results of the B^0 lifetime fit. Shown are the invariant mass (top), λ (middle) and σ^λ (bottom) distributions for B^0 candidates. Events in mass regions contaminated with partially reconstructed b hadrons (hatched region) are excluded from the fit.

Table 5.2: Results of the maximum likelihood fit to extract the B^0 lifetime.

N	**Parameter**	**Value**	**Error (−)**	**Error(+)**
1	γ_{1b} (μm)	46.0	-2.6	2.8
2	γ_{1b} (μm)	13.7	-0.3	0.3
3	f_b^E	0.107	-0.013	0.014
4	μ_b^E (μm)	17.4	-0.1	0.1
5	σ_b^E (μm)	3.8	-0.1	0.1
6	f_2^-	0.25	-0.01	0.01
7	λ_2^- (μm)	95.5	-9.9	8.5
8	f_1^-	0.03	-0.01	0.01
9	λ_1^- (μm)	379.2	-67.9	88.6
10	f_1^+	0.36	-0.04	0.04
11	λ_1^+ (μm)	383.2	-23.3	27.3
12	λ_2^+ (μm)	113.0	-13.1	14.2
13	s	1.32	-0.01	0.01
14	f_p	0.71	-0.01	0.01
15	$c\tau$ (μm)	452.2	-7.5	7.7
16	c_{np}	-1.3	-0.2	0.2
17	μ (GeV/c^2)	5.278	-0.001	0.001
18	σ (GeV/c^2)	0.043	-0.001	0.001
19	f_s	0.217	-0.005	0.005

5.5 Systematic uncertainties

5.5.1 Alternative fit models

We investigate possible sources of systematic uncertainties on the measured lifetimes related to the models used to describe the mass, λ, and σ^{λ} distributions.

5.5.1.1 Mass models

For the mass we consider a double Gaussian to model the signal peak instead of the nominal single Gaussian (Eq. 5.9):

$$M_s(m_j) = g_1 G(m_j, \mu, \sigma_1) + (1 - g_1) G(m_j, \mu, \sigma_2). \tag{5.19}$$

For the prompt background we use an exponential function in place of a constant function (as is done for the nominal non-prompt model). And for the non-prompt background we replace the nominal exponential decay by a second order polynomial (as was done in the previous DØ analysis [10]).

The alternative mass models are combined in a single maximum likelihood fit to take into account correlations between the effects of the different models, and the difference with respect to the result of the nominal fit is quoted as the systematic uncertainty on the mass model.

5.5.1.2 PDL models

For the PDL we study the following variations:

- The introduction of a second Gaussian function along with a second scale factor to model the resolution.
- The exponential functions in the non-prompt background replaced by exponentials convoluted with the resolution function.
- We use only one $\lambda < 0$ exponential to model the negative non-prompt background instead of two.

- We use only one long $\lambda > 0$ exponential (which is a reasonable model after removing partially reconstructed b hadrons) together with a double-Gaussian resolution (two scale factors) as a substitute for two non-prompt exponentials and one Gaussian resolution.

All PDL model changes are combined in a fit, and the difference between the results of this fit and the nominal fit is quoted as the systematic uncertainty due to PDL parametrization.

5.5.1.3 PDL uncertainty models

For the PDL uncertainty we use two different approaches:

1. The signal distribution is extracted from data by background subtraction, parameterized similarly to the nominal background σ^{λ} model, instead of the Monte-Carlo model.

2. We use the distributions obtained from signal Monte-Carlo samples generated with different Λ_b^0 (B^0) lifetimes.

The largest variation in the lifetime (with respect to the nominal measurement) between these two alternative approaches is quoted as the systematic uncertainty due to σ^{λ} parametrization.

5.5.2 B backgrounds

Residual effects due to contamination from partially reconstructed b hadrons in the samples are investigated by changing the requirement on the invariant mass of the Λ_b^0 and B^0 candidates that are included in the likelihood fits: the threshold is moved to lower (higher) invariant masses by 40 (20) MeV/c^2, where 40 MeV/c^2 is the resolution on the invariant mass of the reconstructed signal. The largest variation in the lifetime is quoted as the systematic uncertainty due to possible contamination from partially reconstructed b hadrons.

The contamination from the fully reconstructed decay $B_s^0 \to J/\psi K_S^0$ is assumed to have little impact on the final result, and is disregarded in the nominal B^0 lifetime fit.

To test this assumption the $B_s^0 \to J/\psi K_S^0$ contribution is included in the non-prompt component, constraining the relative B_s^0/B^0 production to 0.0109 ± 0.0011 [42][1] and fixing the B_s^0 lifetime to the evaluated value of the B_s^0 CP-odd lifetime component [1]. The lifetime shift is found to be negligible.

5.5.3 Alignment

The systematic uncertainty due to the alignment of the SMT detector was estimated in a previous study [10] by reconstructing the B^0 sample with the positions of the SMT sensors shifted outwards radially by the alignment uncertainty (this configuration is thought to be the worst case scenario) and then fitting for the lifetime.

5.5.4 Summary of systematic uncertainties

Table 5.3 summarizes the systematic uncertainties of the Λ_b^0 and B^0 lifetime measurements. The uncertainties due to mass, PDL and uncertainty models, possible contamination of partially reconstructed b decays, $B_s \to J/\psi K_S$ contamination and alignment are treated as uncorrelated and added in quadrature.

5.6 Consistency checks

5.6.1 Data split

5.6.1.1 Epochs

Table 5.4 presents the results of the B^0 and Λ_b^0 lifetimes after dividing the data in the two main detector epochs, Run IIa and Run IIb. The large B^0 sample allows (with no convergence problems in the fits) to subdivide the data in Run IIb1-2 and Run IIb3-4. All these results are statistically consistent.

5.6.1.2 Central/forward

The data are divided into central and forward, defined as $|\eta(\mu^{\text{lead}})| < 1$ and > 1, respectively. The fits return $c\tau(\Lambda_b^0)[central] = 399.4 \pm 33.7$ μm and $c\tau(\Lambda_b^0)[forward] =$

[1] We have corrected this fraction to take into account the rejection of B^0 candidates due to low mass limit.

Table 5.3: Summary of systematic uncertainties on the measurements of $c\tau(\Lambda_b^0)$ and $c\tau(B^0)$, and on their ratio. Uncertainties marked with * are combined in quadrature to obtain the total uncertainties.

Source	Λ_b^0 (μm)	B^0 (μm)	Ratio
Mass model	2.2	6.4	0.008
PDL model	7.8	3.7	0.024
PDL uncertainty model (lifetime in Monte-Carlo)	2.5	0.0	0.006
PDL uncertainty model (background subtracted)	1.3	8.9	0.020
PDL uncertainty model (maximum deviation)	2.5	8.9	0.020
* Total models	8.5	11.6	0.032
Partially reconstructed b hadrons ($-\sigma$)	2.7	1.1	0.008
Partially reconstructed b hadrons ($+\frac{1}{2}\sigma$)	1.3	1.3	0.005
* Partially reconstructed b hadrons (maximum deviation)	2.7	1.3	0.008
* $B_s \to J/\psi K_S$	–	0.4	0.001
* Alignment	5.4	5.4	0.002
Total	**10.4**	**12.9**	**0.033**

Table 5.4: Λ_b^0 and B^0 lifetimes in Run IIa and Run IIb. The B^0 sample is subdivided in Run IIb1-2 and Run IIb3-4.

Epoch	$c\tau(\Lambda_b^0)$ (μm)	$c\tau(B^0)$ (μm)
Run IIa	346.1 ± 46.1 (stat)	480.4 ± 19.4 (stat)
Run IIb	416.8 ± 25.2 (stat)	456.6 ± 12.6 (stat)
		451.6 ± 12.3 (stat)

387.4 ± 28.9 μm. These results are statistically consistent.

5.6.1.3 SMT hits

Λ^0 and K_S^0 are long-lived particles that, most likely, decay after the SMT (beyond 10.5 cm). Hence, there is no detection requirement on the SMT for protons and pions. From Monte-Carlo simulations, we find that the signal is reduced $\sim 50\%$ if we demand SMT hits. As a crosscheck, we repeat the lifetime fits for:

- Exactly 0 SMT hits for protons and pions:

$$\begin{aligned} c\tau(\Lambda_b^0) &= 349.4 \pm 46.8 \ \mu\text{m}, \\ c\tau(B^0) &= 449.3 \pm 14.2 \ \mu\text{m}. \end{aligned}$$

- More than 0 SMT hits for protons and pions:

$$\begin{aligned} c\tau(\Lambda_b^0) &= 423.4 \pm 24.8 \ \mu\text{m}, \\ c\tau(B^0) &= 450.8 \pm 9.5 \ \mu\text{m}. \end{aligned}$$

In both decay channels, results are statistically consistent.

5.6.2 Lifetime measurement in Monte-Carlo samples

In order to show that the reconstruction does not create any lifetime bias, we performed lifetime fits on samples of Monte-Carlo, with known generated lifetime, and passed through the full detector simulation and same reconstruction algorithm as in data. Results of this study are shown in figs. 5.8 and 5.9, displaying excellent agreement between the measured lifetimes and input values.

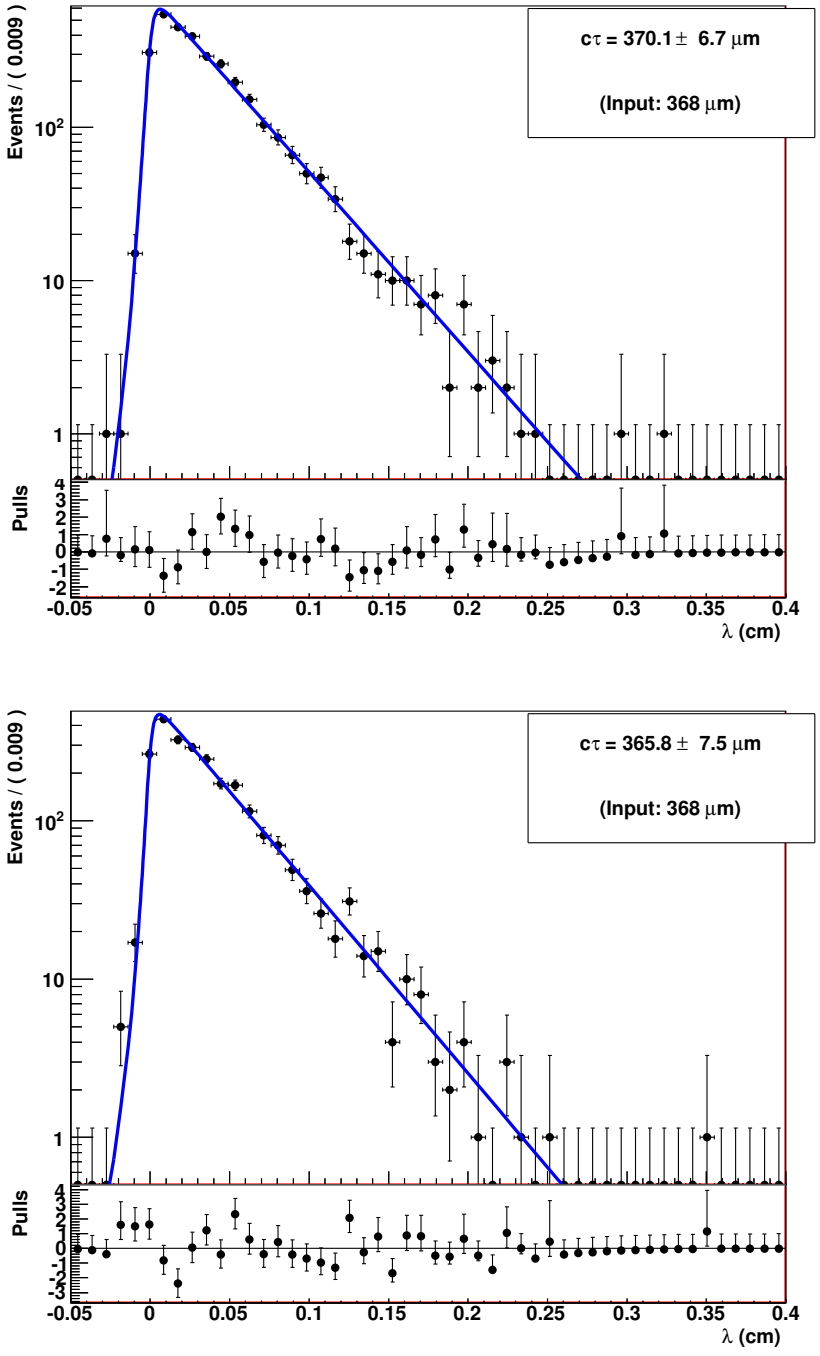

Figure 5.8: Λ_b^0 lifetime measurements in (top) Run IIa and (bottom) Run IIb Monte-Carlo.

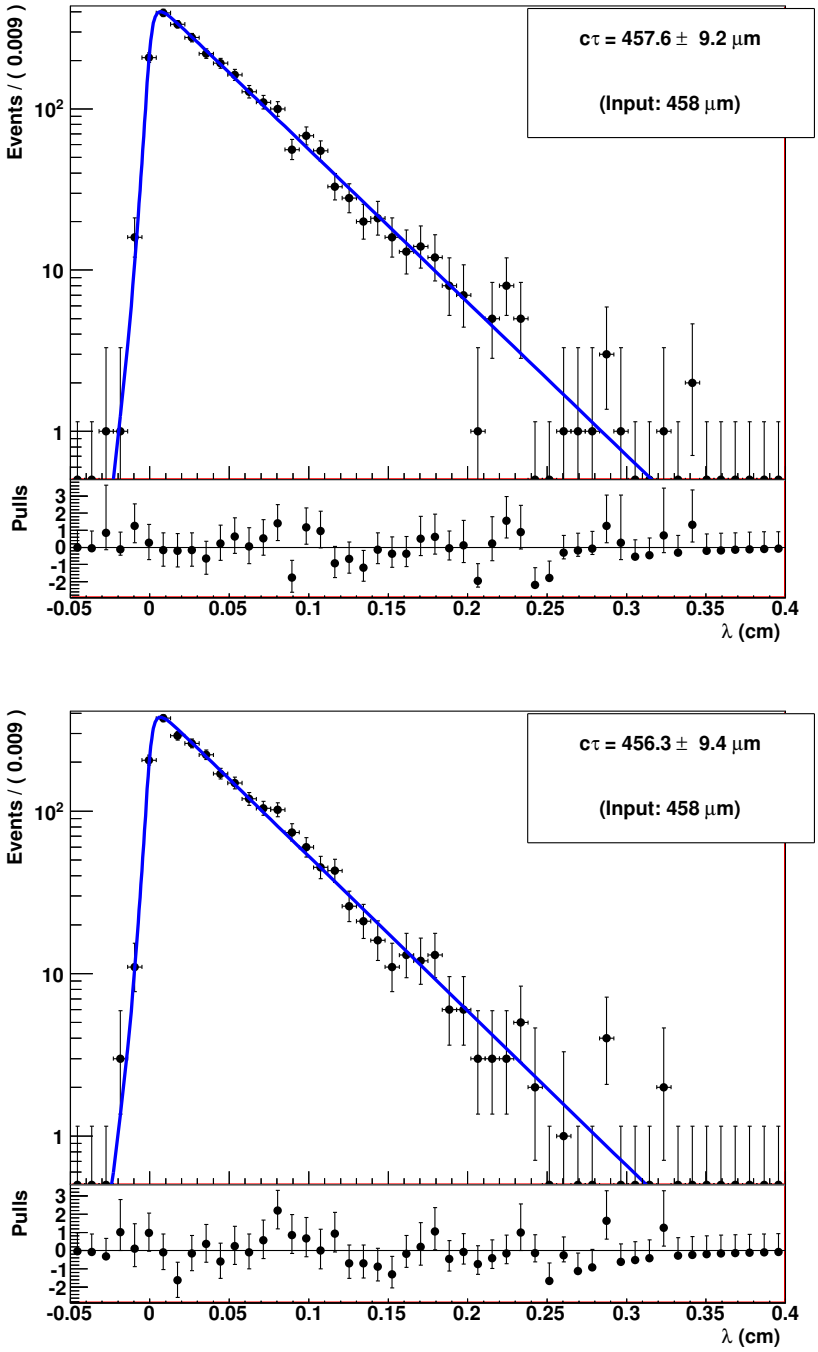

Figure 5.9: B^0 lifetime measurements in (top) Run IIa and (bottom) Run IIb Monte Carlo.

Table 5.5: Λ_b^0 and B^0 lifetimes fits removing all requirements in the optimization process one at a time.

Requirement	$c\tau(B^0)$ (μm)	$c\tau(\Lambda_b^0)$ (μm)
Nominal	452.2 ± 7.6	390.7 ± 22.4
Allow multiple candidates/event	451.7 ± 7.6	390.2 ± 22.4
No Λ^0/K_S^0 collinearity cut	448.3 ± 7.4	388.5 ± 22.2
No Λ^0/K_S^0 distance and significance cut	454.6 ± 7.6	390.5 ± 22.0
No Isolation cut	449.6 ± 7.4	394.1 ± 22.4
No $p_T(J/\psi)$ cut	452.6 ± 7.6	391.6 ± 22.3
No vertex $\chi^2(\Lambda_b^0/B^0)$ cut	455.1 ± 7.7	387.1 ± 22.7
No p_T threshold cut	448.3 ± 7.5	390.0 ± 23.3
$p_T(\Lambda^0/K_S^0) > 1.6$ GeV/c	441.5 ± 7.0	397.3 ± 23.0
$p_T(\Lambda^0/K_S^0) > 2.0$ GeV/c	453.5 ± 7.9	387.7 ± 22.9
$p_T(\Lambda^0/K_S^0) > 2.4$ GeV/c	447.0 ± 8.7	401.8 ± 24.1

5.6.3 Optimization procedure

In order to check that the optimization procedure does not give a potential bias to the selection, we verify that our results remain stable when all requirements in variables used in the optimization process are removed one at a time, when looser and tighter requirements are applied to kinematic variables, and when multiple candidates that pass all selection requirements per event are allowed. All results obtained with these variations are consistent with our measurement. Table 5.5 shows the results of these studies.

5.6.4 PDL uncertainty high-end tail

We study the effect of removing events with large PDL uncertainty. From Figs. 5.6 and 5.7 we observe that the high-end tail of PDL uncertainty plots mostly contain background events. Table 5.6 shows that the lifetime measurements stay stable after removing this tail.

Table 5.6: Λ_b^0 and B^0 lifetimes fits removing the PDL uncertainty high-end tail.

σ_{max} (μm)	$c\tau(B^0)$ (μm)	$c\tau(\Lambda_b^0)$ (μm)
100	452.0 $\pm$ 7.5	391.3 $\pm$ 22.2
150	452.9 $\pm$ 7.6	391.8 $\pm$ 22.3
200	453.0 $\pm$ 7.6	391.0 $\pm$ 22.4
300	452.2 $\pm$ 7.6	390.7 $\pm$ 22.4

5.6.5 Toy Monte-Carlo

We perform pseudo-experiments studies, generating events according to the three dimensional likelihood function, including signal and background components, and using the fit results in Tables 5.1 and 5.2. The size of each sample is the same that we have in data. We generate and fit 1000 samples for each decay channel, as shown in Fig. 5.10 and 5.11. From these studies we do not observe any bias in the lifetime measurement. We also conclude that the statistical uncertainties obtained from the fit to the data are reasonable.

5.6.6 Lifetime measured in bins of PDL

An alternative and independent method to determine the Λ_b^0 and B^0 lifetimes is to split the sample in bins of PDL. The mass distribution in each of these subsamples is fitted using a Gaussian (signal) and an exponential (background) function, as shown in Figs. 5.12 and 5.13. Table 5.7 gives the yields summary. Then, the lifetime is obtained by minimizing

$$\chi^2 = \sum_i^{N_{bins}} \frac{\left(n_i^{(m)} - n_i^{(e)}\right)^2}{(\sigma^{(m)})^2}, \tag{5.20}$$

where $n_i^{(m)} \pm \sigma^{(m)}$ and $n_i^{(e)}$ are the measured and expected number of signal events in each bin, respectively. Also,

$$n_i^{(e)} = N_s \int_i T_s(\lambda) d\lambda, \tag{5.21}$$

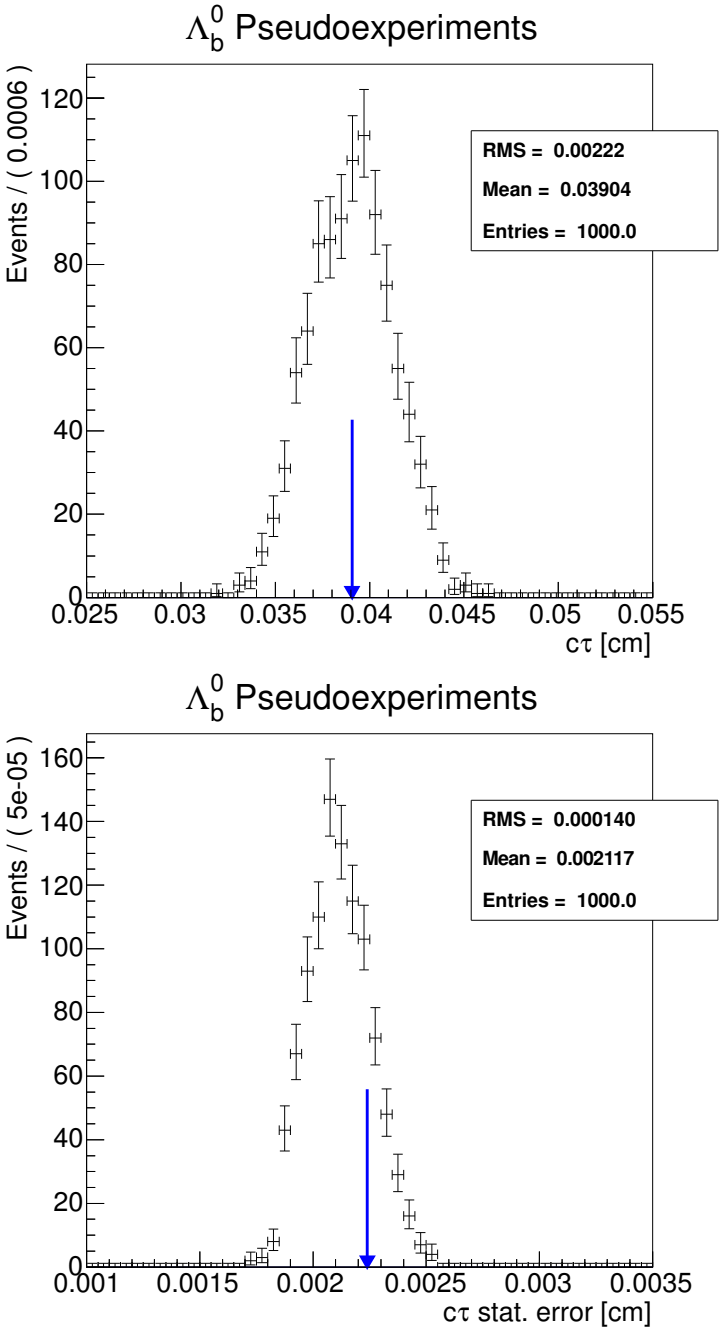

Figure 5.10: (top) Lifetime and (bottom) uncertainty of 1000 Λ_b^0 pseudo-experiments. The arrows indicate the input lifetime and the statistical uncertainty, respectively, obtained from the fit to the data.

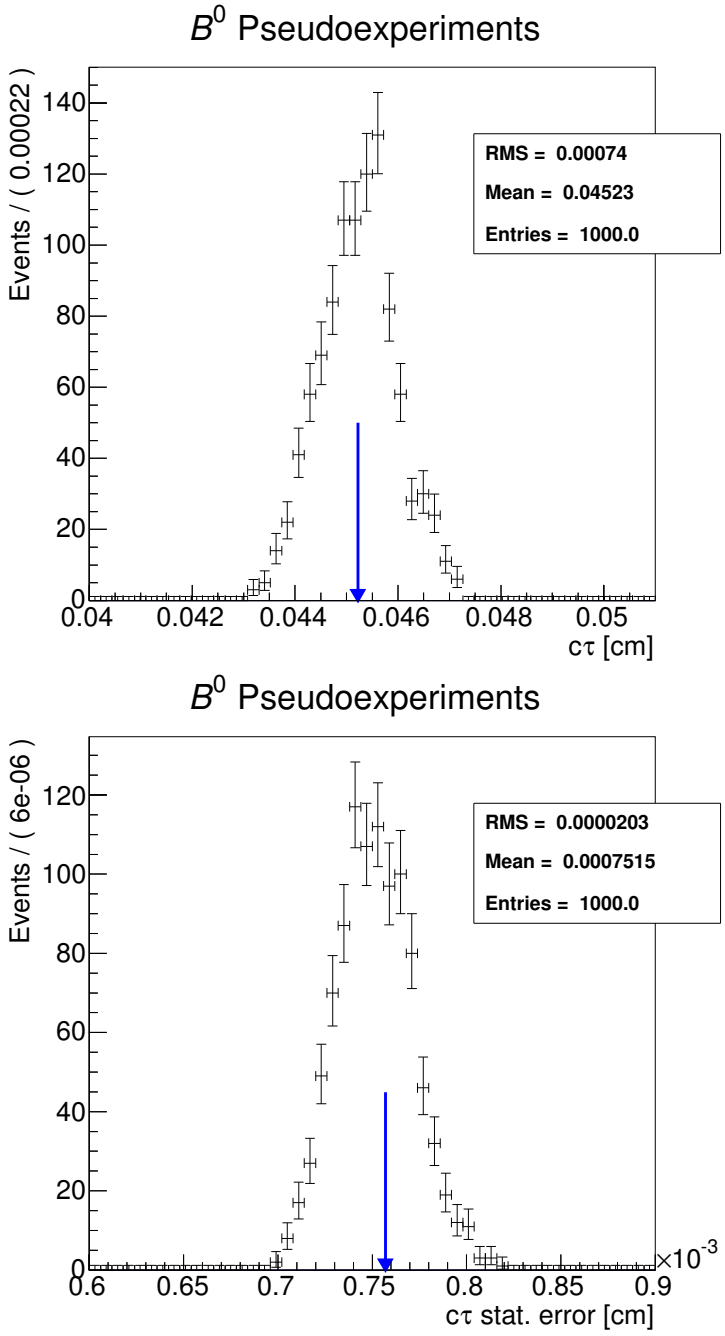

Figure 5.11: (top) Lifetime and (bottom) uncertainty of 1000 B^0 pseudo-experiments. The arrows indicate the input lifetime and the statistical uncertainty, respectively, obtained from the fit to the data.

Table 5.7: Signal yields in PDL bins.

PDL range (cm)	B^0 **signal events**	Λ_b^0 **signal events**
$[-0.04, -0.02]$	0.9 ± 1.0	–
$[-0.02, 0.00]$	109.7 ± 53.2	69.4 ± 39.9
$[0.00, 0.02]$	1665.3 ± 87.8	235.6 ± 42.1
$[0.02, 0.04]$	1235.6 ± 44.6	182.6 ± 20.3
$[0.04, 0.06]$	781.7 ± 34.3	86.9 ± 12.8
$[0.06, 0.08]$	537.8 ± 28.9	72.1 ± 11.7
$[0.08, 0.10]$	341.4 ± 22.4	41.8 ± 9.9
$[0.10, 0.12]$	192.8 ± 16.3	20.8 ± 6.3
$[0.12, 0.14]$	124.0 ± 12.9	9.9 ± 4.8
$[0.14, 0.16]$	77.9 ± 10.9	13.9 ± 4.9
$[0.16, 0.18]$	48.1 ± 8.1	6.8 ± 3.2
$[0.18, 0.20]$	41.0 ± 7.1	–
$[0.20, 0.22]$	28.1 ± 6.1	–
$[0.22, 0.24]$	16.1 ± 5.2	–
$[0.24, 0.26]$	16.1 ± 4.2	–
$[0.26, 0.28]$	8.6 ± 3.5	–
$[0.28, 0.30]$	3.5 ± 2.1	–

where the integration is made within the i-th bin range, N_s is the total number of signal events and $T_s(\lambda)$ is defined by

$$T_s(\lambda) = \frac{1}{c\tau} e^{-\frac{x}{c\tau}} \otimes \int G(x - \lambda, 0, s \cdot \sigma^\lambda) E_s(\sigma^\lambda) d\sigma^\lambda. \tag{5.22}$$

The PDL uncertainty distribution for signal events, E_s, is obtained from Monte-Carlo. N_s, $c\tau$ and s are floating parameters in the χ^2 fit.

The results of this study are $c\tau(\Lambda_b^0) = 391.4 \pm 35.8$ (stat.) μm and $c\tau(B^0) = 458.3 \pm 8.9$ (stat.) μm, and the PDL projections are shown in fig. 5.14. While this counting method is statistically inferior with respect to the maximum likelihood fit, it is also less dependent on the modeling of the different background components. Results are in good agreement between the two methods.

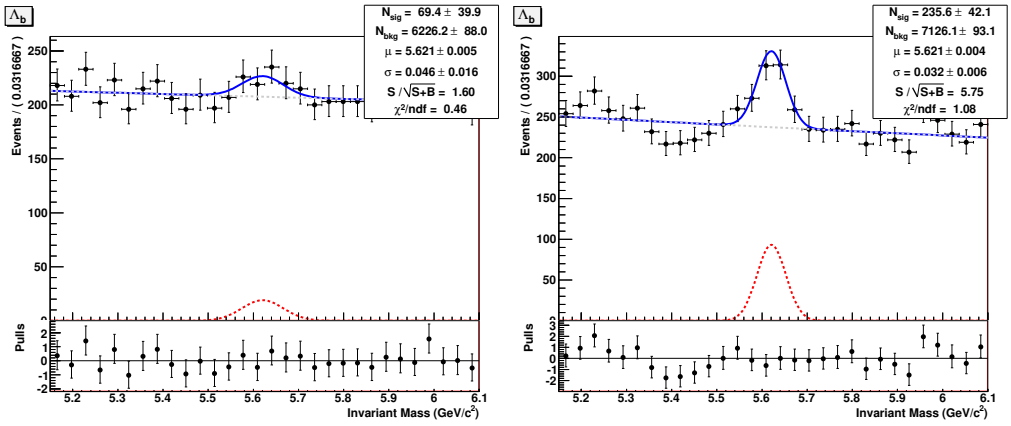

(a) $-0.02 < \lambda < 0.00$

(b) $0.00 < \lambda < 0.02$

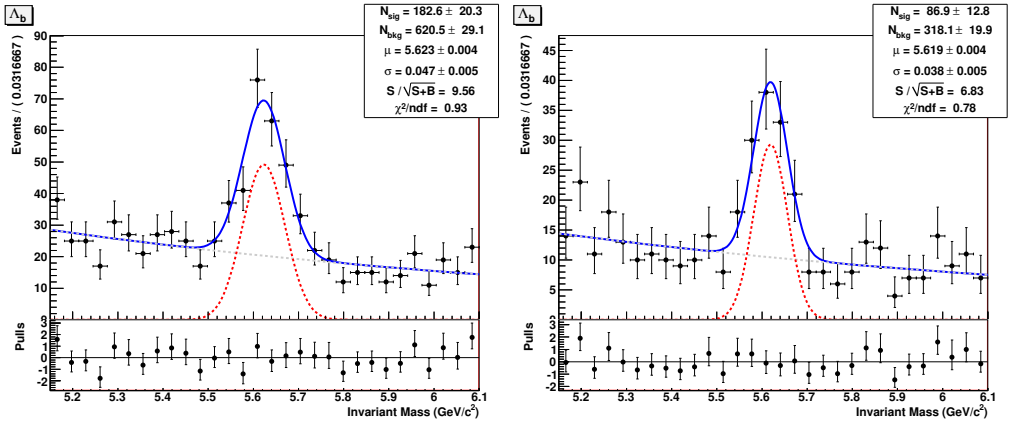

(c) $0.02 < \lambda < 0.04$

(d) $0.04 < \lambda < 0.06$

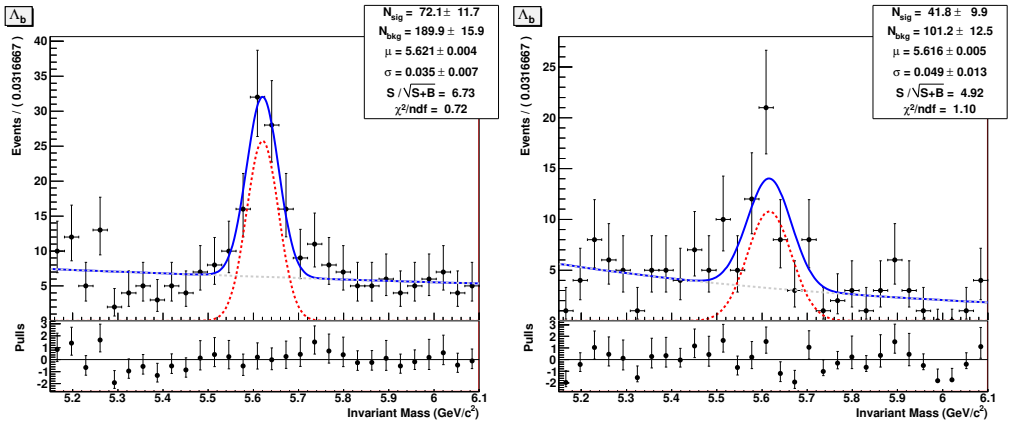

(e) $0.06 < \lambda < 0.08$

(f) $0.08 < \lambda < 0.10$

Figure 5.12: Mass fits for the first six PDL bins (most dominant for the lifetime fit) for Λ_b^0 candidates.

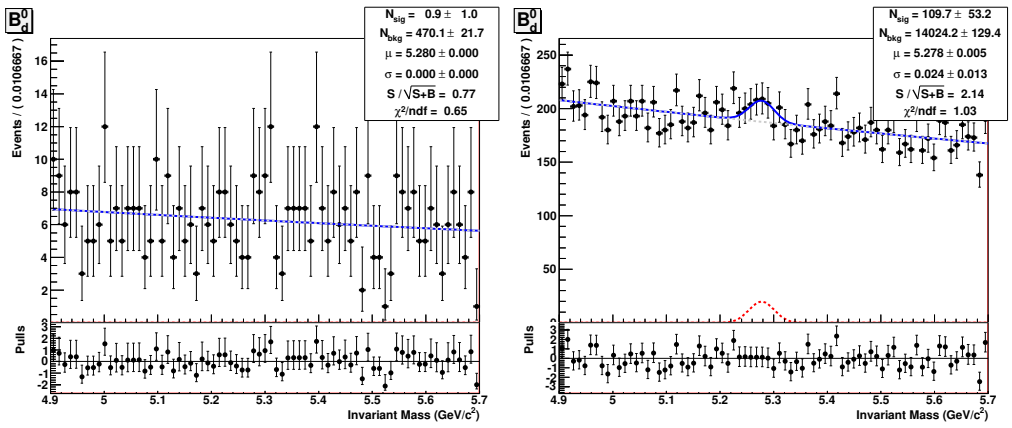

(a) $-0.04 < \lambda < -0.02$

(b) $-0.02 < \lambda < 0.00$

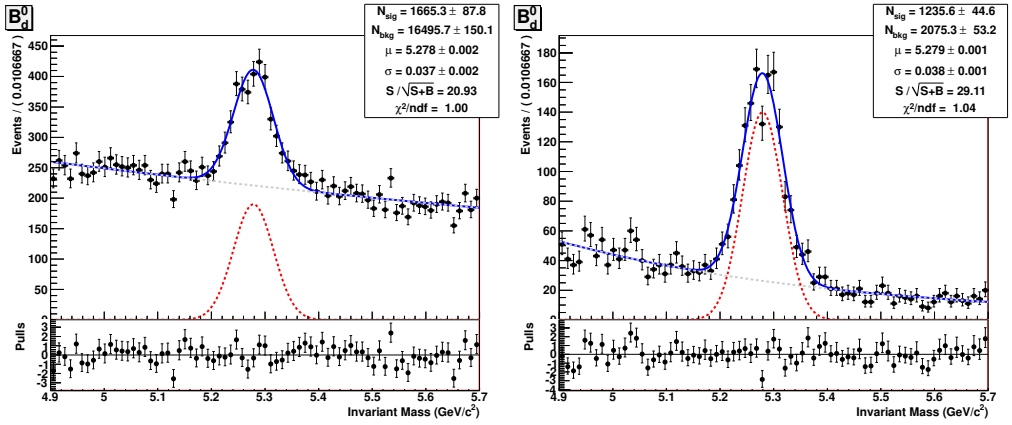

(c) $0.00 < \lambda < 0.02$

(d) $0.02 < \lambda < 0.04$

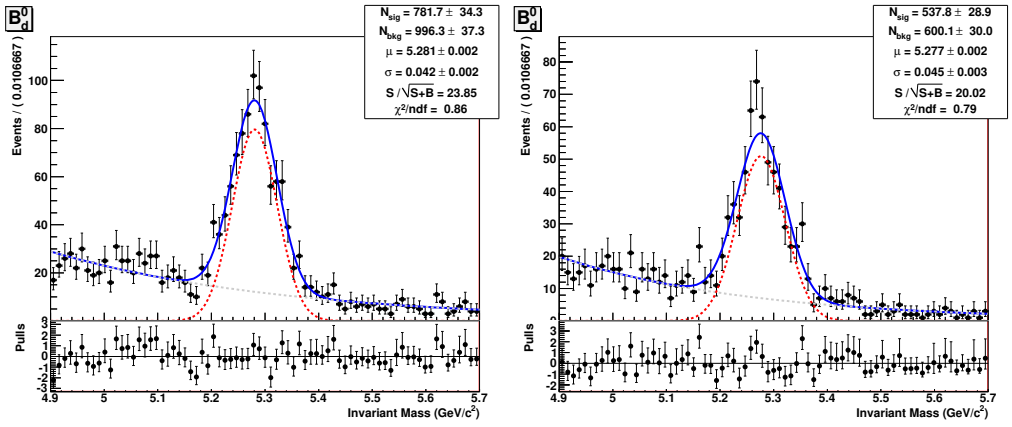

(e) $0.04 < \lambda < 0.06$

(f) $0.06 < \lambda < 0.08$

Figure 5.13: Mass fits for the first six PDL bins (most dominant for the lifetime fit) for B^0 candidates.

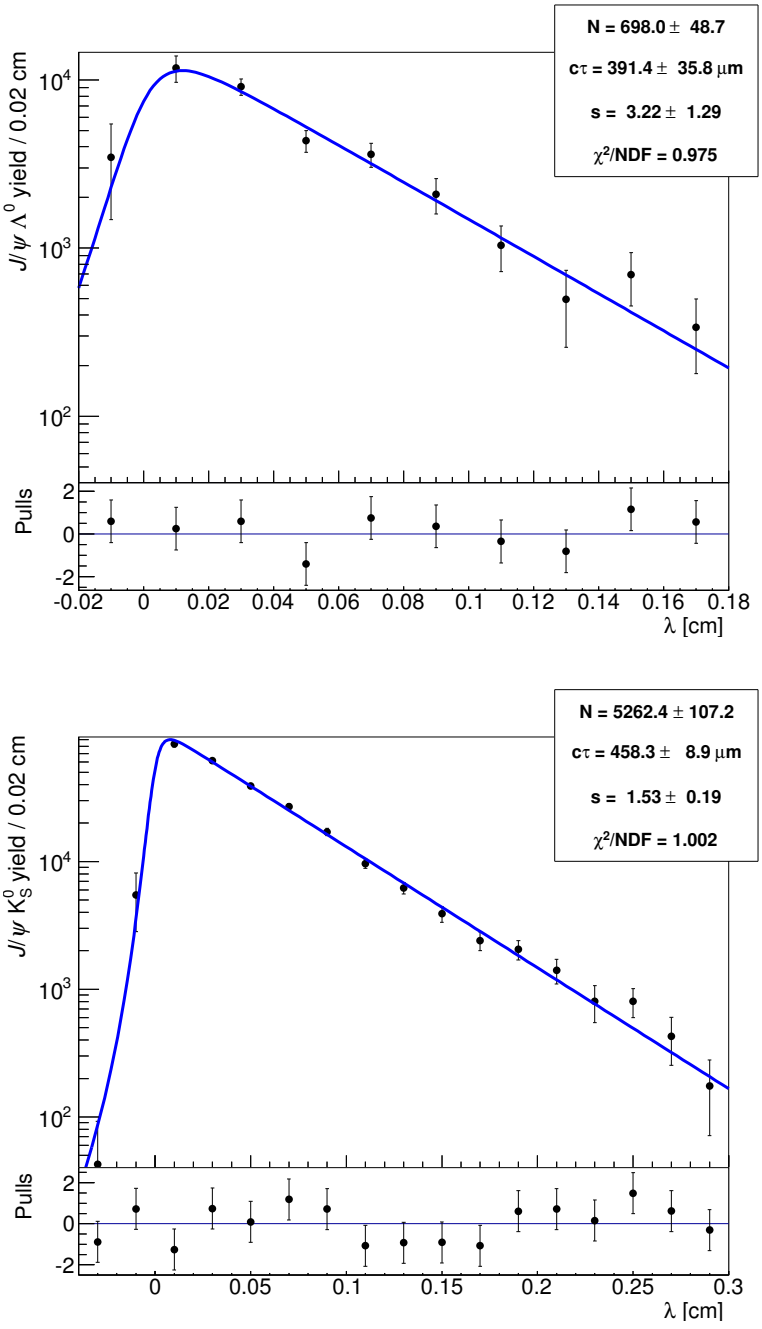

Figure 5.14: Measured yields, normalized by bin width, in bins of PDL for (top) Λ_b^0 and (bottom) B^0 candidates. Fit results are superimposed.

Chapter 6

Conclusions and perspectives

Using the full data sample collected by the DØ experiment, we measure the lifetime of the Λ_b^0 baryon in the $J/\psi\Lambda^0$ final state to be

$$c\tau(\Lambda_b^0) = 390.7 \pm 22.4 \text{ (stat.)} \pm 10.4 \text{ (syst.) } \mu\text{m}, \tag{6.1}$$

$$\tau(\Lambda_b^0) = 1.303 \pm 0.75 \text{ (stat.)} \pm 0.035 \text{ (syst.) ps}, \tag{6.2}$$

consistent with the previous DØ measurement of the Λ_b^0 lifetime, $365.1\ ^{+39.1}_{-34.7}$ (stat.) $\pm$ 12.7 (syst.) μm [10], and the world average, 427.2 ± 9.6 μm (1.425 ± 0.032 ps) [1].

The method to measure the Λ_b^0 lifetime is also used for $B^0 \to J/\psi\, K_S^0$ decays, for which we obtain

$$c\tau(B^0) = 452.2 \pm 7.6 \text{ (stat.)} \pm 12.9 \text{ (syst.) } \mu\text{m}, \tag{6.3}$$

$$\tau(B^0) = 1.508 \pm 0.025 \text{ (stat.)} \pm 0.043 \text{ (syst.) ps}, \tag{6.4}$$

in good agreement with the world average, 455.4 ± 2.1 μm (1.519 ± 0.007 ps) [1].

We find that there is a real deficit of signal events of nearly 35% in the most recent DØ data with respect to the Run IIa data used in the previous DØ measurement of the Λ_b^0 lifetime [10]. We believe this observation is important since it gives an explanation for the fail in observing significant signals of the Ξ_b^- and Ω_b^- baryons in the DØ Run IIb data, which have even lower reconstruction efficiencies due to additional tracks in the final state.

Using these measurements we calculate the ratio of lifetimes,

$$\frac{\tau(\Lambda_b^0)}{\tau(B^0)} = 0.864 \pm 0.052 \text{ (stat.)} \pm 0.033 \text{ (syst.)}, \tag{6.5}$$

where the systematic uncertainty is determined from the differences between the lifetime ratio obtained for each systematic variation and the ratio of the nominal measurements, and combining theses differences in quadrature, as shown in Table 5.3. Our result, 0.86 ± 0.06, is in good agreement with the HQE prediction of 0.88 ± 0.05 [8] and compatible with the current world-average, 1.00 ± 0.06 [1], but differs with the latest measurement of the CDF Collaboration, 1.02 ± 0.03 [7], at the 2.2 standard deviations level.

Our measurements supersede the previous DØ results of $\tau(\Lambda_b^0)$, $\tau(B^0)$ and their ratio [10]. These results [46] were published in Physical Review D on June 7, 2012 (see Appendix B).

Perspectives

There remains disagreement among the experimental values of the Λ_b^0 lifetime and further measurements are required to resolve this puzzle. However, after the definitive shutdown of the Fermilab Tevatron Collider, we have probably achieved the most precise possible measurement of the Λ_b^0 lifetime allowed by the DØ detector. Our result can be combined with a measurement of the Λ_b^0 lifetime using semileptonic decays. This analysis entails further difficulties, related to the mis-reconstructed Λ_b^0 momentum and the poor knowledge of the fractions of all possible background and signal decays, that we believe lead to larger systematic uncertainties.

The new experiments at CERN also offer the possibility to measure the Λ_b^0 lifetime in the exclusive decay $\Lambda_b^0 \to J/\psi\,\Lambda^0$. In particular, the author of this thesis is a member of the CMS Collaboration. The CMS experiment has observed 1,200 Λ_b^0 signal candidates in 1.2 fb^{-1} of pp collisions [51], and it is now possible to analyze more than 5 fb^{-1}. All tools, background studies and methods developed in our analysis can be applied directly on CMS data, with one subtle exception: unlike DØ triggers, CMS triggers introduce biases in the lifetime measurement that must be corrected. The

evolution of the trigger requirements and its implementation in the analysis represents a major challenge for any b hadron lifetime measurement.

There are other interesting properties of the Λ_b^0 baryon, and in general of b baryons, that we did not have the time study and that still remain unknown. These studies can be performed using either DØ or CMS data:

- **Measurement of the Λ_b^0 polarization [52].** A five-dimensional angular analysis is used to extract the value of the Λ_b^0 polarization which appears in the Λ_b^0 spin density matrix:
$$\boldsymbol{\rho} = \frac{1}{2}\left(\mathbf{I} + \vec{\sigma}\cdot\vec{P}\right). \tag{6.6}$$
We have already implemented the Monte-Carlo simulation of this decay in the DØ framework [2].

- **Lifetime of heavier baryons.** The extraction of the Ξ_b^- and Ω_b^- lifetimes is feasible in semileptonic decays using DØ data, and in fully and partially reconstructed decays in CMS.

- **Direct CP violation tests in Λ_b^0 decays [53].** A counting experiment is used to extract the asymmetry between $\Lambda_b^0 \to f$ and $\bar{\Lambda}_b^0 \to \bar{f}$, where f is any final state. In contrast to B mesons, CP violation in mixing is forbidden in baryons because of baryon number conservation.

- **Search for time reversal violation [54].** This is an interesting topic that complements CP violation studies and tests the validity of the CPT theorem.

Appendix A

Monte-Carlo simulation

For all Monte-Carlo (MC) simulations in this work, we use PYTHIA [47] 6.409 to simulate the $p\bar{p}$ collisions, EVTGEN [43] for modeling the decay of particles containing b and c quarks, and GEANT3 [48] to model the detector response. Multiple $p\bar{p}$ interactions are modeled by overlaying hits from random bunch crossings onto the MC. More details are given in this appendix.

PYTHIA simulates the $p\bar{p}$ collisions and generates the full event using the DØ Tune A and CTEQ6L [49] parton distributions functions. In PYTHIA we use the selector `MSEL = 5` [47] to enable (in fact, select) the generation of $b\bar{b}$ quark pairs with massive matrix elements: $q_i\bar{q}_i \to b\bar{b}$, $gg \to b\bar{b}$, $g\gamma \to b\bar{b}$, $\gamma\gamma \to b\bar{b}$ and secondary decays of gauge bosons. Heavy quarks can also be present in the parton distributions at the Q^2 scale of the hard interaction, leading to processes like $qg \to bg$ (initial state radiation can produce the other b quark), called flavour excitation, or they can be created by gluon splittings $g \to b\bar{b}$. The two last processes are disabled in `MSEL = 5`. After hadronization, b hadrons are manually set stable. The rest of the particles can suffer fragmentation (creation of new quark-antiquark pairs) and decay.

EVTGEN was used to decay the b (and c) hadrons. It implements specialized models according to the properties of the hadron, such as models for semileptonic decays, CP-violating decays and spin correlations. For the decay $\Lambda_b^0 \to J/\psi\,\Lambda^0$, we use a phase space model, and for $J/\psi \to \mu^+\mu^-$ a vector to lepton-lepton model (see PHSP and VLL in Ref. [43]). The PHOTOS [50] routine allows QED photon radiative corrections for muons. Same models are used to decay $B^0 \to J/\psi\,K_S^0$. For signal decays, the

branching ratio of $\Lambda_b^0 \to J/\psi\,\Lambda^0$, $B^0 \to J/\psi\,K_S^0$, and $J/\psi \to \mu^+\mu^-$ decays are set to 1 to increase the signal reconstruction efficiency. On the other hand, Λ^0 and K_S^0 are long lived particles that decay far away the primary interaction, so they cannot be forced to decay to a specific channel. They are decayed by GEANT that implements the geometry and material composition of the DØ detector. In a step before the detector simulation, we limit our sample to events that contain two oppositely charged muons decaying from a J/ψ, in the fiducial region $p_T(\mu^\pm) > 1$ GeV and $|\eta(\mu)| < 2.5$.

After the detector response simulation by GEANT3, we use the DØSIM program to simulate the digital signals in the detector. In this stage, random bunch crossings are overlaid onto the MC, which include low-momentum particles that enter the detector, in addition to the particles generated by PYTHIA. Finally, same as with data, DØRECO performs the event reconstruction. In a second DØRECO pass, we implement the extended AATRACK reconstruction (see section 4.2.1).

In total, we generate more than 200,000 $\Lambda_b^0 \to J/\psi(\mu^+\mu^-)\Lambda^0$ and 200,000 $B^0 \to J/\psi(\mu^+\mu^-)K_S^0$ decays per detector epoch (Run IIa and Run IIb1-3) to model the proper decay length uncertainty distribution of Λ_b^0 and B^0 decays, and for efficiency and bias studies.[1] We also generate more that 2 million events of inclusive $J/\psi + \Lambda^0$ or $J/\psi + K_S^0$ events (J/ψ and Λ^0 or K_S^0 do not necessarily form a vertex) in $b\bar{b}$ production (`MSEL = 5`) for background studies. After the extended reconstruction, we apply the same decay reconstruction algorithm and selection criteria that we follow in data.

[1] Run IIb4 samples were not available by the time we concluded the analysis.

Appendix B

Published paper

The Physical Review D [46] reporting the results shown in this thesis is presented in the following pages. The letter (e-mail) from the American Physical Society notifying the online publication of our article is shown below.

```
from: American Physical Society online_publication@aps.org via fnal.gov
to: iheredia@fnal.gov
date: Thu, Jun 7, 2012 at 2:27 PM
subject: Notification of Online Publication of Your Article in
       Phys. Rev. D [DRR1055D]

Dear Dr. La Cruz,

We are pleased to inform you that your article, "Measurement of the
$\Lambda_b^0$ lifetime in the exclusive decay $\Lambda_b^0 \rightarrow
J/\psi \Lambda^0$ in $p\bar{p}$ collisions at $\sqrt{s}=1.96$ TeV" has
been published online today, 07 June 2012, in the 1 June 2012 issue of
Physical Review D (Vol.85, No.11):

URL: http://link.aps.org/doi/10.1103/PhysRevD.85.112003
DOI: 10.1103/PhysRevD.85.112003

Thank you for choosing to publish with the American Physical Society.

Respectfully yours,
Physical Review D
```

B. PUBLISHED PAPER

PHYSICAL REVIEW D **85,** 112003 (2012)

Measurement of the Λ_b^0 lifetime in the exclusive decay $\Lambda_b^0 \to J/\psi \Lambda^0$ in $p\bar{p}$ collisions at $\sqrt{s} = 1.96$ TeV

V. M. Abazov,[32] B. Abbott,[70] B. S. Acharya,[26] M. Adams,[46] T. Adams,[44] G. D. Alexeev,[32] G. Alkhazov,[36] A. Alton,[58,*] G. Alverson,[57] M. Aoki,[45] A. Askew,[44] S. Atkins,[55] K. Augsten,[7] C. Avila,[5] F. Badaud,[10] L. Bagby,[45] B. Baldin,[45] D. V. Bandurin,[44] S. Banerjee,[26] E. Barberis,[57] P. Baringer,[53] J. Barreto,[2] J. F. Bartlett,[45] U. Bassler,[15] V. Bazterra,[46] A. Bean,[53] M. Begalli,[2] L. Bellantoni,[45] S. B. Beri,[24] G. Bernardi,[14] R. Bernhard,[19] I. Bertram,[39] M. Besançon,[15] R. Beuselinck,[40] V. A. Bezzubov,[35] P. C. Bhat,[45] S. Bhatia,[60] V. Bhatnagar,[24] G. Blazey,[47] S. Blessing,[44] K. Bloom,[61] A. Boehnlein,[45] D. Boline,[67] E. E. Boos,[34] G. Borissov,[39] T. Bose,[56] A. Brandt,[73] O. Brandt,[20] R. Brock,[59] G. Brooijmans,[65] A. Bross,[45] D. Brown,[14] J. Brown,[14] X. B. Bu,[45] M. Buehler,[45] V. Buescher,[21] V. Bunichev,[34] S. Burdin,[39,†] C. P. Buszello,[38] E. Camacho-Pérez,[29] B. C. K. Casey,[45] H. Castilla-Valdez,[29] S. Caughron,[59] S. Chakrabarti,[67] D. Chakraborty,[47] K. M. Chan,[51] A. Chandra,[75] E. Chapon,[15] G. Chen,[53] S. Chevalier-Théry,[15] D. K. Cho,[72] S. W. Cho,[28] S. Choi,[28] B. Choudhary,[25] S. Cihangir,[45] D. Claes,[61] J. Clutter,[53] M. Cooke,[45] W. E. Cooper,[45] M. Corcoran,[75] F. Couderc,[15] M.-C. Cousinou,[12] A. Croc,[15] D. Cutts,[72] A. Das,[42] G. Davies,[40] S. J. de Jong,[30,31] E. De La Cruz-Burelo,[29] F. Déliot,[15] R. Demina,[66] D. Denisov,[45] S. P. Denisov,[35] S. Desai,[45] C. Deterre,[15] K. DeVaughan,[61] H. T. Diehl,[45] M. Diesburg,[45] P. F. Ding,[41] A. Dominguez,[61] A. Dubey,[25] L. V. Dudko,[34] D. Duggan,[62] A. Duperrin,[12] S. Dutt,[24] A. Dyshkant,[47] M. Eads,[61] D. Edmunds,[59] J. Ellison,[43] V. D. Elvira,[45] Y. Enari,[14] H. Evans,[49] A. Evdokimov,[68] V. N. Evdokimov,[35] G. Facini,[57] L. Feng,[47] T. Ferbel,[66] F. Fiedler,[21] F. Filthaut,[30,31] W. Fisher,[59] H. E. Fisk,[45] M. Fortner,[47] H. Fox,[39] S. Fuess,[45] A. Garcia-Bellido,[66] J. A. García-González,[29] G. A. García-Guerra,[29,‡] V. Gavrilov,[33] P. Gay,[10] W. Geng,[12,59] D. Gerbaudo,[63] C. E. Gerber,[46] Y. Gershtein,[62] G. Ginther,[45,66] G. Golovanov,[32] A. Goussiou,[77] P. D. Grannis,[67] S. Greder,[16] H. Greenlee,[45] G. Grenier,[17] Ph. Gris,[10] J.-F. Grivaz,[13] A. Grohsjean,[15,§] S. Grünendahl,[45] M. W. Grünewald,[27] T. Guillemin,[13] G. Gutierrez,[45] P. Gutierrez,[70] A. Haas,[65,‖] S. Hagopian,[44] J. Haley,[57] L. Han,[4] K. Harder,[41] A. Harel,[66] J. M. Hauptman,[52] J. Hays,[40] T. Head,[41] T. Hebbeker,[18] D. Hedin,[47] H. Hegab,[71] A. P. Heinson,[43] U. Heintz,[72] C. Hensel,[20] I. Heredia-De La Cruz,[29] K. Herner,[58] G. Hesketh,[41,¶] M. D. Hildreth,[51] R. Hirosky,[76] T. Hoang,[44] J. D. Hobbs,[67] B. Hoeneisen,[9] M. Hohlfeld,[21] I. Howley,[73] Z. Hubacek,[7,15] V. Hynek,[7] I. Iashvili,[64] Y. Ilchenko,[74] R. Illingworth,[45] A. S. Ito,[45] S. Jabeen,[72] M. Jaffré,[13] A. Jayasinghe,[70] R. Jesik,[40] K. Johns,[42] E. Johnson,[59] M. Johnson,[45] A. Jonckheere,[45] P. Jonsson,[40] J. Joshi,[43] A. W. Jung,[45] A. Juste,[37] K. Kaadze,[54] E. Kajfasz,[12] D. Karmanov,[34] P. A. Kasper,[45] I. Katsanos,[61] R. Kehoe,[74] S. Kermiche,[12] N. Khalatyan,[45] A. Khanov,[71] A. Kharchilava,[64] Y. N. Kharzheev,[32] I. Kiselevich,[33] J. M. Kohli,[24] A. V. Kozelov,[35] J. Kraus,[60] S. Kulikov,[35] A. Kumar,[64] A. Kupco,[8] T. Kurča,[17] V. A. Kuzmin,[34] S. Lammers,[49] G. Landsberg,[72] P. Lebrun,[17] H. S. Lee,[28] S. W. Lee,[52] W. M. Lee,[45] J. Lellouch,[14] H. Li,[11] L. Li,[43] Q. Z. Li,[45] J. K. Lim,[28] D. Lincoln,[45] J. Linnemann,[59] V. V. Lipaev,[35] R. Lipton,[45] H. Liu,[74] Y. Liu,[4] A. Lobodenko,[36] M. Lokajicek,[8] R. Lopes de Sa,[67] H. J. Lubatti,[77] R. Luna-Garcia,[29,**] A. L. Lyon,[45] A. K. A. Maciel,[1] R. Madar,[15] R. Magaña-Villalba,[29] S. Malik,[61] V. L. Malyshev,[32] Y. Maravin,[54] J. Martínez-Ortega,[29] R. McCarthy,[67] C. L. McGivern,[53] M. M. Meijer,[30,31] A. Melnitchouk,[60] D. Menezes,[47] P. G. Mercadante,[3] M. Merkin,[34] A. Meyer,[18] J. Meyer,[20] F. Miconi,[16] N. K. Mondal,[26] M. Mulhearn,[76] E. Nagy,[12] M. Naimuddin,[25] M. Narain,[72] R. Nayyar,[42] H. A. Neal,[58] J. P. Negret,[5] P. Neustroev,[36] T. Nunnemann,[22] G. Obrant,[36,§§] J. Orduna,[75] N. Osman,[12] J. Osta,[51] M. Padilla,[43] A. Pal,[73] N. Parashar,[50] V. Parihar,[72] S. K. Park,[28] R. Partridge,[72,‖] N. Parua,[49] A. Patwa,[68] B. Penning,[45] M. Perfilov,[34] Y. Peters,[41] K. Petridis,[41] G. Petrillo,[66] P. Pétroff,[13] M.-A. Pleier,[68] P. L. M. Podesta-Lerma,[29,††] V. M. Podstavkov,[45] A. V. Popov,[35] M. Prewitt,[75] D. Price,[49] N. Prokopenko,[35] J. Qian,[58] A. Quadt,[20] B. Quinn,[60] M. S. Rangel,[1] K. Ranjan,[25] P. N. Ratoff,[39] I. Razumov,[35] P. Renkel,[74] I. Ripp-Baudot,[16] F. Rizatdinova,[71] M. Rominsky,[45] A. Ross,[39] C. Royon,[15] P. Rubinov,[45] R. Ruchti,[51] G. Sajot,[11] P. Salcido,[47] A. Sánchez-Hernández,[29] M. P. Sanders,[22] B. Sanghi,[45] A. S. Santos,[1,‡‡] G. Savage,[45] L. Sawyer,[55] T. Scanlon,[40] R. D. Schamberger,[67] Y. Scheglov,[36] H. Schellman,[48] S. Schlobohm,[77] C. Schwanenberger,[41] R. Schwienhorst,[59] J. Sekaric,[53] H. Severini,[70] E. Shabalina,[20] V. Shary,[15] S. Shaw,[59] A. A. Shchukin,[35] R. K. Shivpuri,[25] V. Simak,[7] P. Skubic,[70] P. Slattery,[66] D. Smirnov,[51] K. J. Smith,[64] G. R. Snow,[61] J. Snow,[69] S. Snyder,[68] S. Söldner-Rembold,[41] L. Sonnenschein,[18] K. Soustruznik,[6] J. Stark,[11] D. A. Stoyanova,[35] M. Strauss,[70] L. Stutte,[45] L. Suter,[41] P. Svoisky,[70] M. Takahashi,[41] M. Titov,[15] V. V. Tokmenin,[32] Y.-T. Tsai,[66] K. Tschann-Grimm,[67] D. Tsybychev,[67] B. Tuchming,[15] C. Tully,[63] L. Uvarov,[36] S. Uvarov,[36] S. Uzunyan,[47] R. Van Kooten,[49] W. M. van Leeuwen,[30] N. Varelas,[46] E. W. Varnes,[42] I. A. Vasilyev,[35] P. Verdier,[17] A. Y. Verkheev,[32] L. S. Vertogradov,[32] M. Verzocchi,[45] M. Vesterinen,[41] D. Vilanova,[15] P. Vokac,[7] H. D. Wahl,[44] M. H. L. S. Wang,[45] J. Warchol,[51] G. Watts,[77] M. Wayne,[51] J. Weichert,[21] L. Welty-Rieger,[48] A. White,[73] D. Wicke,[23] M. R. J. Williams,[39] G. W. Wilson,[53] M. Wobisch,[55] D. R. Wood,[57] T. R. Wyatt,[41] Y. Xie,[45]

R. Yamada,[45] W.-C. Yang,[41] T. Yasuda,[45] Y. A. Yatsunenko,[32] W. Ye,[67] Z. Ye,[45] H. Yin,[45] K. Yip,[68] S. W. Youn,[45] J. Zennamo,[64] T. Zhao,[77] T. G. Zhao,[41] B. Zhou,[58] J. Zhu,[58] M. Zielinski,[66] D. Zieminska,[49] and L. Zivkovic[72]

(D0 Collaboration)

[1]*LAFEX, Centro Brasileiro de Pesquisas Físicas, Rio de Janeiro, Brazil*
[2]*Universidade do Estado do Rio de Janeiro, Rio de Janeiro, Brazil*
[3]*Universidade Federal do ABC, Santo André, Brazil*
[4]*University of Science and Technology of China, Hefei, People's Republic of China*
[5]*Universidad de los Andes, Bogotá, Colombia*
[6]*Charles University, Faculty of Mathematics and Physics, Center for Particle Physics, Prague, Czech Republic*
[7]*Czech Technical University in Prague, Prague, Czech Republic*
[8]*Center for Particle Physics, Institute of Physics, Academy of Sciences of the Czech Republic, Prague, Czech Republic*
[9]*Universidad San Francisco de Quito, Quito, Ecuador*
[10]*LPC, Université Blaise Pascal, CNRS/IN2P3, Clermont, France*
[11]*LPSC, Université Joseph Fourier Grenoble 1, CNRS/IN2P3, Institut National Polytechnique de Grenoble, Grenoble, France*
[12]*CPPM, Aix-Marseille Université, CNRS/IN2P3, Marseille, France*
[13]*LAL, Université Paris-Sud, CNRS/IN2P3, Orsay, France*
[14]*LPNHE, Universités Paris VI and VII, CNRS/IN2P3, Paris, France*
[15]*CEA, Irfu, SPP, Saclay, France*
[16]*IPHC, Université de Strasbourg, CNRS/IN2P3, Strasbourg, France*
[17]*IPNL, Université Lyon 1, CNRS/IN2P3, Villeurbanne, France and Université de Lyon, Lyon, France*
[18]*III. Physikalisches Institut A, RWTH Aachen University, Aachen, Germany*
[19]*Physikalisches Institut, Universität Freiburg, Freiburg, Germany*
[20]*II. Physikalisches Institut, Georg-August-Universität Göttingen, Göttingen, Germany*
[21]*Institut für Physik, Universität Mainz, Mainz, Germany*
[22]*Ludwig-Maximilians-Universität München, München, Germany*
[23]*Fachbereich Physik, Bergische Universität Wuppertal, Wuppertal, Germany*
[24]*Panjab University, Chandigarh, India*
[25]*Delhi University, Delhi, India*
[26]*Tata Institute of Fundamental Research, Mumbai, India*
[27]*University College Dublin, Dublin, Ireland*
[28]*Korea Detector Laboratory, Korea University, Seoul, Korea*
[29]*CINVESTAV, Mexico City, Mexico*
[30]*Nikhef, Science Park, Amsterdam, The Netherlands*
[31]*Radboud University Nijmegen, Nijmegen, The Netherlands*
[32]*Joint Institute for Nuclear Research, Dubna, Russia*
[33]*Institute for Theoretical and Experimental Physics, Moscow, Russia*
[34]*Moscow State University, Moscow, Russia*
[35]*Institute for High Energy Physics, Protvino, Russia*
[36]*Petersburg Nuclear Physics Institute, St. Petersburg, Russia*
[37]*Institució Catalana de Recerca i Estudis Avançats (ICREA) and Institut de Física d'Altes Energies (IFAE), Barcelona, Spain*
[38]*Uppsala University, Uppsala, Sweden*
[39]*Lancaster University, Lancaster LA1 4YB, United Kingdom*
[40]*Imperial College London, London SW7 2AZ, United Kingdom*
[41]*The University of Manchester, Manchester M13 9PL, United Kingdom*
[42]*University of Arizona, Tucson, Arizona 85721, USA*
[43]*University of California Riverside, Riverside, California 92521, USA*
[44]*Florida State University, Tallahassee, Florida 32306, USA*
[45]*Fermi National Accelerator Laboratory, Batavia, Illinois 60510, USA*
[46]*University of Illinois at Chicago, Chicago, Illinois 60607, USA*
[47]*Northern Illinois University, DeKalb, Illinois 60115, USA*
[48]*Northwestern University, Evanston, Illinois 60208, USA*
[49]*Indiana University, Bloomington, Indiana 47405, USA*
[50]*Purdue University Calumet, Hammond, Indiana 46323, USA*
[51]*University of Notre Dame, Notre Dame, Indiana 46556, USA*
[52]*Iowa State University, Ames, Iowa 50011, USA*
[53]*University of Kansas, Lawrence, Kansas 66045, USA*
[54]*Kansas State University, Manhattan, Kansas 66506, USA*
[55]*Louisiana Tech University, Ruston, Louisiana 71272, USA*

B. PUBLISHED PAPER

[56]*Boston University, Boston, Massachusetts 02215, USA*
[57]*Northeastern University, Boston, Massachusetts 02115, USA*
[58]*University of Michigan, Ann Arbor, Michigan 48109, USA*
[59]*Michigan State University, East Lansing, Michigan 48824, USA*
[60]*University of Mississippi, University, Mississippi 38677, USA*
[61]*University of Nebraska, Lincoln, Nebraska 68588, USA*
[62]*Rutgers University, Piscataway, New Jersey 08855, USA*
[63]*Princeton University, Princeton, New Jersey 08544, USA*
[64]*State University of New York, Buffalo, New York 14260, USA*
[65]*Columbia University, New York, New York 10027, USA*
[66]*University of Rochester, Rochester, New York 14627, USA*
[67]*State University of New York, Stony Brook, New York 11794, USA*
[68]*Brookhaven National Laboratory, Upton, New York 11973, USA*
[69]*Langston University, Langston, Oklahoma 73050, USA*
[70]*University of Oklahoma, Norman, Oklahoma 73019, USA*
[71]*Oklahoma State University, Stillwater, Oklahoma 74078, USA*
[72]*Brown University, Providence, Rhode Island 02912, USA*
[73]*University of Texas, Arlington, Texas 76019, USA*
[74]*Southern Methodist University, Dallas, Texas 75275, USA*
[75]*Rice University, Houston, Texas 77005, USA*
[76]*University of Virginia, Charlottesville, Virginia 22901, USA*
[77]*University of Washington, Seattle, Washington 98195, USA*

(Received 13 April 2012; published 7 June 2012)

We measure the Λ_b^0 lifetime in the fully reconstructed decay $\Lambda_b^0 \to J/\psi\Lambda^0$ using 10.4 fb^{-1} of $p\bar{p}$ collisions collected with the D0 detector at $\sqrt{s} = 1.96$ TeV. The lifetime of the topologically similar decay channel $B^0 \to J/\psi K_S^0$ is also measured. We obtain $\tau(\Lambda_b^0) = 1.303 \pm 0.075(\text{stat}) \pm 0.035(\text{syst})$ ps and $\tau(B^0) = 1.508 \pm 0.025(\text{stat}) \pm 0.043(\text{syst})$ ps. Using these measurements, we determine the lifetime ratio of $\tau(\Lambda_b^0)/\tau(B^0) = 0.864 \pm 0.052(\text{stat}) \pm 0.033(\text{syst})$.

DOI: 10.1103/PhysRevD.85.112003 PACS numbers: 14.20.Mr, 13.25.Hw, 13.30.Eg, 14.40.Nd

Lifetime measurements of particles containing b quarks provide important tests of the significance of strong interactions between the constituent partons in the weak decay of b hadrons. These interactions produce measurable differences between b hadron lifetimes that the heavy quark expansion (HQE) [1] predicts with good accuracy through the calculation of lifetime ratios. While the agreement of the ratios between experimental measurements and HQE is excellent for B mesons [2], there are remaining discrepancies between experimental results and theoretical predictions for b baryons. Recently, the CDF Collaboration [3] used the exclusive decay $\Lambda_b^0 \to J/\psi\Lambda^0$ to report the single most precise determination of the Λ_b^0 lifetime which is more than 2 standard deviations higher than the world average [4] and slightly higher than the B^0 lifetime. The CDF measurement of the lifetime ratio, $\tau(\Lambda_b^0)/\tau(B^0)$, is higher than the HQE calculation including $\mathcal{O}(1/m_b^4)$ effects, 0.88 ± 0.05 [5,6]. On the other hand, theoretical predictions are in agreement with measurements by the D0 Collaboration in the $J/\psi\Lambda^0$ [7] and semileptonic [8] channels, by the CDF Collaboration in the $\Lambda_c^+\pi^-$ final state [9], by the DELPHI, OPAL, and ALEPH Collaborations in semileptonic decays [10–12], and previous measurements also in semileptonic channels by the CDF Collaboration [13]. More measurements of the Λ_b^0 lifetime and of the ratio $\tau(\Lambda_b^0)/\tau(B^0)$ are required to resolve this discrepancy.

In this article we report a measurement of the Λ_b^0 lifetime using the exclusive decay $\Lambda_b^0 \to J/\psi\Lambda^0$. The B^0 lifetime is also measured in the topologically similar channel $B^0 \to J/\psi K_S^0$. This provides a cross-check of the measurement procedure, and allows the lifetime ratio to be determined directly. The data used in this analysis were collected with the D0 detector during the complete Run II of the Tevatron Collider, from 2002 to 2011, and correspond to an integrated luminosity of 10.4 fb^{-1} of $p\bar{p}$ collisions at a center-of-mass energy $\sqrt{s} = 1.96$ TeV.

A detailed description of the D0 detector can be found in Refs. [14–17]. Here, we describe briefly the most relevant detector components used in this analysis. The D0 central

*Visitor from Augustana College, Sioux Falls, SD, USA.
†Visitor from The University of Liverpool, Liverpool, UK.
‡Visitor from UPIITA-IPN, Mexico City, Mexico.
§Visitor from DESY, Hamburg, Germany.
‖Visitor from SLAC, Menlo Park, CA, USA.
¶Visitor from University College London, London, UK.
**Visitor from Centro de Investigacion en Computacion - IPN, Mexico City, Mexico.
††Visitor from ECFM, Universidad Autonoma de Sinaloa, Culiacán, Mexico.
‡‡Visitor from Universidade Estadual Paulista, São Paulo, Brazil.
§§Deceased.

tracking system is composed of a silicon microstrip tracker (SMT) and a central scintillating fiber tracker (CFT) immersed in a 2 T solenoidal field. The SMT and the CFT are optimized for tracking and vertexing for the pseudorapidity region $|\eta| < 3.0$ and $|\eta| < 2.0$, respectively, where $\eta \equiv -\ln[\tan(\theta/2)]$ and θ is the polar angle with respect to the proton beam direction. Preshower detectors and electromagnetic and hadronic calorimeters surround the tracker. A muon spectrometer is located beyond the calorimeter, and consists of three layers of drift tubes and scintillation trigger counters covering $|\eta| < 2.0$. A 1.8 T toroidal iron magnet is located outside the innermost layer of the muon detector.

For all Monte Carlo (MC) simulations in this article, we use PYTHIA [18] to simulate the $p\bar{p}$ collisions, EVTGEN [19] for modeling the decay of particles containing b and c quarks, and GEANT [20] to model the detector response. Multiple $p\bar{p}$ interactions are modeled by overlaying hits from random bunch crossings onto the MC.

In order to reconstruct the Λ_b^0 and B^0 candidates, we start by searching for $J/\psi \to \mu^+\mu^-$ candidates, which are collected by single muon and dimuon triggers. The triggers used do not rely on the displacement of tracks from the interaction point. At least one $p\bar{p}$ interaction vertex (PV) must be identified in each event. The interaction vertices are found by minimizing a χ^2 function that depends on all reconstructed tracks in the event and uses the transverse beam position averaged over multiple beam crossings. The resolution of the PV is ≈ 20 μm in the plane perpendicular to the beam (transverse plane). Muon candidates are reconstructed from tracks formed by hits in the central tracking system and with transverse momentum (p_T) greater than 1 GeV/c. At least one muon candidate in the event must have hits in the inner layer, and in at least one outer layer of the muon detector. A second muon candidate, with opposite charge, must either be detected in the innermost layer of the muon system or have a calorimeter energy deposit consistent with that of a minimum-ionizing particle along the direction of hits extrapolated from the central tracking system. Each muon track is required to have at least two hits in the SMT and two hits in the CFT to ensure a high quality common vertex. The probability associated with the vertex fit must exceed 1%. The dimuon invariant mass is required to be in the range 2.80–3.35 GeV/c^2, consistent with the J/ψ mass.

Events with J/ψ candidates are reprocessed with a version of the track reconstruction algorithm that identifies with increased efficiency the low p_T and high impact parameter tracks resulting from the decay of Λ^0 and K_S^0 [21], without introducing any biases in the decay time distribution. We then search for $\Lambda^0 \to p\pi^-$ candidates reconstructed from pairs of oppositely charged tracks. The tracks must form a vertex with a probability associated with the vertex fit greater than 1%. The transverse impact parameter significance (the transverse impact parameter with respect to the PV divided by its uncertainty) for the two tracks forming Λ^0 candidates must exceed 2, and 4 for at least one of them. Each Λ^0 candidate is required to have a mass in the range 1.105–1.127 GeV/c^2. The track with the higher p_T is assigned the proton mass. MC simulations indicate that this is always the correct assumption, given the track p_T detection threshold of 120 MeV/c. To suppress contamination from decays of more massive baryons such as $\Sigma^0 \to \Lambda^0\gamma$ and $\Xi^0 \to \Lambda^0\pi^0$, the Λ^0 momentum vector must point within 1° back to the J/ψ vertex. The same selection criteria are applied in the selection of $K_S^0 \to \pi^+\pi^-$ candidates, except that the mass window is chosen in the range 0.470–0.525 GeV/c^2 and pion mass assignments are used. Track pairs simultaneously reconstructed as both Λ^0 and K_S^0, due to different mass assignments to the same tracks, are discarded from both samples. This requirement rejects 23% (6%) of the $\Lambda_b^0 \to J/\psi\Lambda^0$ ($B^0 \to J/\psi K_S^0$) signal, as estimated from MC, without introducing biases in the lifetime measurement. The fraction of background rejected by this requirement is 58% (48%) as estimated from data. It is important to remove these backgrounds from the samples to avoid the introduction of biases in the lifetime measurements.

The Λ_b^0 candidates are reconstructed by performing a kinematic fit that constrains the dimuon invariant mass to the world average J/ψ mass [4], and the Λ^0 and two muon tracks to a common vertex, where the Λ^0 has been extrapolated from its decay vertex according to the reconstructed Λ^0 momentum vector. The invariant mass of the Λ_b^0 candidate is required to be within the range 5.15–6.05 GeV/c^2. The PV is recalculated excluding the Λ_b^0 final decay products. The final selection requirements are obtained by maximizing $\mathcal{S} = S/\sqrt{S+B}$, where S (B) is the number of signal (background) candidates in the data sample: the decay length of the Λ^0 (measured from the Λ_b^0 vertex) and its significance are required to be greater than 0.3 cm and 3.5, respectively; the p_T of the J/ψ, Λ^0, and Λ^0 daughter tracks are required to be greater than 4.5, 1.8, and 0.3 GeV/c, respectively; and the isolation of the Λ_b^0 [22] is required to be greater than 0.35. After this optimization, if more than one candidate is found in the event, which happens in less than 0.3% of the selected events, the candidate with the best Λ_b^0 decay vertex fit probability is chosen. We have verified that this selection is unbiased by varying the selection values chosen by the optimization as described in more detail later. The same selection criteria are applied to $B^0 \to J/\psi K_S^0$ decays, except that the B^0 mass window is chosen in the range 4.9–5.7 GeV/c^2.

The samples of Λ_b^0 and B^0 candidates have two primary background contributions: combinatorial background and partially reconstructed b hadron decays. The combinatorial background can be divided in two categories: prompt background, which accounts for $\approx 70\%$ of the total background, primarily due to direct production of J/ψ mesons; and nonprompt background, mainly produced by random combinations of a J/ψ meson from a b hadron and a Λ^0

(K_S^0) candidate in the event. Contamination from partially reconstructed b hadrons comes from b baryons (B mesons) decaying to a J/ψ meson, a Λ^0 baryon (K_S^0 meson), and additional decay products that are not reconstructed.

We define the transverse proper decay length as $\lambda = cML_{xy}/p_T$, where M is the mass of the b hadron taken from the PDG [4], and L_{xy} is the vector pointing from the PV to the b hadron decay vertex projected on the b hadron transverse momentum ($\vec{p}_T$) direction. Because of the fact that signal and partially reconstructed b hadron decays have similar λ distributions that are particularly hard to disentangle in the lifetime fit, we remove partially reconstructed b hadrons by rejecting events with Λ_b^0 (B^0) invariant mass below 5.42(5.20) GeV/c^2 from the Λ_b^0 (B^0) sample, as shown in Fig. 1. This figure shows the Λ_b^0 and B^0 invariant mass distributions with results of unbinned maximum likelihood fits superimposed, excluding events in zones contaminated by partially reconstructed b hadrons. The signal peak is modeled by a Gaussian function. The combinatorial background is parametrized by an exponentially decaying function, while partially reconstructed b hadrons are derived from MC. It can be seen from Fig. 1 that partially reconstructed b hadrons contribute minimally to the signal mass region.

In order to extract the lifetimes, we perform separate unbinned maximum likelihood fits for Λ_b^0 and B^0 candidates. The likelihood function ($\mathcal{L}$) depends on the probability of reconstructing each candidate event j in the sample with the mass m_j, the proper decay length λ_j, and proper decay length uncertainty σ_j^λ:

$$\mathcal{L} = \prod_j [f_s \mathcal{F}_s(m_j, \lambda_j, \sigma_j^\lambda) + (1 - f_s)\mathcal{F}_b(m_j, \lambda_j, \sigma_j^\lambda)], \quad (1)$$

where f_s is the fraction of signal events, and $\mathcal{F}_s$ ($\mathcal{F}_b$) is the product of the probability distribution functions that model each of the three observables being considered for signal (background) events. The background is further divided into prompt and nonprompt components. For the signal, the mass distribution is modeled by a Gaussian function; the λ distribution is parametrized by an exponential decay, $e^{-\lambda_j/c\tau}/c\tau$, convoluted with a Gaussian function $\mathcal{R} = e^{-\lambda_j^2/2(s\sigma_j^\lambda)^2}/\sqrt{2\pi}s\sigma_j^\lambda$ that models the detector resolution; the σ^λ distribution is obtained from MC simulation and parametrized by a superposition of Gaussian functions. Here τ is the lifetime of the b hadron, and the event-by-event uncertainty σ_j^λ is scaled by a global factor s to take into account a possible underestimation of the uncertainty. The mass distribution of the prompt component of the background is parameterized by a constant function, since we observe that the total amount of background is reduced uniformly over the entire mass range when the requirement $\lambda > 100$ μm is applied. The nonprompt component of the background is modeled by an exponential function, as observed using the data satisfying this requirement. The prompt component of the λ distribution is parametrized by the resolution function, and the nonprompt component by the superposition of two exponential decays for $\lambda < 0$ and two exponential decays for $\lambda > 0$, as observed from events in the high-mass sideband of the b hadron peak (above 5.80 and 5.45 GeV/c^2 for Λ_b^0 and B^0, respectively). Finally, the background σ^λ distribution is modeled by two exponential functions convoluted with a Gaussian function as determined empirically from the high-mass sideband region. All the events, except for those corresponding to the invariant mass region contaminated by partially reconstructed b hadrons, are used in each likelihood fit to determine a total of 19 parameters: lifetime, mean, and width of the signal mass, signal fraction, prompt background fraction, one nonprompt background mass parameter, seven nonprompt background λ parameters, five background σ^λ parameters, and one resolution scale factor.

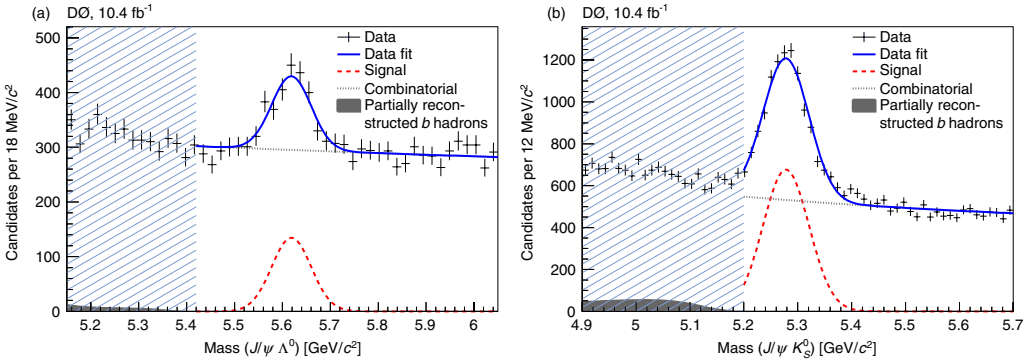

FIG. 1 (color online). Invariant mass distributions for (a) $\Lambda_b^0 \to J/\psi\Lambda^0$ and (b) $B^0 \to J/\psi K_S^0$ candidates, with fit results superimposed. Events in mass regions contaminated with partially reconstructed b hadrons (hatched region) are excluded from the maximum likelihood function used to determine the Λ_b^0 and B^0 lifetimes.

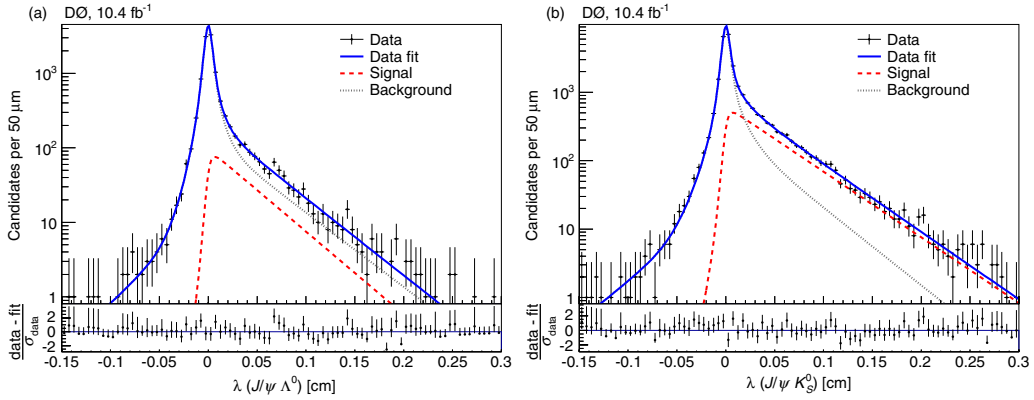

FIG. 2 (color online). Proper decay length distributions for (a) $\Lambda_b^0 \to J/\psi\Lambda^0$ and (b) $B^0 \to J/\psi K_S^0$ candidates, with fit results superimposed. Residuals normalized by the corresponding uncertainty in each bin are given in the bottom panel.

The maximum likelihood fits to the data yield $c\tau(\Lambda_b^0) = 390.7 \pm 22.4\,\mu$m and $c\tau(B^0) = 452.2 \pm 7.6\,\mu$m. Figure 2 shows the λ distributions for the Λ_b^0 and the B^0 candidates. Fit results are superimposed. The numbers of signal events, derived from f_s, are 755 ± 49 (Λ_b^0) and 5671 ± 126 (B^0). The ratios of the event yields in this and in the previous measurement [7] do not scale with the integrated luminosity because the most recent D0 data was collected at higher instantaneous luminosities, which required tighter, and less efficient, trigger requirements and also resulted in a reduction of the reconstruction efficiency caused by the presence of multiple interactions in a single bunch crossing.

We investigate possible sources of systematic uncertainties on the measured lifetimes related to the models used to describe the mass, λ, and σ^λ distributions. For the mass we consider a double Gaussian to model the signal peak instead of the nominal single Gaussian, an exponential function for the prompt background in place of a constant function, and a second-order polynomial for the nonprompt background. The alternative mass models are combined in a single maximum likelihood fit to take into account correlations between the effects of the different models, and the difference with respect to the result of the nominal fit is quoted as the systematic uncertainty on the mass model. For λ we study the following variations: the introduction of a second Gaussian function along with a second scale factor to model the resolution, the exponential functions in the nonprompt background replaced by exponentials convoluted with the resolution function, one nonprompt negative exponential instead of two, and one long positive exponential together with a double-Gaussian resolution as a substitute for two nonprompt exponentials and one Gaussian resolution. All λ model changes are combined in a fit, and the difference between the results of this fit and the nominal fit is quoted as the systematic uncertainty due to λ parametrization. For σ^λ we use two different approaches: we use the distribution extracted from data by background subtraction, parameterized similarly to the nominal background σ^λ model, instead of the MC model, and we use σ^λ distributions from MC samples generated with different Λ_b^0 (B^0) lifetimes. The largest variation in the lifetime (with respect to the nominal measurement) between these two alternative approaches is quoted as the systematic uncertainty due to σ^λ parametrization. Residual effects due to contamination from partially reconstructed b hadrons in the samples are investigated by changing the requirement on the invariant mass of the Λ_b^0 and B^0 candidates that are included in the likelihood fits: the threshold is moved to lower (higher) invariant masses by 40(20) MeV$/c^2$, where 40 MeV$/c^2$ is the resolution on the invariant mass of the reconstructed signal. The largest variation in the lifetime is quoted as the systematic uncertainty due to possible contamination from partially reconstructed b hadrons. In the lifetime fit the contamination from the fully reconstructed decay $B_s^0 \to J/\psi K_S^0$ is assumed to have little impact on the final result. To test this assumption the $B_s^0 \to J/\psi K_S^0$ contribution is included in the nonprompt component. The lifetime shift is found to be negligible. The systematic uncertainty due to the alignment of the SMT detector was estimated in a previous study [7] by reconstructing the B^0 sample with the positions of the SMT sensors shifted outwards radially by the alignment uncertainty and then fitting for the lifetime. The systematic uncertainties are summarized in Table I.

We perform several cross-checks of the lifetime measurements. We extract the signal yield in bins of λ by fitting the mass distribution in each of these regions. From these measurements, lifetimes are obtained by the χ^2 minimization of the signal yield expected in each λ bin according to

B. PUBLISHED PAPER

TABLE I. Summary of systematic uncertainties on the measurements of $c\tau(\Lambda_b^0)$ and $c\tau(B^0)$, and on their ratio. Individual uncertainties are combined in quadrature to obtain the total uncertainties.

Source	Λ_b^0 (μm)	B^0 (μm)	Ratio
Mass model	2.2	6.4	0.008
Proper decay length model	7.8	3.7	0.024
Proper decay length uncertainty	2.5	8.9	0.020
Partially reconstructed b hadrons	2.7	1.3	0.008
$B_s^0 \to J/\psi K_S^0$	—	0.4	0.001
Alignment	5.4	5.4	0.002
Total	10.4	12.9	0.033

the first term in Eq. (1). While this method is statistically inferior with respect to the maximum likelihood fit, it is also less dependent on the modeling of the different background components. The results of this study are $c\tau_{\Lambda_b^0} = 391.4 \pm 35.8(\text{stat})$ μm and $c\tau_{B^0} = 458.3 \pm 8.9(\text{stat})$ μm. The sample is also split into different data taking periods, η regions, and numbers of hits in the SMT detector. All results obtained with these variations are consistent with our measurement. In order to check that the optimization procedure does not give a potential bias to the selection, we verify that our results remain stable when all requirements in variables used in the optimization process are removed one at a time, when looser and tighter requirements are applied to kinematic variables, and when multiple candidates that pass all selection requirements per event are allowed. The results also remain stable after removing the high-end tail (above 100 μm) of the σ^λ distribution, mainly populated by background events. We also cross-check the fitting procedure and selection criteria by measuring the Λ_b^0 and B^0 lifetimes in MC events. The lifetimes obtained are consistent with the input values.

In summary, using the full data sample collected by the D0 experiment, we measure the lifetime of the Λ_b^0 baryon in the $J/\psi\Lambda^0$ final state to be

$$\tau(\Lambda_b^0) = 1.303 \pm 0.075(\text{stat}) \pm 0.035(\text{syst}) \text{ ps}, \quad (2)$$

consistent with the world average, 1.425 ± 0.032 ps [4]. The method to measure the Λ_b^0 lifetime is also used for $B^0 \to J/\psi K_S^0$ decays, for which we obtain

$$\tau(B^0) = 1.508 \pm 0.025(\text{stat}) \pm 0.043(\text{syst}) \text{ ps}, \quad (3)$$

in good agreement with the world average, 1.519 ± 0.007 ps [4].

Using these measurements we calculate the ratio of lifetimes,

$$\frac{\tau(\Lambda_b^0)}{\tau(B^0)} = 0.864 \pm 0.052(\text{stat}) \pm 0.033(\text{syst}), \quad (4)$$

where the systematic uncertainty is determined from the differences between the lifetime ratio obtained for each systematic variation and the ratio of the nominal measurements, and combining theses differences in quadrature, as shown in Table I. Our result, 0.86 ± 0.06, is in good agreement with the HQE prediction of 0.88 ± 0.05 [5] and compatible with the current world average, 1.00 ± 0.06 [4], but differs with the latest measurement of the CDF Collaboration, 1.02 ± 0.03 [3], at the 2.2 standard deviations level. Our measurements supersede the previous D0 results of $\tau(\Lambda_b^0)$, $\tau(B^0)$, and $\tau(\Lambda_b^0)/\tau(B^0)$ [7].

We thank the staffs at Fermilab and collaborating institutions, and acknowledge support from the DOE and NSF (USA); CEA and CNRS/IN2P3 (France); MON, Rosatom and RFBR (Russia); CNPq, FAPERJ, FAPESP and FUNDUNESP (Brazil); DAE and DST (India); Colciencias (Colombia); CONACyT (Mexico); NRF (Korea); FOM (The Netherlands); STFC and the Royal Society (United Kingdom); MSMT and GACR (Czech Republic); BMBF and DFG (Germany); SFI (Ireland); The Swedish Research Council (Sweden); and CAS and CNSF (China).

[1] G. Bellini, I. I. Y. Bigi, and P. J. Dornan, Phys. Rep. **289**, 1 (1997).
[2] A. J. Lenz, AIP Conf. Proc. **1026**, 36 (2008).
[3] T. Aaltonen *et al.* (CDF Collaboration), Phys. Rev. Lett. **106**, 121804 (2011).
[4] K. Nakamura *et al.* (Particle Data Group), J. Phys. G **37**, 075021 (2010).
[5] C. Tarantino, Nucl. Phys. B, Proc. Suppl. **156**, 33 (2006).
[6] F. Gabbiani, A. I. Onishchenko, and A. A. Petrov, Phys. Rev. D **68**, 114006 (2003); **70**, 094031 (2004).
[7] V. M. Abazov *et al.* (D0 Collaboration), Phys. Rev. Lett. **99**, 142001 (2007).
[8] V. M. Abazov *et al.* (D0 Collaboration), Phys. Rev. Lett. **99**, 182001 (2007).
[9] T. Aaltonen *et al.* (CDF Collaboration), Phys. Rev. Lett. **104**, 102002 (2010).
[10] P. Abreu *et al.* (DELPHI Collaboration), Eur. Phys. J. C **10**, 185 (1999).
[11] K. Ackerstaff *et al.* (OPAL Collaboration), Phys. Lett. B **426**, 161 (1998).
[12] R. Barate *et al.* (ALEPH Collaboration), Eur. Phys. J. C **2**, 197 (1998).
[13] F. Abe *et al.* (CDF Collaboration), Phys. Rev. Lett. **77**, 1439 (1996).

[14] V. M. Abazov *et al.* (D0 Collaboration), Nucl. Instrum. Methods Phys. Res., Sect. A **565**, 463 (2006).
[15] M. Abolins *et al.*, Nucl. Instrum. Methods Phys. Res., Sect. A **584**, 75 (2008).
[16] R. Angstadt *et al.*, Nucl. Instrum. Methods Phys. Res., Sect. A **622**, 298 (2010).
[17] S. Ahmed *et al.*, Nucl. Instrum. Methods Phys. Res., Sect. A **634**, 8 (2011).
[18] T. Sjöstrand *et al.*, Comput. Phys. Commun. **135**, 238 (2001).
[19] D. J. Lange, Nucl. Instrum. Methods Phys. Res., Sect. A **462**, 152 (2001).
[20] R. Brun and F. Carminati, CERN Program Library Long Writeup Report No. W5013, 1993.
[21] V. M. Abazov *et al.* (D0 Collaboration), Phys. Rev. Lett. **99**, 052001 (2007).
[22] Isolation is defined as $p(B)/[p(B) + \sum_{<\Delta R} p]$, where $p(B)$ is the momentum of the b hadron and the sum, excluding the decay products of the b hadron, is over the momentum of all particles from the PV within the larger $\Delta R(\mu^{\pm}, b$ hadron) cone in pseudorapidity-azimuthal angle space, defined as $\Delta R = \sqrt{\Delta\eta^2 + \Delta\phi^2}$.

Bibliography

[1] K. Nakamura *et al.* (Particle Data Group), J. Phys. G **37**, 075021 (2010).

[2] I. Heredia-De La Cruz, arXiv:1109.6083v3 [hep-ex] (2011).

[3] V.M. Abazov *et al.* (D0 Collaboration), Phys. Rev. D. **84**, 031102(R) (2011).

[4] T. Aaltonen *et al.* (CDF Collaboration), Phys. Rev. Lett. **107**, 201802 (2011).

[5] G. Bellini, I. I. Y. Bigi, and P. J. Dornan, Phys. Rep. **289**, 1 (1997).

[6] A. J. Lenz, AIP Conf. Proc. **1026**, 36 (2008).

[7] T. Aaltonen *et al.* (CDF Collaboration), Phys. Rev. Lett. **106**, 121804 (2011); A. Abulencia *et al.* (CDF Collaboration), Phys. Rev. Lett. **98**, 122001 (2007).

[8] C. Tarantino, Nucl. Phys. B, Proc. Suppl. **156**, 33 (2006).

[9] F. Gabbiani, A. I. Onishchenko, and A. A. Petrov, Phys. Rev. D **68**, 114006 (2003); **70**, 094031 (2004).

[10] V. M. Abazov *et al.* (D0 Collaboration), Phys. Rev. Lett. **99**, 142001 (2007); **94**, 102001 (2005).

[11] V. M. Abazov *et al.* (D0 Collaboration), Phys. Rev. Lett. **99** 182001 (2007).

[12] T. Aaltonen *et al.* (CDF Collaboration), Phys. Rev. Lett. **104**, 102002 (2010).

[13] P. Abreu *et al.* (DELPHI Collaboration) Eur. Phys. J. C **10**, 185 (1999).

[14] K. Ackerstaff *et al.* (OPAL Collaboration), Phys. Lett. B **426**, 161 (1998).

[15] R. Barate *et al.* (ALEPH Collaboration), Eur. Phys. J. C **2**, 197 (1998).

[16] F. Abe *et al.* (CDF Collaboration), Phys. Rev. Lett. **77**, 1439 (1996).

[17] `http://en.wikipedia.org/wiki/Standard_Model`; Wikimedia Commons. License: CC 3.0 Unported, `http://creativecommons.org/licenses/by/3.0/deed.en`

[18] `http://en.wikipedia.org/wiki/Cabibbo-Kobayashi-Maskawa_matrix`

[19] M. Abazov *et al.* (D0 Collaboration), Phys. Rev. D **85**, 032006 (2012).

[20] K. Anikeev *et al.*, Report No. FERMILAB-Pub-01/197, arXiv:hep-ph/0201071 (2001).

[21] A. J. Buras and M. Linder (1998), *Heavy Flavors II*, World Scientific, New Jersey.

[22] A. J. Buras, M. Misiak and J. Urban, Nucl. Phys. B **586** 397 (2000).

[23] M. Neubert, arXiv:hep-ph/0512222v1 (2005).

[24] A. Lenz, arXiv:1205.1444v1 [hep-ph] (2012).

[25] `http://www.fnal.gov/pub/science/accelerator/`

[26] `http://www.fnal.gov/pub/news04/update_archive/update_10-1.html`

[27] `http://www.fnal.gov/pub/tevatron/milestones/interactive-timeline.html`

[28] `http://d0server1.fnal.gov/Projects/Operations/D0RunII_DataTaking.htm`

[29] `http://www.fnal.gov/pub/presspass/press_releases/2011/Tevatron-Shutdown-20100726-images.html`

[30] V. M. Abazov *et al.* (D0 Collaboration), Nucl. Instrum. Methods Phys. Res. A **565**, 463 (2006).

[31] M. Abolins *et al.*, Nucl. Instrum. Methods Phys. Res. A **584**, 75 (2008).

[32] R. Angstadt *et al.*, Nucl. Instrum. Methods Phys. Res. A **622**, 298 (2010).

[33] S. Ahmed *et al.*, Nucl. Instrum. Methods Phys. Res. A **634**, 8 (2011).

[34] J. M. Campbell, J. W. Huston and W. J. Stirling, Rep. Prog. Phys. **70**, 89 (2007).

[35] `http://d0server1.fnal.gov/users/nomerot/Run2A/B_ANA.html`

[36] Abdallah, J. *et al.* Eur. Phys. J. C **32**, 185 (2004).

[37] V.M. Abazov *et al.* (D0 Collaboration), Phys. Rev. Lett. **99**, 052001 (2007).

[38] `http://www-d0.fnal.gov/Run2Physics/cs/extaa/extaa2.html`

[39] Griffiths, D. (1987), *Introduction to Elementary Particles*, John Wiley & Sons, Inc., New York.

[40] Balm, P. (2004), *Measurement of the B^0 lifetime using $B^0 \to J/\psi\, K^0_S$ decays at DØ*, PhD thesis, University of Amsterdam.

[41] M. Abazov *et al.* (D0 Collaboration), Phys. Rev. Lett. **102**, 032001 (2009).

[42] T. Aaltonen *et al.* (CDF Collaboration), Phys. Rev. D **83**, 052012 (2011).

[43] D.J. Lange, Nucl. Instrum. Meth. Phys. Res. A **462**, 152 (2001).

[44] G. Punzi, arXiv:physics/0401045v1 [physics.data-an] (2004).

[45] K. S. Cranmer, Comput. Phys. Commun. **136**, 198 (2001); arXiv:hep-ex/0011057v1 (2000); `http://root.cern.ch/root/html/RooKeysPdf.html`

[46] M. Abazov *et al.* (D0 Collaboration), Phys. Rev. D 85, **112003** (2012); arXiv:1204.2340v2 [hep-ex] (2012).

[47] T. Sjöstrand *et al.*, Comp. Phys. Commun. **135**, 238 (2001).

[48] R. Brun and F. Carminati, CERN Program Library Long Writeup Report No. W5013, 1993 (unpublished).

[49] `http://www.phys.psu.edu/~cteq/`

[50] E. Richter-Was, Phys. Lett. B **303**, 163 (1993).

[51] S. Chatrchyan, *et al.* (CMS Collaboration), arXiv:1205.0594v1 [hep-ex] (2012).

[52] J. Hrivnac *et al.*, J. Phys. G **21**, 629 (1995).

[53] I. Dunietz, Z. Phys. C **56**, 129 (1992).

[54] E. Di Salvo, Z. J. Ajaltouni, Mod. Phys. Lett. A **24**, 109-121 (2009).